

AN APPROXIMATE SOLUTION OF THE EQUATIONS OF MOTION
FOR ARBITRARY ROTATING SPACECRAFT

By

Peter Ralph Kurzhals

Thesis submitted to the Graduate Faculty of the
Virginia Polytechnic Institute

in candidacy for the degree of

DOCTOR OF PHILOSOPHY

in

Aerospace Engineering

GPO PRICE \$ _____

CFSTI PRICE(S) \$ _____

Hard copy (HC) 6.00

Microfiche (MF) 1.50

653 July 65

May 1966

N66 29735
(ACCESSION NUMBER)
244
(PAGES)
TM-257691
(NASA CR OR TMX OR AD NUMBER)

(THRU)
1
(CODE)
30
(CATEGORY)

FACILITY FORM 602

AN APPROXIMATE SOLUTION OF THE EQUATIONS OF MOTION
FOR ARBITRARY ROTATING SPACECRAFT

By Peter Ralph Kurzahls

ABSTRACT

The determination of the motion of rotating spacecraft, such as manned space stations and spinning satellites, requires the solution of the spacecraft's equations of motion with varying disturbance torques and mass distributions. The numerical integration of these equations on high-speed computing equipment can give only limited information on the effects of disturbance and spacecraft characteristics, and cannot provide the physical insight needed for an analysis of the spacecraft motion. An approximate solution of the governing equations which would yield a direct assessment of the effects of applied disturbances and would lead to a clear understanding of the motion mechanics could thus be particularly useful.

This dissertation comprises the development and application of an approximate analytical solution for the motion of arbitrary rotating spacecraft with variable disturbance functions. The solution is based on the assumptions of small changes in the spacecraft inertia characteristics, body rates, and Euler angles. The rate and attitude errors, resulting from the application of disturbance torques, are described by complex pseudovectors and the governing spacecraft equations are reduced to linear differential equations in terms of these error vectors. Solutions are obtained for the steady spinning mode and for a spinup and despin mode.

AN APPROXIMATE SOLUTION OF THE EQUATIONS OF MOTION
FOR ARBITRARY ROTATING SPACECRAFT

By Peter Ralph Kurzhals

ABSTRACT

29735

The determination of the motion of rotating spacecraft, such as manned space stations and spinning satellites, requires the solution of the spacecraft's equations of motion with varying disturbance torques and mass distributions. The numerical integration of these equations on high-speed computing equipment can give only limited information on the effects of disturbance and spacecraft characteristics, and cannot provide the physical insight needed for an analysis of the spacecraft motion. An approximate solution of the governing equations which would yield a direct assessment of the effects of applied disturbances and would lead to a clear understanding of the motion mechanics could thus be particularly useful.

This dissertation comprises the development and application of an approximate analytical solution for the motion of arbitrary rotating spacecraft with variable disturbance functions. The solution is based on the assumptions of small changes in the spacecraft inertia characteristics, body rates, and Euler angles. The rate and attitude errors, resulting from the application of disturbance torques, are described by complex pseudovectors and the governing spacecraft equations are reduced to linear differential equations in terms of these error vectors. Solutions are obtained for the steady spinning mode and for a spinup and despin mode.

Author

The solutions for the spinning mode consider the effects of initial errors, external torques, and instantaneous and periodic mass motions within the spacecraft. The resultant errors are presented as error component time histories and as traces of the complex error vectors. Upper bounds of the error magnitudes are deduced from the error vectors. Both the general case of nonsymmetric spacecraft and the special case of spacecraft rotating about an axis of symmetry are examined.

Periodic mass motions within the spacecraft are shown to have significant effects on the spacecraft motions and can produce errors several times greater than the errors predicted for "worst-case" instantaneous mass motions. Instability trends of the errors are also found when the spin axis becomes an intermediate axis of inertia during a mass motion and when the motions occur at the precession frequency λ .

The effectiveness of several control techniques is investigated for the approximate governing equations. Pure rate control and rate plus rate integral control are found to be acceptable for damping of the rate and attitude errors produced by mass motions and other internal disturbances. Rate plus attitude control is, however, needed for the elimination of possible residual attitude errors due to external disturbances and for the reorientation of the spacecraft. The implementation of the control techniques is discussed for reaction wheel, control moment gyro, and reaction jet systems. Actuator commands and the required control system weights are developed.

A comparison of the analytical solution and the exact solution obtained from numerical integration of the complete equations of motion

is used to establish the adequacy of the approximate solution. The applications of the analytical solution are illustrated for a manned orbital research laboratory and a large spinning space station.

The solutions for the spinup and despin mode are employed in the optimization of spinup and extension techniques for cable- or strut-connected spacecraft modules. Fuel savings of about 22 lb per spinup and despin cycle of the manned orbital research laboratory can be obtained by a continuous-thrust extension.

The analytical solution shows that a simple and valid interpretation of the spacecraft motions is possible for a large number of applied disturbances.

AN APPROXIMATE SOLUTION OF THE EQUATIONS OF MOTION
FOR ARBITRARY ROTATING SPACECRAFT

by

Peter Ralph Kurzhals

Thesis submitted to the Graduate Faculty of the
Virginia Polytechnic Institute

in candidacy for the degree of

DOCTOR OF PHILOSOPHY

in

Aerospace Engineering

APPROVED:

Chairman, Dr. James B. Eades

Dr. Daniel Frederick

Dr. Svend T. Gormsen

Dr. A. Keith Furr

Dr. Yasutada Kashiwagi

May 1966

Blacksburg, Virginia

II. TABLE OF CONTENTS

CHAPTER	PAGE
I. TITLE	1
II. TABLE OF CONTENTS	2
III. LIST OF FIGURES AND TABLES	6
IV. SYMBOLS	10
V. SUMMARY	16
VI. INTRODUCTION	17
VII. PROBLEM FORMULATION	20
A. Spacecraft Motion	20
B. Assumptions	22
C. Governing Equations	22
D. Total Errors	26
E. Solution Approach	30
VIII. ANALYSIS OF SPINNING MODE	32
A. Equations of Motion	33
B. Total Errors	41
C. Characteristic Disturbances for Nonsymmetric Spacecraft	43
1. Impulsive Torques	43
a. Time Histories	43
b. Total Errors	44
c. Initial Error Contribution	47
d. Impulsive Torque Contribution	53

	PAGE
2. Step Torques	53
a. Time Histories	53
b. Total Errors	54
3. Step Products of Inertia	61
a. Time Histories	61
b. Total Errors	63
4. Variable Products of Inertia	70
a. Stability Trends	72
b. Time Histories	74
c. Total Errors	75
D. Characteristic Disturbances for Symmetric	
Spacecraft	84
1. Impulsive Torques	86
2. Step Torques	90
3. Step Products of Inertia	93
4. Variable Products of Inertia	96
a. Circumferential Mass Motion	96
b. Radial Mass Oscillation	103
c. Vertical Mass Oscillation	108
E. Controlled Spacecraft Characteristics	114
1. Governing Equations	114
2. Control Requirements	117
3. Control Law Formulation	118

	PAGE
a. Pure Rate Control Law	119
b. Rate Plus Rate Integral Control Law	127
c. Rate Plus Attitude Control Law	131
d. General Considerations	135
4. Control System Selection	137
a. Reaction Wheels	138
b. Control Moment Gyroscopes	143
c. Reaction Jets	148
F. Comparison of Exact and Approximate Solution	150
1. Manned Orbital Research Laboratory - MORL	151
2. Large Manned Space Station	160
IX. ANALYSIS OF SPINUP AND DESPIN MODE	170
A. Governing Equations	170
B. Rigid Spacecraft	170
C. Extensible Spacecraft	171
1. Mathematical Model	171
2. Spinup and Despin Techniques	174
a. Constant-Momentum Extension	175
b. Constant-Rate Extension	175
c. Continuous-Thrust Extension	176
d. Comparison of Extension Techniques	177
X. CONCLUSIONS	184
XI. ACKNOWLEDGMENTS	187
XII. BIBLIOGRAPHY	188

	PAGE
XIII. VITA	192
XIV. APPENDIX A - DEVELOPMENT OF THE LINEARIZED EQUATIONS OF MOTION	193
XV. APPENDIX B - PARTICULAR SOLUTION FUNCTIONS FOR THE UNCONTROLLED SPACECRAFT	214

III. LIST OF FIGURES AND TABLES

FIGURES	PAGE
1. Reference system for rotating spacecraft	20
2. Vector transformation between spacecraft axes and intermediate reference system	21
3. Vectorial representation of total angular rate error . . .	27
4. Pseudovectorial representation of total attitude error . .	28
5. Rate error trace for initial conditions	47
6. Attitude error trace for initial conditions	49
7. Rate error trace for step torques	56
8. Attitude error trace for step torques	58
9. Rate error trace for step inertia product	64
10. Attitude error trace for step inertia products	67
11. Rate error traces for periodic inertia products	77
12. Rate error trace development for periodic inertia products	78
13. Attitude error traces for periodic inertia products . . .	80
14. Attitude error trace development for periodic inertia products	81
15. Rate error trace for initial conditions and symmetric spacecraft	87
16. Attitude error trace for initial conditions and symmetric spacecraft	88
17. Rate error trace for step torques and symmetric spacecraft	91

FIGURE	PAGE
18. Attitude error trace for step torques and symmetric spacecraft	92
19. Rate error trace for step inertia products and symmetric spacecraft	94
20. Attitude error trace for step inertia products and symmetric spacecraft	95
21. Rate error trace for circumferential mass motion and symmetric spacecraft	98
22. Attitude error trace for circumferential mass motion and symmetric spacecraft	100
23. Rate error trace for radial mass oscillation and symmetric spacecraft	104
24. Attitude error trace for radial mass oscillation and symmetric spacecraft	106
25. Rate error trace for vertical mass oscillation and symmetric spacecraft	110
26. Attitude error trace for vertical mass oscillation and symmetric spacecraft	111
27. Stability characteristics for the controlled spacecraft	123
28. Spacecraft control with reaction wheels	139
29. Variation of total reaction wheel weight with required angular momentum	141

FIGURE	PAGE
30. Spacecraft control with control moment gyros	143
31. Variation of total gyro weight with required angular momentum	145
32. Variation of total reaction jet system weight with required total impulse	149
33. Artist's sketch of possible Manned Orbital Research Laboratory	151
34. Uncontrolled laboratory error histories for step inertia products	155
35. Laboratory error histories for step inertia products and pure rate control	156
36. Uncontrolled laboratory error histories for vertical mass oscillation	158
37. Laboratory error histories for vertical mass oscillation and rate plus rate integral control	159
38. Artist's sketch of possible 150-foot manned space station	161
39. Uncontrolled station error histories for circumferential mass motion	164
40. Station error histories for circumferential mass motion and rate plus rate integral control	166
41. Uncontrolled station error histories for residual errors	167

FIGURE	PAGE
42. Station error histories for residual errors and rate plus attitude control	168
43. Mathematical model for spinup fuel calculations	171
44. Fuel criteria for extension technique selection	179

TABLES	PAGE
1. Solution Terms for Unit Step and Unit Impulse Functions	216
2. Solution Terms for Powers of t	217
3. Solution Terms for the Trigonometric Functions $\sin pt$ and $\cos pt$	218
4. Forcing Function Coefficients for the Variable Inertia Products	219
5. Solution Function Coefficients for the Variable Inertia Products	220
6. Assumed Characteristics for Manned Orbital Research Laboratory	221
7. Disturbance Effects on Manned Orbital Research Laboratory	222
8. Assumed Characteristics for 150-Foot Space Station	223
9. Disturbance Effects on 150-Foot Space Station	224

IV. SYMBOLS

A_j	complex coefficients of forcing function, (B-1) and (30)
a	power conversion factor, (254)
a, b, c, d, e, f	characteristic coordinate for the error traces
B_j	complex coefficients of total rate error relation, (43)
C_j	complex coefficients of total angular error relation, (44)
D_1, D_2, D_3, D_4, D_5	spinup parameters, (295) and (297)
E_1, E_2, E_3, E_4	forcing function coefficients for variable inertia products, table 4 and (112)
E_5, E_6, E_7	solution function coefficients for variable inertia products, (113) and (115)
F	complex forcing function, (30)
\overline{F}	complex solution function for the body rate errors
$\overline{\overline{F}}$	complex solution function for the Euler angle errors
f_x, f_y	forcing functions for the controlled spacecraft, (213) and (214)
G	complex actuator torque
G_s	actuator stall torque
g	complex control torque, (209)
H	rigid-body angular momentum
I	moment or product of inertia
I_0	spacecraft moment of inertia without moving particles
I_{rz}	radial inertia product, $I_{xz} + iI_{yz}$

I_{SP}	specific impulse
I_T	total impulse, (284)
K_{jx}, K_{jy}	control gains for the X and Y axes, (209)
k_{jx}, k_{jy}	nondimensional control gains for the X and Y axes, (210)
L	nondimensional external moment, (A-30)
l	distance between mass centers of manned and counter-weight modules
l_z	effective spinup moment arm, (294)
M	external moment, $M_x + iM_y$
M_z	spinup moment
m_j	mass of moving particle
m_s	mass of spacecraft and moving particles
$O[\Delta]$	order of $[\Delta]$
P	external force
p	frequency for moving particle
Q	constant defining center of mass change, (A-25)
\vec{R}_j	position vector of moving particle measured with respect to the origin of the fixed coordinate system
\vec{R}_0	position vector of origin of spacecraft coordinate system measured relative to the origin of the fixed coordinate system
r_D	damping ratio
\vec{r}_j	position vector of moving particle measured with respect to the spacecraft coordinate system

\vec{r}_s	position vector of composite mass center measured with respect to the spacecraft coordinate system
s	Laplace transform variable
sgn	signum function, denoting the sign of the characteristic coordinate or variable
T	constant step or impulse torque, $T_x + iT_y$
T_z	cross coupling torque applied to spacecraft by control system
t	time
t_D	time constant
$U(t)$	unit step function, (B-4)
V	effective forcing function
W	weight
X, Y, Z	reference axes
x, y, z	scalar components of \vec{r} along the X, Y, Z axes
u, v, w	nondimensional scalar components of \vec{r} along the X, Y, Z axes (A-30)
α	complex angular position error, $\phi + i\theta$, figure 4
α_g	limiting gyro gimbal angle, (272)
α_I	complex inertial position error, (14)
β_j	argument of B_j
γ_j	argument of C_j
$\delta(t)$	impulse function, (B-5)

Δ	quantity denoting the magnitude order of ω_k , $\dot{\omega}_p$, θ_φ , θ^2 , L_p , ρ_p , and the nondimensional inertia terms for the moving particles
ϵ	nondimensional moment or product of inertia, (A-29)
θ, φ, ψ	modified Euler angles, figure 2
λ, λ_k	precession rate parameters, (24), positive when I_z is maximum inertia and negative when I_z is minimum inertia
μ	nondimensional mass, (A-29)
ρ	nondimensional force, (A-30)
σ	constant positive spin rate, (15)
τ	nondimensional time, (A-29)
Φ	angular coordinate used in total error traces
$\vec{\Omega}$	total angular rate vector of spacecraft axis system
$\Omega_x, \Omega_y, \Omega_z$	scalar components of $\vec{\Omega}$ along the X, Y, Z axes
Ω_{xy}	complex rate error, $\Omega_x + i\Omega_y$, figure 3
ω_N	damped natural frequency
ω_S	synchronous wheel speed
$\omega_x, \omega_y, \omega_z$	nondimensional scalar components of $\vec{\Omega}$ along the X, Y, Z axes
Subscripts:	
a, b, c, d, e	value for corresponding characteristic coordinate
c	counterweight module
CM	extension at constant momentum
CR	extension with constant spin rate

CT	extension with continuous thrust
d	disturbance
F	fixed coordinates
f	final value after spinup
G	gyro
g	gyro gimbal
I	intermediate coordinates
i	intermediate value before extension
j	value for jth term or mass where $j = 1, 2, 3, \dots$
k, l	component for X or Y axis with $k \neq l$
lim	upper bound
M	momentum
m	manned module
max	maximum value
n	summed value for moving particles
O	value referred to origin of spacecraft body axes
o	initial value
P	power
p, q	component for X, Y, or Z axis
pq	component for XY, XZ, or YZ plane
SU	spinup fuel
s	value for spacecraft mass center
R	reaction control
r	residual value

T	total
x,y,z	component for X, Y, or Z axis
xy,xz,yz	component for XY, XZ, or YZ plane
W	reaction wheel

A dot over a symbol denotes the derivative with respect to time.

An arrow (\rightarrow) over a symbol denotes a vector.

A tilde (\sim) over a symbol denotes the general solution function corresponding to initial rate and attitude errors.

A single (') and double (") apostrophe denotes particular elements of a vector component along the spacecraft axis.

The quadrant for the angles corresponding to the inverse trigonometric functions $\tan^{-1}(\)$ is determined by the sign of the numerator and denominator of the term in the brackets. When both numerator and denominator are positive, the angle is in the first quadrant; when the numerator is positive and the denominator is negative, the angle falls in the second quadrant; when both numerator and denominator are negative, the angle falls in the third quadrant; and when the numerator is negative and the denominator is positive, the angle falls in the fourth quadrant.

All square root terms in this analysis are principal, positive values. These values may be positive real or positive imaginary numbers.

V. SUMMARY

The assumption of small changes in the inertia parameters has been used to derive approximate rotational equations of motion for arbitrary spinning spacecraft in the small angle and rate regime. Complex representations are introduced to define the rate and attitude errors produced by applied disturbances, and analytic solutions are obtained for the steady spinning mode and for the spinup and despin mode.

Solutions for the steady spinning mode consider both the uncontrolled and the controlled spacecraft motion for characteristic disturbances. These disturbances include initial errors, externally applied torques, and instantaneous and periodic mass motions within the spacecraft. The errors induced by the disturbances are described by the error component time histories, and by vector traces of the complex error representations. Upper bounds of the errors are developed for the uncontrolled case, and the required control techniques and control systems are examined for the controlled case.

Solutions for the spinup and despin mode consider extensible spacecraft modules connected by struts or cables. Fuel consumption relations are derived for several extension techniques, and optimization of the extension techniques is shown to yield appreciable fuel savings.

Comparisons of the analytical solutions and exact solutions obtained by numerical integration of the complete equations of motion are found to be in excellent agreement, and the applications of the approximate solution are illustrated for a manned orbital research laboratory and a large spinning space station.

VI. INTRODUCTION

Proposed spacecraft, such as the manned orbital laboratory (ref. 1) and manned interplanetary vehicles (ref. 2), may use rotation about a maximum axis of inertia to provide spin stabilization and to produce artificial gravity for the crew. These spacecraft will be subjected to variable torques arising from both internal and external sources (ref. 3) and will undergo wobbling motions as a result of these torques. Since the wobbling motions (ref. 4) produce attitude errors (which may affect the spacecraft's power system and experiments) and oscillatory rates (which may lead to discomfort and nausea of the crew), an analysis is required to determine the magnitude of any such attitude errors and body rates for the spacecraft under consideration.

In order to carry out this analysis, the spacecraft's equations of motion with varying inertias and torques must be integrated to define the spacecraft response for the anticipated applied disturbances. In the past, such a solution has required high-speed computing equipment for the numerical integration of the equations of motion and has consumed a large amount of computer time to assess the effects of a range of disturbances for a particular vehicle configuration.

Because of the rather limited application of these results, an approximate analytical solution of the spacecraft's equations of motion would be of considerable value. The closed form solution could be used to determine attitude errors and body rates introduced by "worst case" type of disturbances and would define instability trends that might

result from applied torques. In addition, such a solution would allow a direct evaluation of the effects of changes in both the spacecraft's configuration and the disturbances on the spacecraft's motion.

Approximate analytical solutions of the equations of motion for an arbitrary rotating spacecraft may be obtained for linearized governing equations and Euler angle transformations. A number of such solutions have been obtained for the simplified equations of motion corresponding to symmetric or near-symmetric spacecraft. Leon (ref. 5) and Thomson (ref. 6) have developed attitude and rate relations for spinning near-symmetrical bodies by considering a vectorial representation of the total errors. Thomson and Fung (ref. 7) have also investigated the stability of near-symmetric spinning space stations and have defined regions of instability for an example vehicle. In addition, Hackler (ref. 8), Buglia (ref. 9), and Loebel (ref. 10) have derived expressions for the attitude and rate histories of symmetrical spacecraft by linearizing the equations of motion.

Several analytical solutions for a nonsymmetric spinning body with constant inertias have also been obtained. Exact solutions for a torque-free body were developed by Routh (ref. 11) and MacMillan (ref. 12) in terms of Poincot's construction and elliptic functions and by Whitbeck (ref. 13) in terms of a phase plane approach. An approximate method which shows good agreement between the nonlinear and linearized results for a vehicle under applied torques was presented by Suddath (ref. 14).

Various other analytical approximations are discussed in the literature (refs. 15-20). Existing solutions, however, have considered either

very special cases of nonsymmetric spacecraft or have been restricted to particular symmetric or near-symmetric spacecraft with specified disturbances. Such results cannot be applied to the general case of a nonsymmetric spacecraft with varying products of inertia and applied torques, and offer little information on the properties of the motion of such spacecraft. Furthermore, the form of these solutions has made the determination of upper limits for the total attitude and rate errors difficult since the amount of computational time required to define the error boundaries is in general prohibitive.

The present analysis develops a solution technique for arbitrary rotating spacecraft with variable disturbance functions. The complete equations of motion for nonsymmetric vehicles are linearized and solved with time varying forcing functions and products of inertia. General and particular solution functions are determined and are used to generate rate and attitude expressions corresponding to the variable forcing functions. A complex vector representation is introduced to define both error time histories in component form and the total angular and rate errors.

A number of disturbances are considered for both nonsymmetric and symmetric spacecraft; and the corresponding solutions are examined for the uncontrolled and controlled cases. Upper bounds of the total errors are defined and body-fixed and inertial traces of the total errors are analyzed. A method of selecting control commands is also presented.

VII. PROBLEM FORMULATION

A. Spacecraft Motion

The rotating spacecraft will be related to the reference system shown in figure 1. A set of $X Y Z$ axes fixed to the spacecraft is used to describe the rotational motion of the spacecraft with respect to a set of intermediate $X_I Y_I Z_I$ coordinates. The intermediate coordinates translate without rotation in inertial space, but always remain parallel to a set of $X_F Y_F Z_F$ axes fixed in inertial space.

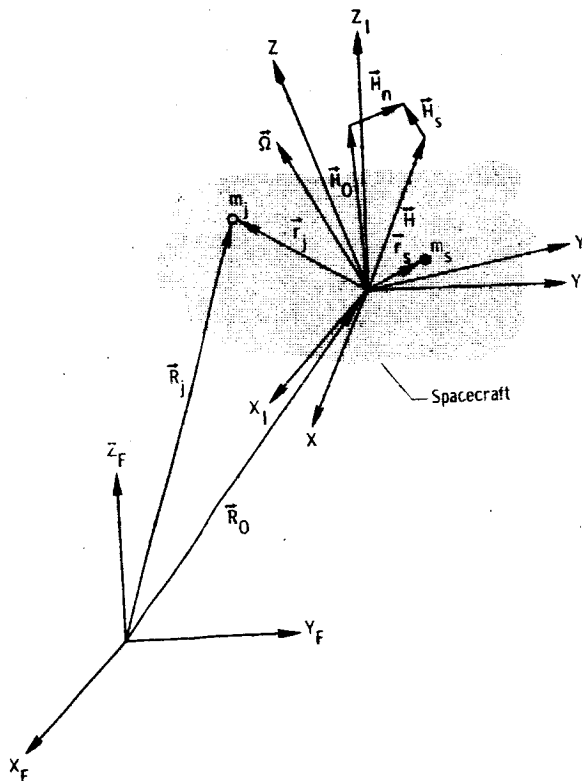


Figure 1.- Reference system for rotating spacecraft.

The inertial attitude of the spacecraft may be defined by means of three modified Euler angles which determine the relative motion between

the $X Y Z$ and $X_I Y_I Z_I$ axis systems. These modified Euler angles, as illustrated in figure 2, results from three consecutive rotations. The first rotation, about the Z_I axis, carries the X_I and Y_I axes through an angle ψ measured in a horizontal plane. The second rotation, about the new Y_I axis, then takes the X_I and Z_I axes through an angle θ measured in a vertical plane. Finally, the third rotation, about the new X_I axis, carries the Y_I and Z_I axes through the angle ϕ measured in an inclined plane to give the X , Y , and Z axes.

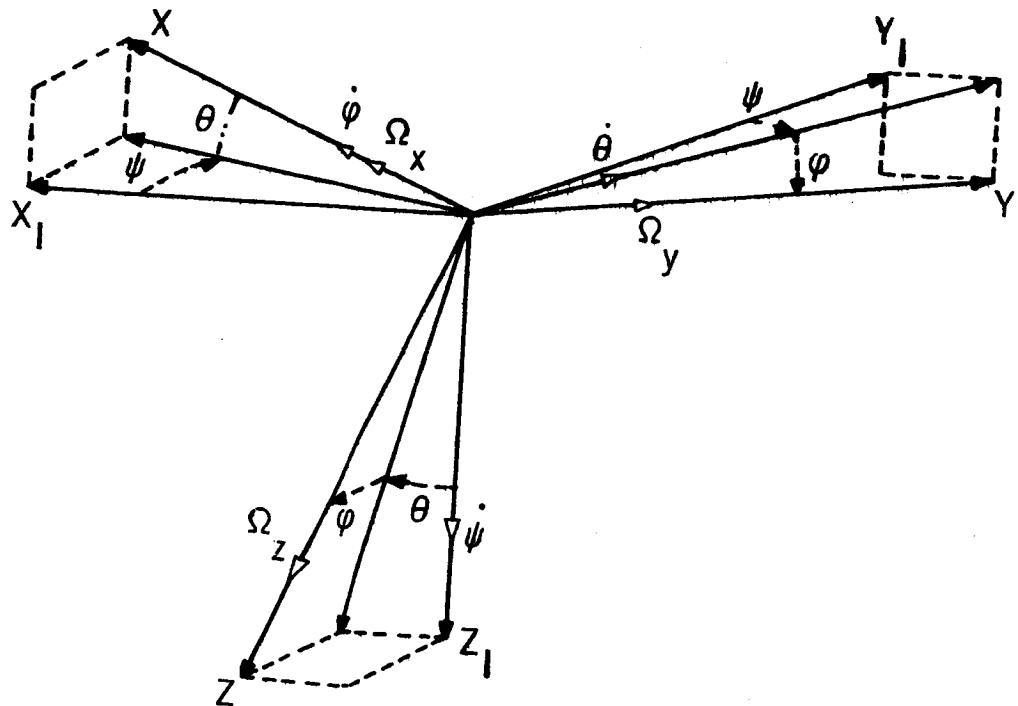


Figure 2.- Vector transformation between spacecraft axes and intermediate reference system.

The modified Euler angles can be determined by expressing the rotations $\dot{\psi}$, $\dot{\theta}$, and $\dot{\phi}$ in terms of the angular rates Ω_x , Ω_y ,

and Ω_z about the vehicle axes. The vehicle angular rates then can be found from a solution of the vehicle moment and force equations. The resultant expressions for Ω_x , Ω_y , and Ω_z are substituted into the Euler angle transformations, which now reduce to differential equations in ψ , θ , ϕ , and t . The solutions of these equations give the attitude of the spacecraft relative to the intermediate axes and thus determine the angular motion of the spacecraft.

B. Assumptions

To make the general nonlinear equations of motion amenable to analytical treatment, the assumptions

$$\left. \begin{array}{ll} \Omega_x \ll \Omega_z & \\ \Omega_y \ll \Omega_z & \\ \sin \theta = \tan \theta = \theta & \cos \theta = 1 \\ \sin \phi = \tan \phi = \phi & \cos \phi = 1 \end{array} \right\} \quad (1)$$

were introduced in the moment, force, and Euler angle relations developed in appendix A. The further assumption that the nondimensional inertia terms associated with any mass particles moving with respect to the spacecraft were small was also made to linearize the equations. The resultant method of reduction to linear form and the range and validity of these assumptions are discussed in appendix A.

C. Governing Equations

With the assumptions of the preceding section, the equations of motion reduce to

$$\begin{aligned} \dot{\Omega}_x + \left[\left(\frac{I_z - I_y}{I_x} \right) \Omega_z \right] \Omega_y = \frac{1}{I_x} \left\{ M_x + \Omega_z (\dot{I}_{xz} - I_{yz} \Omega_z) + \left[\sum_{j=1}^n m_j (z_j \dot{x}_j - x_j \dot{z}_j) \right. \right. \\ \left. \left. - m_s (z_s \dot{x}_s - x_s \dot{z}_s) \right] \Omega_z + \sum_{j=1}^n m_j (z_j \ddot{y}_j - y_j \ddot{z}_j) \right. \\ \left. - m_s (z_s \ddot{y}_s - y_s \ddot{z}_s) \right\} \end{aligned} \quad (2)$$

$$\begin{aligned} \dot{\Omega}_y - \left[\left(\frac{I_z - I_x}{I_y} \right) \Omega_z \right] \Omega_x = \frac{1}{I_y} \left\{ M_y + \Omega_z (\dot{I}_{yz} + I_{xz} \Omega_z) + \left[\sum_{j=1}^n m_j (z_j \dot{y}_j - y_j \dot{z}_j) \right. \right. \\ \left. \left. - m_s (z_s \dot{y}_s - y_s \dot{z}_s) \right] \Omega_z + \sum_{j=1}^n m_j (x_j \ddot{z}_j - z_j \ddot{x}_j) \right. \\ \left. - m_s (x_s \ddot{z}_s - z_s \ddot{x}_s) \right\} \end{aligned} \quad (3)$$

$$\dot{\Omega}_z + \frac{\dot{I}_z}{I_z} \Omega_z = \frac{1}{I_z} \left\{ M_z + \sum_{j=1}^n m_j (y_j \ddot{x}_j - x_j \ddot{y}_j) - m_s (y_s \ddot{x}_s - x_s \ddot{y}_s) \right\} \quad (4)$$

The inertia terms are

$$\left. \begin{aligned} I_x &= I_{x0} + \sum_{j=1}^n m_j (y_{j0}^2 + z_{j0}^2) - m_s (y_{s0}^2 + z_{s0}^2) \\ I_y &= I_{y0} + \sum_{j=1}^n m_j (x_{j0}^2 + z_{j0}^2) - m_s (x_{s0}^2 + z_{s0}^2) \\ I_z &= I_{z0} + \sum_{j=1}^n m_j (x_j^2 + y_j^2) - m_s (x_s^2 + y_s^2) \end{aligned} \right\} \quad (5)$$

$$\left. \begin{aligned} I_{xz} &= \sum_{j=1}^n m_j x_j z_j - m_s x_s z_s \\ I_{yz} &= \sum_{j=1}^n m_j y_j z_j - m_s y_s z_s \end{aligned} \right\} \quad (5)$$

and, consistent with our assumptions, the moments of inertia are taken as constant in (2) and (3), but are allowed to vary in (4). The associated inertia derivatives then become

$$\left. \begin{aligned} \dot{I}_z &= 2 \left[\sum_{j=1}^n m_j (x_j \dot{x}_j + y_j \dot{y}_j) - m_s (x_s \dot{x}_s + y_s \dot{y}_s) \right] \\ \dot{I}_{xz} &= \sum_{j=1}^n m_j (x_j \dot{z}_j + z_j \dot{x}_j) - m_s (x_s \dot{z}_s + z_s \dot{x}_s) \\ \dot{I}_{yz} &= \sum_{j=1}^n m_j (y_j \dot{z}_j + z_j \dot{y}_j) - m_s (y_s \dot{z}_s + z_s \dot{y}_s) \end{aligned} \right\} \quad (6)$$

where x_j , y_j , z_j denote the position coordinates of the mass m_j moving with respect to the spacecraft, and

$$\left. \begin{aligned} x_s &= \sum_{j=1}^n \frac{m_j}{m_s} x_j \\ y_s &= \sum_{j=1}^n \frac{m_j}{m_s} y_j \\ z_s &= \sum_{j=1}^n \frac{m_j}{m_s} z_j \end{aligned} \right\} \quad (7)$$

denote the position coordinates of the composite mass center for the spacecraft and the moving masses.

The spin rate Ω_z is obtained by integrating (4) as

$$\Omega_z = \frac{1}{I_z} \left\{ I_{z0} \Omega_{z0} + \int M_z dt + \int \left[\sum_{j=1}^n m_j (y_j \ddot{x}_j - x_j \ddot{y}_j) - m_s (y_s \ddot{x}_s - x_s \ddot{y}_s) \right] dt \right\} \quad (8)$$

where the first term in the brackets represents the system's initial angular momentum and the remaining terms account for changes in the spin rate due to the applied torque M_z and to the accelerations of the moving masses.

Solutions to the spacecraft equations of motion may be obtained by first determining Ω_z from (8) and then integrating (2) and (3) simultaneously to find Ω_x and Ω_y .

These solutions can be substituted into the linearized Euler angle transformations

$$\dot{\phi} = \Omega_x + \Omega_z \theta \quad (9)$$

$$\dot{\theta} = \Omega_y - \Omega_z \phi \quad (10)$$

$$\dot{\psi} = \Omega_z \quad (11)$$

from which we have

$$\psi = \int \frac{1}{I_z} \left\{ I_{z0} \Omega_{z0} + \int M_z dt + \int \left[\sum_{j=1}^n m_j (y_j \ddot{x}_j - x_j \ddot{y}_j) - m_s (y_s \ddot{x}_s - x_s \ddot{y}_s) \right] dt \right\} dt \quad (12)$$

The solution of (2), (3), (9), and (10) then defines the motion of the spacecraft in terms of the time histories of the body rates and Euler angles.

D. Total Errors

The body rates Ω_x and Ω_y are the undesired rate components produced by the applied disturbances and will be referred to as the rate error components. Similarly, the Euler angles φ and θ describe the unwanted attitude deviations that result from the application of the disturbances. These Euler angles will be referred to as the attitude error components. The solutions for both rate and attitude error components follow directly from the preceding section, and are found as time dependent components along the body and inertial axes.

In practice, one is primarily concerned with the total errors. For example, the time variation and maximum value of the total angular velocity error in body-fixed coordinates must be known to assess possible crew discomfort due to wobbling motions. The time variation and maximum value of the total angular position error with respect to inertial space is needed to determine possible effects on the spacecraft experiments and power system. The effects of removal of a disturbance on the residual spacecraft motion are also of interest.

Both the total angular position and the total body rate errors may be developed by using a complex vector representation (ref. 5). The total angular rate error Ω_{xy} can be obtained by vector addition of the body rates Ω_x and Ω_y , as shown in figure 3.

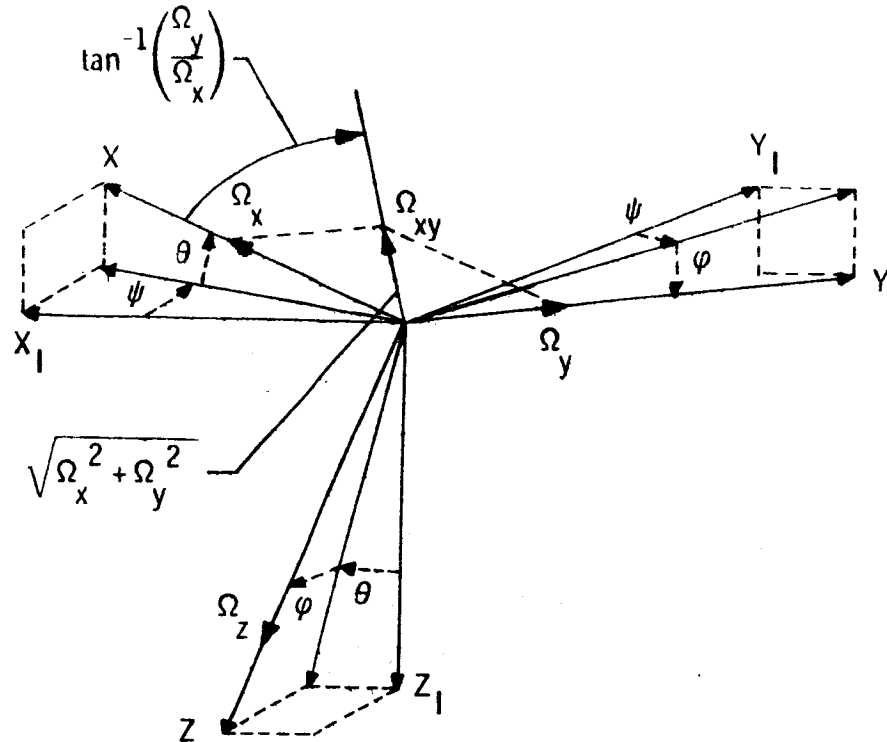


Figure 3.- Vectorial representation of total angular rate error.

Mathematically, Ω_{xy} may be written as

$$\Omega_{xy} = \Omega_x + i\Omega_y = \sqrt{\Omega_x^2 + \Omega_y^2} e^{i \tan^{-1} \left(\frac{\Omega_y}{\Omega_x} \right)} \quad (13)$$

Similarly, the total attitude error α in body-fixed coordinates can be considered as the vector sum of the small Euler angles φ and θ , as illustrated in figure 4. To transform this pseudovector to the intermediate coordinate system, one must rotate the body coordinate system through the angle ψ . The total inertial error α_I is then

$$\alpha_I = \alpha e^{i\psi} = (\varphi + i\theta) e^{i\psi} = \sqrt{\varphi^2 + \theta^2} e^{i \left[\psi + \tan^{-1} \left(\frac{\theta}{\varphi} \right) \right]} \quad (14)$$

Physically, α_I represents the trace of the Z axis projected on the $X_I Y_I$ plane and Ω_{xy} represents the trace of the total rate error vector in the body-fixed XY plane.

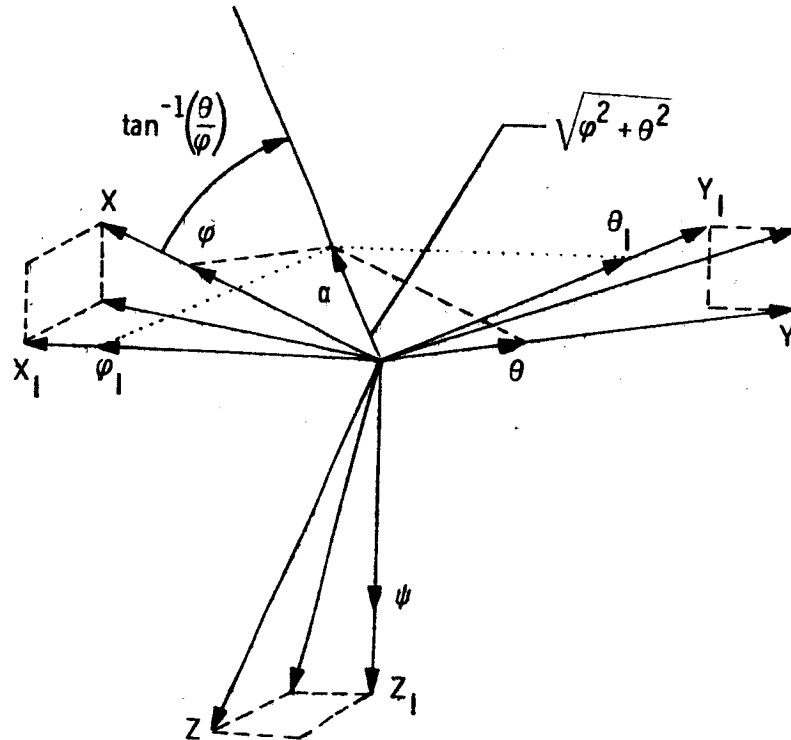


Figure 4.- Pseudovectorial representation of total attitude error.

Differentiation of (14) yields

$$\dot{\alpha}_I = (\dot{\alpha} + i\dot{\psi}\alpha)e^{i\psi} \quad (15)$$

and noting that

$$\dot{\alpha} + i\Omega_Z\alpha = \Omega_{xy} \quad (16)$$

from (9) and (10), one may use (11) to develop the relation

$$\begin{aligned}\dot{\alpha}_I &= (\dot{\alpha} + i\Omega_Z\alpha)e^{i\Omega_Z t} \\ &= \Omega_{xy}e^{i\Omega_Z t}\end{aligned}\tag{17}$$

The magnitude of the rate of change of the inertial attitude error is thus equal to the magnitude of the rate error for the small angle regime.

By integrating (17), one arrives at

$$\alpha_I = \alpha_0 + \int_0^t \Omega_{xy}(\tau)e^{i\Omega_Z(\tau)} d\tau\tag{18}$$

as the solution for the inertial attitude error vector. The attitude error in body coordinates becomes

$$\begin{aligned}\alpha &= \alpha_I e^{-i\Omega_Z t} \\ &= \alpha_0 e^{-i\Omega_Z t} + e^{-i\Omega_Z t} \int_0^t \Omega_{xy}(\tau)e^{i\Omega_Z \tau} d\tau\end{aligned}\tag{19}$$

and both the attitude errors α_I and α can be directly developed from the rate error expression.

If only total error vectors are desired, the time solution of the equations of motion for Ω_{xy} may be followed by application of (18) and (19) to yield α_I and α . If the rate and Euler angle components are of interest, the direct solution of the linear differential equation (2), (3), (9), and (10) is preferable.

In the present analysis, solutions were first developed in the form of time histories for the error components. The transition to the

total error form was then made by substitution of the vector expression for the resultant rate error in (18) and (19).

E. Solution Approach

The solutions of the equations of motion for arbitrary rotating spacecraft can in general be divided into two types, namely those associated with the spinup and despin modes and those associated with the steady spinning mode.

The spinup and despin modes may involve the extension and retraction of cable-connected counterweight modules and thus could have major and rapid changes in the moments of inertia for the spacecraft. During these modes other disturbances, such as crew motions and applied torques, will necessarily be restricted and only the solution for the spin rate and angle, as given by (8) and (12) need be considered. The efficiency of various spinup and despin methods using constant spin rate, constant cable tension, or similar schemes can be readily evaluated from these equations.

For the steady spinning mode, the variations of all total moments of inertia due to the moving masses associated with a particular crew motion are small in comparison with the constant spacecraft inertias I_{x0} , I_{y0} , and I_{z0} . The assumption that the total moments of inertia I_x , I_y , and I_z retain their initial values throughout the crew motion (see appendix A) will be made for this mode.

In addition, disturbance moments due to crew motions and applied torques will now act primarily about the spacecraft X and Y axes. Any

torques about the spacecraft Z axis can be neglected during a particular disturbance since the resultant change (refs. 8, 14, 19) in the spin rate will be small in comparison with the initial spin rate.

In accordance with these assumptions, one may approximate the spin rate by its constant value at the initiation of a particular disturbance

$$\Omega_z = \frac{I_{z0}\Omega_{z0}}{I_z} \equiv \sigma \quad (20)$$

For the evaluation of the effects of that disturbance on the spacecraft motion in the steady spinning mode. The value σ can and will be taken as positive without loss of generality.

Since the spinning mode occurs for the major portion of the spacecraft lifetime, this mode will first be analyzed in considerable detail and several spinup and despin techniques will then be considered in a later chapter.

VIII. ANALYSIS OF SPINNING MODE

For the spinning mode, the moments of inertia take on their initial values immediately after initiation of the disturbance and remain constant for the duration of the disturbance. The inertias may thus be computed from (5) as

$$\left. \begin{aligned} I_x &= I_{x0} + \sum_{j=1}^n m_j(y_{j0}^2 + z_{j0}^2) - m_s(y_{s0}^2 + z_{s0}^2) \\ I_y &= I_{y0} + \sum_{j=1}^n m_j(x_{j0}^2 + z_{j0}^2) - m_s(x_{s0}^2 + z_{s0}^2) \\ I_z &= I_{z0} + \sum_{j=1}^n m_j(x_{j0}^2 + y_{j0}^2) - m_s(x_{s0}^2 + y_{s0}^2) \end{aligned} \right\} \quad (21)$$

and the governing equations may now be developed directly from (2) and (3).

A. Equations of Motion

The equations of motion reduce to

$$\begin{aligned}
 \ddot{\Omega}_x + \left[\left(\frac{I_z - I_y}{I_y} \right) \left(\frac{I_z - I_x}{I_x} \right) \sigma^2 \right] \Omega_x = & \frac{1}{I_x} \dot{M}_x - \left[\left(\frac{I_z - I_y}{I_y} \right) \sigma \dot{M}_y - \left[\left(\frac{I_z - I_y}{I_y} \right) \sigma \left[\dot{i}_{yz} \sigma + I_{xz} \sigma^2 \right] + \left[\ddot{i}_{xz} \sigma - \dot{i}_{yz} \sigma^2 \right] \right] \right. \\
 & + \left[\sum_{j=1}^n m_j (z_j \ddot{x}_j - x_j \ddot{z}_j) - m_s (z_s \ddot{x}_s - x_s \ddot{z}_s) \right] \sigma + \sum_{j=1}^n m_j (z_j \ddot{y}_j + \dot{z}_j \ddot{y}_j) \\
 & - y_j \ddot{z}_j - \dot{y}_j \ddot{z}_j) - m_s (z_s \ddot{y}_s + \dot{z}_s \ddot{y}_s - y_s \ddot{z}_s - \dot{y}_s \ddot{z}_s) \\
 & - \left[\left(\frac{I_z - I_y}{I_y} \right) \sigma \right] \left[\left\{ \sum_{j=1}^n m_j (z_j \dot{y}_j - y_j \dot{z}_j) - m_s (z_s \dot{y}_s - y_s \dot{z}_s) \right\} \sigma \right. \\
 & \left. \left. + \sum_{j=1}^n m_j (x_j \ddot{z}_j - z_j \ddot{x}_j) - m_s (x_s \ddot{z}_s - z_s \ddot{x}_s) \right\} \right]
 \end{aligned} \tag{22}$$

and

$$\begin{aligned}
 \ddot{\Omega}_y + \left[\left(\frac{I_z - I_y}{I_y} \right) \left(\frac{I_z - I_x}{I_x} \right) \sigma^2 \right] \Omega_y = & \frac{1}{I_y} \dot{M}_y + \left[\left(\frac{I_z - I_x}{I_x} \right) \sigma \right] M_x + \left[\left(\frac{I_z - I_x}{I_x} \right) \sigma \right] \left[\dot{I}_{xz} \sigma - I_{yz} \sigma^2 \right] + \left[\ddot{I}_{yz} \sigma + \dot{I}_{xz} \sigma^2 \right] \\
 & + \left[\sum_{j=1}^n m_j (z_j \ddot{y}_j - y_j \ddot{z}_j) - m_s (z_s \ddot{y}_s - y_s \ddot{z}_s) \right] \sigma \\
 & + \sum_{j=1}^n m_j (x_j \ddot{z}_j + \dot{x}_j \ddot{z}_j - z_j \ddot{x}_j - \dot{z}_j \ddot{x}_j) - m_s (x_s \ddot{z}_s + \dot{x}_s \ddot{z}_s - z_s \ddot{x}_s - \dot{z}_s \ddot{x}_s) \\
 & + \left[\left(\frac{I_z - I_x}{I_x} \right) \sigma \right] \left[\left(\sum_{j=1}^n m_j (z_j \dot{x}_j - x_j \dot{z}_j) - m_s (z_s \dot{x}_s - x_s \dot{z}_s) \right) \sigma \right] \\
 & + \left[\sum_{j=1}^n m_j (z_j \ddot{y}_j - y_j \ddot{z}_j) - m_s (z_s \ddot{y}_s - y_s \ddot{z}_s) \right] \sigma
 \end{aligned} \tag{23}$$

For simplicity of notation, introduce the precession rate parameters

$$\left. \begin{aligned} \lambda_x &\equiv \left(\frac{I_z - I_x}{I_x} \right) \sigma \\ \lambda_y &\equiv \left(\frac{I_z - I_y}{I_y} \right) \sigma \\ \lambda^2 &\equiv \lambda_x \lambda_y \end{aligned} \right\} \quad (24)$$

and

so that (22) and (23) become

$$\begin{aligned} \ddot{\Omega}_x + \lambda^2 \Omega_x &= \frac{1}{I_x} \left\{ \dot{M}_x - \lambda_y M_y + \sigma \left[\ddot{I}_{xz} - \dot{I}_{yz}(\sigma + \lambda_y) - I_{xz} \sigma \lambda_y \right] \right. \\ &+ \sum_{j=1}^n m_j \left[(\sigma + \lambda_y)(z_j \ddot{x}_j - x_j \ddot{z}_j) - \sigma \lambda_y (z_j \dot{y}_j - y_j \dot{z}_j) \right. \\ &+ (z_j \ddot{y}_j + \dot{z}_j \ddot{y}_j - y_j \ddot{z}_j - \dot{y}_j \ddot{z}_j) \left. \right] - m_s \left[(\sigma + \lambda_y)(z_s \ddot{x}_s - x_s \ddot{z}_s) \right. \\ &\left. \left. - \sigma \lambda_y (z_s \dot{y}_s - y_s \dot{z}_s) + (z_s \ddot{y}_s + \dot{z}_s \ddot{y}_s - y_s \ddot{z}_s - \dot{y}_s \ddot{z}_s) \right] \right\} \end{aligned}$$

and

$$\begin{aligned} \ddot{\Omega}_y + \lambda^2 \Omega_y &= \frac{1}{I_y} \left\{ \dot{M}_y + \lambda_x M_x + \sigma \left[\ddot{I}_{yz} + \dot{I}_{xz}(\sigma + \lambda_x) - I_{yz} \sigma \lambda_x \right] \right. \\ &+ \sum_{j=1}^n m_j \left[(\sigma + \lambda_x)(z_j \ddot{y}_j - y_j \ddot{z}_j) + \sigma \lambda_x (z_j \dot{x}_j - x_j \dot{z}_j) \right. \\ &+ (x_j \ddot{z}_j + \dot{x}_j \ddot{z}_j - z_j \ddot{x}_j - \dot{z}_j \ddot{x}_j) \left. \right] - m_s \left[(\sigma + \lambda_x)(z_s \ddot{y}_s - y_s \ddot{z}_s) \right. \\ &\left. \left. + \sigma \lambda_x (z_s \dot{x}_s - x_s \dot{z}_s) + (x_s \ddot{z}_s + \dot{x}_s \ddot{z}_s - z_s \ddot{x}_s - \dot{z}_s \ddot{x}_s) \right] \right\} \end{aligned}$$

or

$$\ddot{\Omega}_x + \lambda^2 \Omega_x = F_x \quad (25)$$

$$\ddot{\Omega}_y + \lambda^2 \Omega_y = F_y \quad (26)$$

where

$$\begin{aligned} F_x &= \frac{1}{I_x} \left\{ \dot{M}_x - \lambda_y M_y + \sigma \left[\ddot{I}_{xz} - \dot{I}_{yz}(\sigma + \lambda_y) - I_{xz} \sigma \lambda_y \right] \right. \\ &\quad + \sum_{j=1}^n m_j \left[(\sigma + \lambda_y)(z_j \ddot{x}_j - x_j \ddot{z}_j) - \sigma \lambda_y (z_j \dot{y}_j - y_j \dot{z}_j) \right. \\ &\quad + (z_j \ddot{y}_j + \dot{z}_j \dot{y}_j - y_j \ddot{z}_j - \dot{y}_j \dot{z}_j) \left. \right] - m_s \left[(\sigma + \lambda_y)(z_s \ddot{x}_s - x_s \ddot{z}_s) \right. \\ &\quad \left. \left. - \sigma \lambda_y (z_s \dot{y}_s - y_s \dot{z}_s) + (z_s \ddot{y}_s + \dot{z}_s \dot{y}_s - y_s \ddot{z}_s - \dot{y}_s \dot{z}_s) \right] \right\} \\ &= \frac{1}{I_x} \left\{ \dot{M}_x - \lambda_y M_y + \sum_{j=1}^n m_j \left[z_j \left\{ \ddot{y}_j + (2\sigma + \lambda_y) \ddot{x}_j - \sigma(\sigma + 2\lambda_y) \dot{y}_j \right. \right. \right. \\ &\quad \left. \left. - \sigma^2 \lambda_y x_j \right\} + \dot{z}_j \left\{ \ddot{y}_j + 2\sigma \dot{x}_j - \sigma^2 y_j \right\} - \ddot{z}_j \left\{ \dot{y}_j + \lambda_y x_j \right\} \right. \right. \\ &\quad \left. \left. - \ddot{z}_j y_j \right] - m_s \left[z_s \left\{ \ddot{y}_s + (2\sigma + \lambda_y) \ddot{x}_s - \sigma(\sigma + 2\lambda_y) \dot{y}_s - \sigma^2 \lambda_y x_s \right\} \right. \right. \\ &\quad \left. \left. + \dot{z}_s \left\{ \ddot{y}_s + 2\sigma \dot{x}_s - \sigma^2 y_s \right\} - \ddot{z}_s \left\{ \dot{y}_s + \lambda_y x_s \right\} - \ddot{z}_s y_s \right] \right\} \quad (27) \end{aligned}$$

and

$$\begin{aligned}
 F_y &= \frac{1}{I_y} \left\{ \dot{M}_y + \lambda_x M_x + \sigma \left[\ddot{I}_{yz} + \dot{I}_{xz}(\sigma + \lambda_x) - I_{yz}\sigma\lambda_x \right] \right. \\
 &\quad + \sum_{j=1}^n m_j \left[(\sigma + \lambda_x)(z_j \ddot{y}_j - y_j \ddot{z}_j) + \sigma\lambda_x(z_j \dot{x}_j - x_j \dot{z}_j) \right. \\
 &\quad \left. + (x_j \ddot{z}_j + \dot{x}_j \dot{z}_j - z_j \ddot{x}_j - \dot{z}_j \dot{x}_j) \right] - m_s \left[(\sigma + \lambda_x)(z_s \ddot{y}_s - y_s \ddot{z}_s) \right. \\
 &\quad \left. + \sigma\lambda_x(z_s \dot{x}_s - x_s \dot{z}_s) + (x_s \ddot{z}_s + \dot{x}_s \dot{z}_s - z_s \ddot{x}_s - \dot{z}_s \dot{x}_s) \right] \Big\} \\
 &= \frac{1}{I_y} \left\{ \dot{M}_y + \lambda_x M_x - \sum_{j=1}^n m_j \left[z_j \left\{ \ddot{x}_j - (2\sigma + \lambda_x) \ddot{y}_j - \sigma(\sigma + 2\lambda_x) \dot{x}_j \right. \right. \right. \\
 &\quad \left. \left. + \sigma^2 \lambda_x y_j \right\} + \dot{z}_j \left\{ \ddot{x}_j - 2\sigma \dot{y}_j - \sigma^2 x_j \right\} - \ddot{z}_j \left\{ \dot{x}_j - \lambda_x y_j \right\} - \ddot{z}_j x_j \right] \right. \\
 &\quad + m_s \left[z_s \left\{ \ddot{x}_s - (2\sigma + \lambda_x) \ddot{y}_s - \sigma(\sigma + 2\lambda_x) \dot{x}_s + \sigma^2 \lambda_x y_s \right\} \right. \\
 &\quad \left. \left. + \dot{z}_s \left\{ \ddot{x}_s - 2\sigma \dot{y}_s - \sigma^2 x_s \right\} - \ddot{z}_s \left\{ \dot{x}_s - \lambda_x y_s \right\} - \ddot{z}_s x_s \right] \right\} \quad (28)
 \end{aligned}$$

Adding (25) and (26) in quadrature and referring to (13) yields

$$\ddot{\Omega}_{xy} + \lambda^2 \Omega_{xy} = F \quad (29)$$

with

$$F = F_x + iF_y \quad (30)$$

The solution of (29) is

$$\Omega_{xy} = \frac{\dot{\Omega}_{xy0}}{\lambda} \sin \lambda t + \Omega_{xy0} \cos \lambda t + \bar{F} \quad (31)$$

where \bar{F} is obtained by replacing functions of t in F by the corresponding particular solution functions given in appendix B.

The initial conditions at $t = 0$ are

$$\left. \begin{aligned} \Omega_{xy0} &= \Omega_{xo} + i\Omega_{yo} \\ \dot{\Omega}_{xy0} &= -\left(\frac{\lambda_y I_y}{I_x}\right)\Omega_{yo} + i\left(\frac{\lambda_x I_x}{I_y}\right)\Omega_{xo} \end{aligned} \right\} \quad (32)$$

The particular contributions of an applied disturbance to the initial errors are included in the Laplace formulation of the solution terms.

Substitution of (32) into (31) then results in expressions for the total error Ω_{xy} and its components Ω_x and Ω_y . The spin rate Ω_z is found from

$$\Omega_z = \frac{I_{z0}\Omega_{z0}}{I_z} \equiv \sigma$$

and all of the body rates have thus been defined.

The Euler angle differential equations can be written as

$$\left. \begin{aligned} \ddot{\varphi} + \sigma^2 \varphi &= \dot{\Omega}_x + \sigma \Omega_y \\ \ddot{\theta} + \sigma^2 \theta &= \dot{\Omega}_y - \sigma \Omega_x \end{aligned} \right\} \quad (33)$$

and after adding in quadrature

$$\ddot{\alpha} + \sigma^2 \alpha = \dot{\Omega}_{xy} - i\sigma \Omega_{xy} \quad (34)$$

Substitution for the rate error yields

$$\ddot{\alpha} + \sigma^2 \alpha = \left[\lambda \Omega_{xy0} - \frac{i\sigma \dot{\Omega}_{xy0}}{\lambda} \right] \sin \lambda t + \left[\dot{\Omega}_{xy0} - i\sigma \Omega_{xy0} \right] \cos \lambda t + \ddot{\bar{F}} - i\sigma \bar{F} \quad (35)$$

which has the solution

$$\alpha = \frac{\dot{\alpha}_0}{\sigma} \sin \sigma t + \alpha_0 \cos \sigma t + \frac{1}{\sigma^2 - \lambda^2} \left\{ \left[\lambda \Omega_{xy0} - \frac{i\sigma \dot{\Omega}_{xy0}}{\lambda} \right] \left[\sin \lambda t - \frac{\lambda}{\sigma} \sin \sigma t \right] + \left[\dot{\Omega}_{xy0} - i\sigma \Omega_{xy0} \right] \left[\cos \lambda t - \cos \sigma t \right] \right\} + \frac{\ddot{\bar{F}}}{\sigma} - i\sigma \bar{F} \quad (36)$$

where $\ddot{\bar{F}}$ and \bar{F} are obtained by replacing functions of t in F by the corresponding particular solution functions of appendix B.

Initial conditions at $t = 0$ are

$$\left. \begin{aligned} \alpha_0 &= \varphi_0 + i\theta_0 \\ \dot{\alpha}_0 &= \Omega_{xy0} - i\sigma \alpha_0 \end{aligned} \right\} \quad (37)$$

and the Euler angle ψ can be determined from the relation

$$\psi = \sigma t \quad (38)$$

This completes the development of the Euler angles.

Since the terms involving the initial errors will have the same form for all disturbances, introduce

$$\tilde{\Omega}_{xy} \equiv \tilde{\Omega}_x + i\tilde{\Omega}_y = \frac{\dot{\Omega}_{xy0}}{\lambda} \sin \lambda t + \Omega_{xy0} \cos \lambda t$$

and

(39)

$$\begin{aligned}\tilde{\alpha} \equiv \tilde{\varphi} + i\tilde{\theta} = & \frac{1}{\sigma} \left\{ \dot{\alpha}_0 - \left[\frac{\lambda^2 \Omega_{xy0} - i\sigma \dot{\Omega}_{xy0}}{\sigma^2 - \lambda^2} \right] \right\} \sin \sigma t \\ & + \left\{ \alpha_0 - \left[\frac{\dot{\Omega}_{xy0} - i\sigma \Omega_{xy0}}{\sigma^2 - \lambda^2} \right] \right\} \cos \sigma t \\ & + \frac{1}{\sigma^2 - \lambda^2} \left\{ \left[\lambda \Omega_{xy0} - \frac{i\sigma \dot{\Omega}_{xy0}}{\lambda} \right] \sin \lambda t \right. \\ & \left. + \left[\dot{\Omega}_{xy0} - i\sigma \Omega_{xy0} \cos \lambda t \right] \right\}\end{aligned}$$

or in component form

$$\tilde{\Omega}_x = \Omega_{x0} \cos \lambda t - \left(\frac{\lambda_y I_y}{\lambda I_x} \right) \Omega_{y0} \sin \lambda t$$

(40)

$$\tilde{\Omega}_y = \Omega_{y0} \cos \lambda t + \left(\frac{\lambda_x I_x}{\lambda I_y} \right) \Omega_{x0} \sin \lambda t$$

while

$$\begin{aligned}\tilde{\varphi} = & \left[\varphi_0 - \frac{I_y \Omega_{y0}}{\sigma I_z} \right] \cos \sigma t + \left[\theta_0 + \frac{I_x \Omega_{x0}}{\sigma I_z} \right] \sin \sigma t \\ & + \left[\frac{I_y \Omega_{y0}}{\sigma I_z} \right] \cos \lambda t + \left[\frac{I_x \lambda_x \Omega_{x0}}{\sigma \lambda I_z} \right] \sin \lambda t\end{aligned}$$

and

(41)

$$\begin{aligned}\tilde{\theta} = & \left[\theta_0 + \frac{I_x \Omega_{x0}}{\sigma I_z} \right] \cos \sigma t - \left[\varphi_0 - \frac{I_y \Omega_{y0}}{\sigma I_z} \right] \sin \sigma t \\ & - \left[\frac{I_x \Omega_{x0}}{\sigma I_z} \right] \cos \lambda t + \left[\frac{I_y \lambda_y \Omega_{y0}}{\sigma I_z} \right] \sin \lambda t\end{aligned}$$

All coefficients in these equations may be evaluated from the initial conditions Ω_{x0} , Ω_{y0} , σ , φ_0 , θ_0 , and the initial moments of inertia.

The terms involving the applied disturbances can be similarly put into component form, so that the body rates and Euler angles can be found by equating real and imaginary parts in

$$\Omega_{xy} = \Omega_x + i\Omega_y = \tilde{\Omega}_{xy} + \bar{F}$$

and

(42)

$$\alpha = \varphi + i\theta = \tilde{\alpha} + \dot{\bar{F}} - i\sigma\bar{F}$$

where \bar{F} , $\dot{\bar{F}}$, and $\dot{\bar{F}}$ are taken from appendix B.

B. Total Errors

The total rate and attitude errors may be put into a somewhat simpler form by expressing all trigonometric terms occurring in these errors in exponential form. Thus, one is able to obtain

$$\Omega_{xy} = \sum_{j=1}^f \sum_{h=0}^g B_j t^h e^{i\beta_j t} \quad (43)$$

where j and h vary over a finite range of integers. The complex constants B_j and the real constants β_j must be evaluated for a particular disturbance.

The total angular error in inertial space, as defined by equation (14) can be similarly expressed as

$$\alpha_I = (\varphi + i\theta)e^{i\psi} = \sum_{j=1}^u \sum_{h=0}^v C_j t^h e^{i\gamma_j t} \quad (44)$$

where j and h again remain finite integers with C_j and γ_j determined for a specified disturbance.

In engineering applications, one is also interested in the maximum magnitudes of these errors. Since the exact solution for the maximum error magnitudes requires an iterative determination of the zeros of the magnitude derivative - and this requires considerable computing time - an alternate method of defining upper bounds for the errors is preferable from the practical standpoint. It is noted from (43) that

$$\begin{aligned} |\Omega_{xy}| &= \left| \sum_{j=1}^f \sum_{h=0}^g B_j t^h e^{i\beta_j t} \right| \\ &\leq \sum_{j=1}^f \sum_{h=0}^g |B_j t^h| \\ &\leq \sum_{j=1}^f \sum_{h=0}^g |B_j| |t^h| \equiv |\Omega_{xy}|_{lim} \end{aligned} \quad (45)$$

and similarly from (44) that

$$\begin{aligned} |\alpha_I| = |\alpha| &= \left| \sum_{j=1}^u \sum_{h=0}^v C_j t^h e^{i\gamma_j t} \right| \\ &\leq \sum_{j=1}^u \sum_{h=0}^v |C_j t^h| \\ &\leq \sum_{j=1}^u \sum_{h=0}^v |C_j| |t^h| \equiv |\alpha|_{lim} \end{aligned} \quad (46)$$

These upper bounds provide limiting values of the error magnitudes which are adequate for assessing the effects of particular disturbances. More accurate estimates of the absolute maximum errors and their directions can be obtained from polar plots of the complex errors if desired.

C. Characteristic Disturbances for Nonsymmetric Spacecraft

Most disturbances acting on rotating spacecraft may be approximated by impulsive torques, step torques, step products of inertia, or variable products of inertia. For example, docking impacts and attitude control moments can be represented by impulsive or step torques, while crew or cargo motions would result in either step or variable products of inertia. Other externally applied torques (such as the sinusoidal gravity gradient moments) are dependent on the particular spacecraft and orbital characteristics and cannot be defined without selecting a specific vehicle and orientation.

The effects of characteristic disturbing functions on the spacecraft motion are presented in this section. Time solutions for the Euler angle and body rate errors are developed for arbitrary constant moments of inertia, and upper bounds for these variables are given.

1. Impulsive Torques

a. Time Histories

Docking impulses caused by resupply and rendezvous vehicles or micrometeorite hits may result in impulsive torques acting on the spacecraft. These torques can be written as

$$M \equiv M_x + iM_y = (T_x + iT_y)\delta(t) \quad (47)$$

and the corresponding forcing function is

$$F = \frac{1}{I_x} \left[T_x \dot{\delta}(t) - \lambda_y T_y \delta(t) \right] + \frac{1}{I_y} \left[T_y \dot{\delta}(t) + \lambda_x T_x \delta(t) \right] \quad (48)$$

For arbitrary initial conditions, the total rate error may be found from (27), (42), and (48) by using the solution functions given in table I. The results are

$$\Omega_{xy} = \tilde{\Omega}_{xy} + \frac{1}{I_x} \left[T_x \cos \lambda t - \frac{T_y \lambda_y}{\lambda} \sin \lambda t \right] + \frac{1}{I_y} \left[T_y \cos \lambda t + \frac{T_x \lambda_x}{\lambda} \sin \lambda t \right] \quad (49)$$

where $\tilde{\Omega}_{xy}$ is given by (39) and (40).

The attitude error can be similarly determined as

$$\alpha = \tilde{\alpha} + \frac{1}{I_z \sigma} \left\{ \left[T_y (\cos \lambda t - \cos \sigma t) + T_x \left(\frac{\lambda_x}{\lambda} \sin \lambda t + \sin \sigma t \right) \right] - i \left[T_x (\cos \lambda t - \cos \sigma t) - T_y \left(\frac{\lambda_y}{\lambda} \sin \lambda t + \sin \sigma t \right) \right] \right\} \quad (50)$$

with $\tilde{\alpha}$ determined from (39) and (41).

b. Total Errors

Conversion of the total angular and rate error to exponential form leads to the complex vector representation

$$\Omega_{xy} = \Omega_x + i\Omega_y = \tilde{\Omega}_{xy} + B_3 e^{i\lambda t} + B_4 e^{-i\lambda t} \quad (51)$$

where

$$\tilde{\Omega}_{xy} = B_1 e^{i\lambda t} + B_2 e^{-i\lambda t} \quad (52)$$

and the complex constants B_j are given by

$$\begin{aligned}
 B_1 &= \left\{ \frac{1}{2} \left[\frac{1}{I_x \sqrt{\lambda_x}} + \frac{1}{I_y \sqrt{\lambda_y}} \right] \sqrt{\left(I_x \Omega_{x0} \sqrt{\lambda_x} \right)^2 + \left(I_y \Omega_{y0} \sqrt{\lambda_y} \right)^2} \right\} e^{i \tan^{-1} \left[\frac{I_y \Omega_{y0} \sqrt{\lambda_y}}{I_x \Omega_{x0} \sqrt{\lambda_x}} \right]} \\
 B_2 &= \left\{ \frac{1}{2} \left[\frac{1}{I_x \sqrt{\lambda_x}} - \frac{1}{I_y \sqrt{\lambda_y}} \right] \sqrt{\left(I_x \Omega_{x0} \sqrt{\lambda_x} \right)^2 + \left(I_y \Omega_{y0} \sqrt{\lambda_y} \right)^2} \right\} e^{-i \tan^{-1} \left[\frac{I_y \Omega_{y0} \sqrt{\lambda_y}}{I_x \Omega_{x0} \sqrt{\lambda_x}} \right]} \\
 B_3 &= \left\{ \frac{1}{2} \left[\frac{1}{I_x \sqrt{\lambda_x}} + \frac{1}{I_y \sqrt{\lambda_y}} \right] \sqrt{\left(T_x \sqrt{\lambda_x} \right)^2 + \left(T_y \sqrt{\lambda_y} \right)^2} \right\} e^{i \tan^{-1} \left[\frac{T_y \sqrt{\lambda_y}}{T_x \sqrt{\lambda_x}} \right]} \\
 B_4 &= \left\{ \frac{1}{2} \left[\frac{1}{I_x \sqrt{\lambda_x}} - \frac{1}{I_y \sqrt{\lambda_y}} \right] \sqrt{\left(T_x \sqrt{\lambda_x} \right)^2 + \left(T_y \sqrt{\lambda_y} \right)^2} \right\} e^{-i \tan^{-1} \left[\frac{T_y \sqrt{\lambda_y}}{T_x \sqrt{\lambda_x}} \right]}
 \end{aligned} \tag{53}$$

and

The angular error α_I can be developed directly by substitution of (52) and (53) into (18). The result is

$$\alpha_I = (\varphi + i\theta) e^{i\sigma t} = \tilde{\alpha}_I + i \left[C_4 + C_5 e^{i(\sigma+\lambda)t} + C_6 e^{i(\sigma-\lambda)t} \right] \tag{54}$$

where

$$\tilde{\alpha}_I = \tilde{\alpha} e^{i\sigma t} = \alpha_0 + i \left[C_1 + C_2 e^{i(\sigma+\lambda)t} + C_3 e^{i(\sigma-\lambda)t} \right] \quad (55)$$

and the constants are

$$\begin{aligned} \alpha_0 &= \sqrt{\varphi_0^2 + \theta_0^2} e^{-i(\frac{\theta_0}{\varphi_0})} \\ C_1 &= \left\{ \frac{1}{\sigma I_z} \sqrt{(I_x \Omega_{x0})^2 + (I_y \Omega_{y0})^2} \right\} e^{i \tan^{-1} \left(\frac{I_y \Omega_{y0}}{I_x \Omega_{x0}} \right)} \\ C_2 &= \left\{ \frac{-1}{2\sigma I_z} \left[\frac{1}{\sqrt{\lambda_x}} + \frac{1}{\sqrt{\lambda_y}} \right] \sqrt{(I_x \Omega_{x0} \sqrt{\lambda_x})^2 + (I_y \Omega_{y0} \sqrt{\lambda_y})^2} \right\} e^{i \tan^{-1} \left(\frac{I_y \Omega_{y0} \sqrt{\lambda_y}}{I_x \Omega_{x0} \sqrt{\lambda_x}} \right)} \\ C_3 &= \left\{ \frac{-1}{2\sigma I_z} \left[\frac{1}{\sqrt{\lambda_x}} - \frac{1}{\sqrt{\lambda_y}} \right] \sqrt{(I_x \Omega_{x0} \sqrt{\lambda_x})^2 + (I_y \Omega_{y0} \sqrt{\lambda_y})^2} \right\} e^{-i \tan^{-1} \left(\frac{I_y \Omega_{y0} \sqrt{\lambda_y}}{I_x \Omega_{x0} \sqrt{\lambda_x}} \right)} \\ C_4 &= \left\{ \frac{1}{\sigma I_z} \sqrt{T_x^2 + T_y^2} \right\} e^{i \tan^{-1} \left(\frac{T_y}{T_x} \right)} \\ C_5 &= \left\{ \frac{-1}{2\sigma I_z} \left[\frac{1}{\sqrt{\lambda_x}} + \frac{1}{\sqrt{\lambda_y}} \right] \sqrt{(T_x \sqrt{\lambda_x})^2 + (T_y \sqrt{\lambda_y})^2} \right\} e^{i \tan^{-1} \left(\frac{T_y \sqrt{\lambda_y}}{T_x \sqrt{\lambda_x}} \right)} \\ C_6 &= \left\{ \frac{-1}{2\sigma I_z} \left[\frac{1}{\sqrt{\lambda_x}} - \frac{1}{\sqrt{\lambda_y}} \right] \sqrt{(T_x \sqrt{\lambda_x})^2 + (T_y \sqrt{\lambda_y})^2} \right\} e^{-i \tan^{-1} \left(\frac{T_y \sqrt{\lambda_y}}{T_x \sqrt{\lambda_x}} \right)} \end{aligned} \quad (56)$$

and

c. Initial Error Contribution

The total errors $\tilde{\Omega}_{xy}$ and $\tilde{\alpha}_I$ which correspond to the initial conditions Ω_{x0} , Ω_{y0} , σ , Φ_0 , and θ_0 will be considered first. A simple geometrical interpretation of these error traces is possible. For $\tilde{\Omega}_{xy}$ this interpretation follows from the trace of the velocity error in the XY body axis plane, as shown in figure 5.

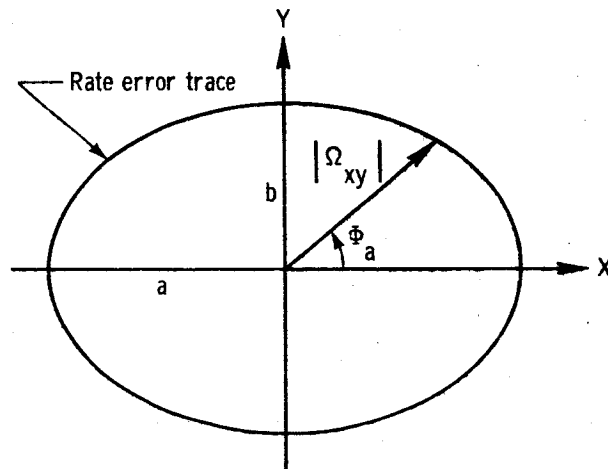


Figure 5.- Rate error trace for initial conditions.

The path described by the tip of the $\tilde{\Omega}_{xy}$ vector is an ellipse in the body-fixed plane.

The characteristics of this ellipse are derived from an examination of (52) and (53). The semiaxes a and b are determined as

$$\left. \begin{aligned} a &= \frac{1}{I_x \sqrt{\lambda_x}} \sqrt{(I_x \Omega_{x0} \sqrt{\lambda_x})^2 + (I_y \Omega_{y0} \sqrt{\lambda_y})^2} \\ b &= \frac{1}{I_y \sqrt{\lambda_y}} \sqrt{(I_x \Omega_{x0} \sqrt{\lambda_x})^2 + (I_y \Omega_{y0} \sqrt{\lambda_y})^2} \end{aligned} \right\} \quad (57)$$

and the angular position of the rate error vector is given by

$$\phi_a = \tan^{-1} \left\{ \frac{I_x \sqrt{\lambda_x}}{I_y \sqrt{\lambda_y}} \tan \left[\lambda t + \tan^{-1} \left(\frac{I_y \Omega_{y0} \sqrt{\lambda_y}}{I_x \Omega_{x0} \sqrt{\lambda_x}} \right) \right] \right\} \quad (58)$$

The quadrant for the angles corresponding to the inverse trigonometric functions $\tan^{-1}(\)$ in (58) and in all subsequent equations is determined by the sign of the numerator and denominator of the term in the brackets. When both numerator and denominator are positive, the angle is in the first quadrant; when the numerator is positive and the denominator is negative, the angle falls in the second quadrant; when both numerator and denominator are negative, the angle falls in the third quadrant; and when the numerator is negative and the denominator is positive, the angle falls in the fourth quadrant.

The position of the major axis of the ellipse is determined by the relative magnitude of I_x and I_y . If $I_y > I_x$, then the major axis coincides with the Y body axis and the maximum angular rate occurs about this axis. Conversely, if $I_x > I_y$, then the major axis and the maximum angular rate lie along the X body axis. The period of revolution is $\left| \frac{2\pi}{\lambda} \right|$ and the $\tilde{\Omega}_{xy}$ vector rotates in the direction of the precession rate λ . When I_z is a maximum inertia, this rotation is in the direction of spin; when I_z is a minimum inertia, the rotation is against the direction of spin.

The trace of the rate error vector can be directly compared with the results of Poinot's geometric construction (ref. 12), in which the path of the instantaneous rate vector on the ellipsoid of inertia is

called the polhode. For the present solution the rate vector is restrained to move in a plane normal to the Z axis, which is a principal axis of the inertia ellipsoid. The polhode projection onto this plane has been developed by Thomson (ref. 6, page 124) and yields a curve whose shape is defined by the relation

$$\lambda_x(I_x\Omega_x)^2 + \lambda_y(I_y\Omega_y)^2 = \lambda_x(I_x\Omega_{x0})^2 + \lambda_y(I_y\Omega_{y0})^2 \quad (59)$$

This relation describes an ellipse, with semiaxes given by (57). Since the polhode projection is proportional to the rate vector trace derived in this analysis, the approximate solution will exactly represent the spacecraft rates when the variation in the spin rate is negligible.

The angular trace with respect to the X_I and Y_I axes is illustrated in figure 6.

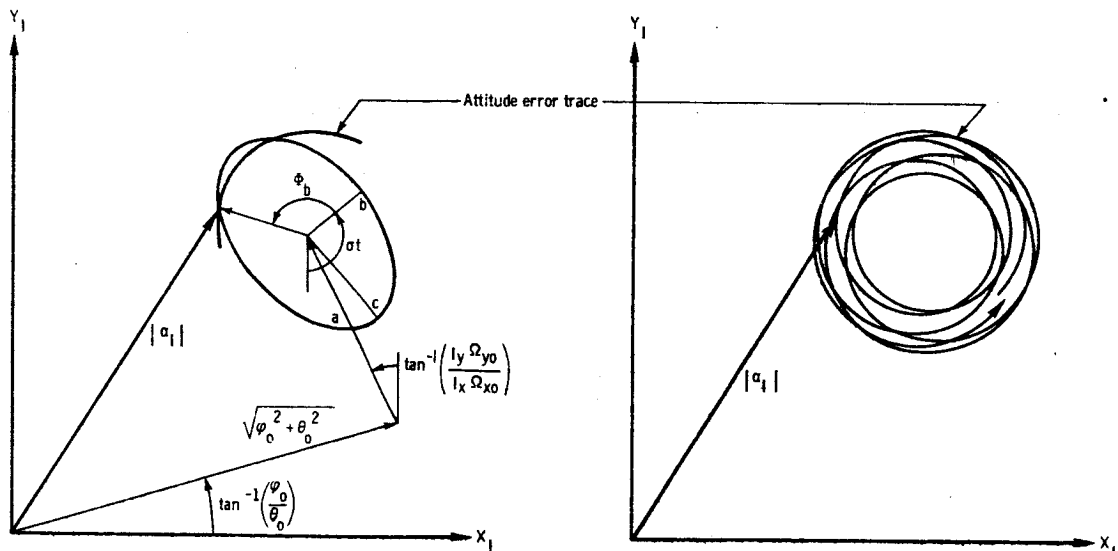


Figure 6.- Attitude error trace for initial conditions.

The path described by the tip of the $\tilde{\alpha}_T$ vector is generated by a point moving on a displaced ellipse, which in turn is rotating at the spin rate. From (55) and (56), the center of the moving ellipse is located by the vector sum of the initial attitude error α_0 and of the initial angular momentum ratio term $i \left[\frac{I_x \Omega_{x0} + i I_y \Omega_{y0}}{\sigma I_z} \right]$. The radius a shown on the figure is thus

$$a = \frac{1}{\sigma I_z} \sqrt{(I_x \Omega_{x0})^2 + (I_y \Omega_{y0})^2} \quad (60)$$

while the semiaxes of the rotating ellipse become

$$\left. \begin{aligned} b &= \frac{1}{\sigma I_z \sqrt{\lambda_x}} \sqrt{(I_x \Omega_{x0} \sqrt{\lambda_x})^2 + (I_y \Omega_{y0} \sqrt{\lambda_y})^2} \\ c &= \frac{1}{\sigma I_z \sqrt{\lambda_y}} \sqrt{(I_x \Omega_{x0} \sqrt{\lambda_x})^2 + (I_y \Omega_{y0} \sqrt{\lambda_y})^2} \end{aligned} \right\} \quad (61)$$

and the precession of the attitude error vector within the ellipse is specified by the angle

$$\Phi_b = \tan^{-1} \left\{ \sqrt{\frac{\lambda_x}{\lambda_y}} \tan \left[\lambda t + \tan^{-1} \left(\frac{I_y \Omega_{y0} \sqrt{\lambda_y}}{I_x \Omega_{x0} \sqrt{\lambda_x}} \right) \right] \right\} \quad (62)$$

When λ is rational, the path of the attitude error trace is closed and has a period of $2k\pi$, where k is the least common denominator of σ and λ .

The trace of the attitude error vector is in agreement with the general properties predicted by MacMillan (ref. 12) for the torque-free motion of a rigid body with respect to a unit reference sphere. This sphere was drawn about the fixed point of the spinning body as a center;

and the motion of the body Z axis about the fixed-momentum axis was then described by the trace of the Z axis on the unit sphere. The vector trace, introduced in the present analysis, can be considered as the projection of this Z axis trace onto a plane perpendicular to the Z_I axis.

It should be apparent that the Z_I axis which is arbitrarily defined as the fixed space axis corresponding to the initial position of the Z axis, will not generally coincide with the fixed-momentum axis. By assumption, however, the angle between these two axes is small. Hence, the shape of the traces about the fixed-momentum axis should be approximately retained in the plane normal to the Z_I axis. The fixed-momentum axis will appear as a displaced point on this attitude error plane.

In figure 6, the fixed-momentum axis projects as the center of the rotating ellipse. The attitude error oscillates between two concentric circles drawn about the ellipse center. The radii of these circles are given by the minor and major semiaxis of the ellipse. The similarity of this motion with that depicted in figure 61 of MacMillan's test is obvious.

Upper bounds of the values for the rate and attitude error magnitudes, as developed from (45) and (46), are

$$|\Omega_{xy}|_{\lim} = \frac{1}{2} \left[\left| \frac{1}{I_x \sqrt{\lambda_x}} + \frac{1}{I_y \sqrt{\lambda_y}} \right| + \left| \frac{1}{I_x \sqrt{\lambda_x}} - \frac{1}{I_y \sqrt{\lambda_y}} \right| \right] \sqrt{(I_x \Omega_{x0} \sqrt{\lambda_x})^2 + (I_y \Omega_{y0} \sqrt{\lambda_y})^2} \quad (63)$$

and

$$|\alpha|_{\text{lim}} = \sqrt{\phi_0^2 + \theta_0^2} + \frac{1}{\sigma I_z} \sqrt{(I_x \Omega_{x0})^2 + (I_y \Omega_{y0})^2} + \frac{1}{2\sigma I_z} \left[\left| \frac{1}{\sqrt{\lambda_y}} + \frac{1}{\sqrt{\lambda_x}} \right| \right. \\ \left. + \left| \frac{1}{\sqrt{\lambda_y}} - \frac{1}{\sqrt{\lambda_x}} \right| \right] \sqrt{(I_x \Omega_{x0} \sqrt{\lambda_x})^2 + (I_y \Omega_{y0} \sqrt{\lambda_y})^2} \quad (64)$$

The rate limit (63) gives the major semiaxis of the rate error trace and is equal to the maximum rate error. The attitude limit (64) corresponds to the sum of the center radii and the major semiaxis of the attitude ellipse, and will be greater than or equal to the maximum attitude error.

Several interesting trends may be observed from the geometrical development and the relations for the upper limits of the errors. When the spacecraft inertia I_x (or I_y) approaches I_z while the second inertia I_y (or I_x) remains different from I_z , then the rate and attitude ellipses become very elongated. Small rate errors induced about the second inertia axis by impulsive torques or other disturbances can thus lead to large total attitude and rate errors. An example is a cylindrical configuration spinning about an axis normal to the axis of symmetry.

When the spacecraft inertia I_x (or I_y) is very much larger than I_z , excessive attitude errors will be produced by small body rates and tumbling may occur. This result, however, is not surprising since the inplane angular momentum is now much larger than the spin momentum. Examples here are slender cylindrical satellites and missiles spinning about a minimum axis of inertia.

One may note that the smallest errors will be produced when both I_x and I_y are much smaller than I_z , and the spacecraft configuration approaches that of a disk.

The contributions of the errors $\tilde{\Omega}_{xy}$ and $\tilde{\alpha}$ to the limiting errors $|\Omega_{xy}|_{\lim}$ and $|\alpha|_{\lim}$ for a given disturbance will be omitted in the remainder of the analysis to avoid undue complications of the limiting error relations. These error terms could, however, be readily included if this is desirable for a particular disturbance.

d. Impulsive Torque Contribution

If the initial error terms are taken as zero, the total errors for the impulsive torques are equivalent to those for the initial rate error terms. The geometrical representation and the maximum error values for the vectors corresponding to the initial errors will thus hold for the impulsive torques if Ω_{x0} is replaced by $\frac{T_x}{I_x}$, Ω_{y0} is replaced by $\frac{T_y}{I_y}$, and ϕ_0 and θ_0 are taken as zero in (57) - (64) and in figures 5 and 6.

2. Step Torques

a. Time Histories

The spacecraft attitude control system and external sources, such as gravity gradients, may also exert torques about the body axes. For this example, consideration will be given to constant step torques of the form

$$M \equiv M_x + iM_y = (T_x + iT_y)U(t) \quad (65)$$

and the associated forcing function

$$F = \frac{1}{I_x} \left[T_x \delta(t) - \lambda_y T_y U(t) \right] + \frac{1}{I_y} \left[T_y \delta(t) + \lambda_x T_x U(t) \right] \quad (66)$$

The body rate error is found from (21), (42), and (66) by substitution of the solution functions of table 1, and is

$$\begin{aligned} \Omega_{xy} = \tilde{\Omega}_{xy} + \frac{1}{\lambda} \left\{ \frac{1}{I_x} \left[T_x \sin \lambda t - \frac{T_y \lambda_y}{\lambda} (1 - \cos \lambda t) \right] \right. \\ \left. + \frac{1}{I_y} \left[T_y \sin \lambda t + \frac{T_x \lambda_x}{\lambda} (1 - \cos \lambda t) \right] \right\} \quad (67) \end{aligned}$$

The attitude error α is determined in a like manner as

$$\begin{aligned} \alpha = \tilde{\alpha} + \frac{1}{\sigma I_z} \left[\left\{ T_x \left[\frac{1}{\lambda_y} \left(\frac{I_z}{I_y} - \cos \lambda t \right) - \frac{1}{\sigma} \cos \sigma t \right] \right. \right. \\ \left. \left. + T_y \left[\frac{1}{\lambda} \sin \lambda t - \frac{1}{\sigma} \sin \sigma t \right] \right\} \right. \\ \left. + i \left\{ T_y \frac{1}{\lambda_x} \left(\frac{I_z}{I_x} - \cos \lambda t \right) - \frac{1}{\sigma} \cos \sigma t \right. \right. \\ \left. \left. + T_x \left[\frac{1}{\lambda} \sin \lambda t - \frac{1}{\sigma} \sin \sigma t \right] \right\} \right] \quad (68) \end{aligned}$$

The initial error contributions $\tilde{\Omega}_{xy}$ and $\tilde{\alpha}$ are defined as before.

b. Total Errors

A transformation of these components to polar form yields

$$\Omega_{xy} = \tilde{\Omega}_{xy} + B_3 + B_4 e^{i\lambda t} + B_5 e^{-i\lambda t} \quad (69)$$

with

$$\left. \begin{aligned} B_3 &= \left\{ -\sqrt{\left(\frac{T_x}{\lambda_y I_y}\right)^2 + \left(\frac{T_y}{\lambda_x I_x}\right)^2} e^{-i \tan^{-1} \left[\frac{T_x \lambda_x I_x}{T_y \lambda_y I_y} \right]} \right. \\ B_4 &= \left\{ \frac{1}{2} \left[\frac{1}{I_x \sqrt{\lambda_x}} + \frac{1}{I_y \sqrt{\lambda_y}} \right] \sqrt{\frac{T_x^2}{\lambda_y} + \frac{T_y^2}{\lambda_x}} e^{-i \tan^{-1} \left[\frac{T_x \sqrt{\lambda_x}}{T_y \sqrt{\lambda_y}} \right]} \right. \\ B_5 &= \left\{ \frac{1}{2} \left[\frac{1}{I_x \sqrt{\lambda_x}} - \frac{1}{I_y \sqrt{\lambda_y}} \right] \sqrt{\frac{T_x^2}{\lambda_y} + \frac{T_y^2}{\lambda_x}} e^{i \tan^{-1} \left[\frac{T_x \sqrt{\lambda_x}}{T_y \sqrt{\lambda_y}} \right]} \right. \end{aligned} \right\} \quad (70)$$

and

$$\alpha_I = \tilde{\alpha}_I + C_5 + C_6 e^{i(\sigma+\lambda)t} + C_7 e^{i(\sigma-\lambda)t} + C_8 e^{i\sigma t} \quad (71)$$

with

$$\left. \begin{aligned} C_5 &= \left\{ -\frac{1}{\sigma^2 I_z} \sqrt{T_x^2 + T_y^2} e^{i \tan^{-1} \left[\frac{T_y}{T_x} \right]} \right. \\ C_6 &= \left\{ -\frac{1}{2 I_z \sigma} \left[\frac{1}{\sqrt{\lambda_y}} + \frac{1}{\sqrt{\lambda_x}} \right] \sqrt{\frac{T_x^2}{\lambda_y} + \frac{T_y^2}{\lambda_x}} e^{i \tan^{-1} \left[\frac{T_y \sqrt{\lambda_y}}{T_x \sqrt{\lambda_x}} \right]} \right. \\ C_7 &= \left\{ -\frac{1}{2 I_z \sigma} \left[\frac{1}{\sqrt{\lambda_y}} - \frac{1}{\sqrt{\lambda_x}} \right] \sqrt{\frac{T_x^2}{\lambda_y} + \frac{T_y^2}{\lambda_x}} e^{-i \tan^{-1} \left[\frac{T_y \sqrt{\lambda_y}}{T_x \sqrt{\lambda_x}} \right]} \right. \\ C_8 &= \left\{ \frac{1}{\sigma} \sqrt{\left(\frac{T_x}{\lambda_y I_y}\right)^2 + \left(\frac{T_y}{\lambda_x I_x}\right)^2} e^{i \tan^{-1} \left[\frac{T_y \lambda_y I_y}{T_x \lambda_x I_x} \right]} \right. \end{aligned} \right\} \quad (72)$$

and

The trace of the total rate vector due only to the step torques is shown in figure 7.

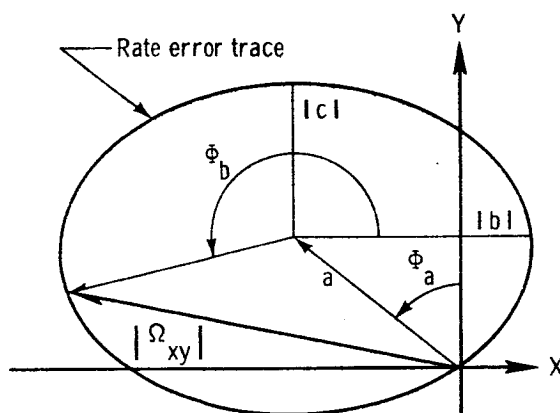


Figure 7.- Rate error trace for step torques.

This trace is now an offset ellipse which intersects the origin at time zero.

The elements of the rate ellipse can be determined from (69) and (70). The center of the ellipse is located by the radius

$$a = \sqrt{\left(\frac{T_x}{\lambda_y I_y}\right)^2 + \left(\frac{T_y}{\lambda_x I_x}\right)^2} \quad (73)$$

and the angular coordinate

$$\phi_a = \tan^{-1} \left(\frac{T_y \lambda_y I_y}{T_x \lambda_x I_x} \right) \quad (74)$$

The semiaxes of the ellipse are found from

$$\left. \begin{aligned} b &= \frac{1}{I_x \sqrt{\lambda_x}} \sqrt{\frac{T_x^2}{\lambda_y} + \frac{T_y^2}{\lambda_x}} \\ c &= \frac{1}{I_y \sqrt{\lambda_y}} \sqrt{\frac{T_x^2}{\lambda_y} + \frac{T_y^2}{\lambda_x}} \end{aligned} \right\} \quad (75)$$

and the angular location of the rate error vector is

$$\phi_b = \tan^{-1} \left\{ \frac{c}{b} \tan \left[\lambda t - \tan^{-1} \left(\frac{T_x \sqrt{\lambda_x}}{T_y \sqrt{\lambda_y}} \right) \right] \right\} \quad (76)$$

The position of the major semiaxis of the ellipse is again dependent on the relative magnitudes of I_x and I_y . If $I_y > I_x$, the maximum semiaxis is parallel to the Y axis; if $I_y < I_x$, the maximum semiaxis is parallel to the X axis. The motion of the Ω_{xy} vector is in the direction of λ and has a period of $\left| \frac{2\pi}{\lambda} \right|$.

An extension of Poincot's development (ref. 12) to the motion of a rigid body under step torques appears possible. The fixed reference point, with respect to which the polhode projection is generated, lies along the maximum angular momentum vector possible for the body. The angular accelerations vanish for steady spin about this axis of maximum angular momentum. By referring to (2) and (3), one notes that the associated coordinates for the fixed point are proportional to

and

$$\left. \begin{aligned} \Omega_{x0} &= -\frac{T_y}{\lambda_x I_x} \\ \Omega_{y0} &= \frac{T_x}{\lambda_y I_y} \end{aligned} \right\} \quad (77)$$

for the constant step torques.

The shape of the polhode projection corresponding to this fixed point is defined by (59). Substitution of (77) into (59) yields the curve

$$\lambda_x (I_x \Omega_x)^2 + \lambda_y (I_y \Omega_y)^2 = \frac{T_x^2}{\lambda_x} + \frac{T_y^2}{\lambda_y} \quad (78)$$

An inspection of figure 7 shows that the polhode projection is indeed represented by the rate vector trace. The fixed point coincides with the center of the trace ellipse and the equation of the ellipse becomes (78).

The inertial attitude error corresponding to the step torques yields the trace shown in figure 8.

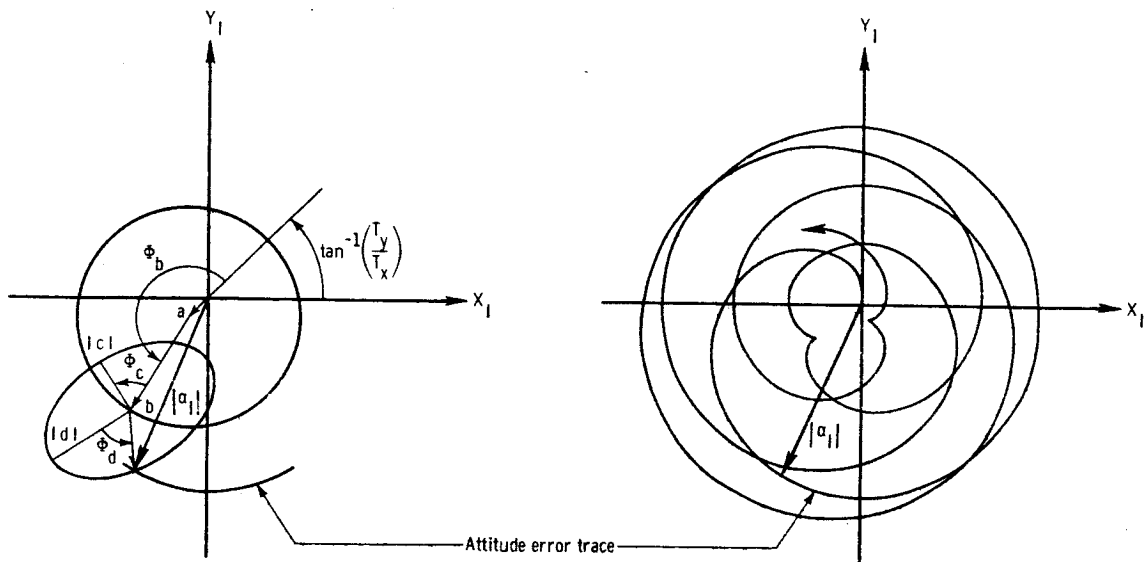


Figure 8.- Attitude error trace for step torques.

This trace results from a point moving along an ellipse, which remains fixed with respect to the rotating radius of a stationary displaced circle. The motion begins at the origin at time zero.

The center of the stationary circle is located by the radial coordinate

$$a = \frac{1}{\sigma^2 I_z} \sqrt{T_x^2 + T_y^2} \quad (79)$$

corresponding to the ratio of the torque to the spin vis viva. The radius of the stationary circle is

$$b = \frac{1}{\sigma} \sqrt{\left(\frac{T_x}{\lambda_y I_y}\right)^2 + \left(\frac{T_y}{\lambda_x I_x}\right)^2} \quad (80)$$

and the center of the moving ellipse has the angular position

$$\phi_b = \sigma t + \tan^{-1} \left(\frac{T_y I_y \lambda_y}{T_x I_x \lambda_x} \right) - \tan^{-1} \left(\frac{T_y}{T_x} \right) \quad (81)$$

The semiaxes of the ellipse are computed from the parameters

$$\left. \begin{aligned} c &= \frac{1}{\sigma I_z \sqrt{\lambda_y}} \sqrt{\frac{T_x^2}{\lambda_y} + \frac{T_y^2}{\lambda_x}} \\ d &= \frac{1}{\sigma I_z \sqrt{\lambda_x}} \sqrt{\frac{T_x^2}{\lambda_y} + \frac{T_y^2}{\lambda_x}} \end{aligned} \right\} \quad (82)$$

and the semiaxis $|c|$ makes the angle

$$\phi_c = \frac{\pi}{2} - \tan^{-1} \left(\frac{T_y I_y \lambda_y}{T_x I_x \lambda_x} \right) \quad (83)$$

with the radius b of the stationary circle. The angular coordinate of the tip of the attitude error vector within the ellipse

$$\Phi_d = \tan^{-1} \left\{ \sqrt{\frac{\lambda_y}{\lambda_x}} \tan \left[\lambda t + \tan^{-1} \left(\frac{T_y \sqrt{\lambda_y}}{T_x \sqrt{\lambda_x}} \right) \right] \right\} \quad (84)$$

completes the development of a point on the error trace curve.

The motion is a closed curve when λ and σ are both rational. The corresponding period is given by $2k\pi$, where k is the least common denominator of σ and λ .

The general properties of the motion can be readily interpreted from figure 8, if one recalls that this figure represents the projection of the Z axis trace onto a plane normal to the Z_I axis. The fixed space axis corresponding to the axis of maximum angular momentum projects as the center of the stationary circle. The motion of the body is bounded by two circles, concentric with the stationary circle and tangent to the moving ellipse in the figure. The outer circle represents the maximum Z axis excursion relative to the fixed momentum vector and can only be approached from the inside. The inner circle represents the minimum Z axis excursion and is approached from the outside when the ellipse does not contain the fixed momentum reference point. When the ellipse contains the momentum reference point, then the inner circle is crossed by the Z axis trace and is approached from the inside.

Upper bounds of the error magnitudes are found from (45) and (46), with the result

$$|\Omega_{xy}|_{\text{lim}} = \sqrt{\left(\frac{T_x}{\lambda_y I_y}\right)^2 + \left(\frac{T_y}{\lambda_x I_x}\right)^2} + \frac{1}{2} \left[\left| \frac{1}{I_x \sqrt{\lambda_x}} + \frac{1}{I_y \sqrt{\lambda_y}} \right| + \left| \frac{1}{I_x \sqrt{\lambda_x}} - \frac{1}{I_y \sqrt{\lambda_y}} \right| \right] \sqrt{\frac{T_x^2}{\lambda_y} + \frac{T_y^2}{\lambda_x}} \quad (85)$$

and

$$|\alpha|_{\text{lim}} = \frac{1}{\sigma^2 I_z} \sqrt{T_x^2 + T_y^2} + \frac{1}{\sigma} \sqrt{\left(\frac{T_x}{\lambda_y I_y}\right)^2 + \left(\frac{T_y}{\lambda_x I_x}\right)^2} + \frac{1}{2\sigma I_z} \left[\left| \frac{1}{\sqrt{\lambda_y}} + \frac{1}{\sqrt{\lambda_x}} \right| + \left| \frac{1}{\sqrt{\lambda_y}} - \frac{1}{\sqrt{\lambda_x}} \right| \right] \sqrt{\frac{T_x^2}{\lambda_y} + \frac{T_y^2}{\lambda_x}} \quad (86)$$

These upper bounds consist of the sums of the radial vector magnitudes and the semimajor axis of the error ellipse, and will obviously be greater than or equal to the maximum error values.

For cylindrical spacecraft spinning about an axis normal to the cylinder axis, large rate and attitude errors will be produced by torques applied about the cylinder axis. Conversely, torques applied about the normal inertia axis in the spin plane will have little effect on the spacecraft motion.

Near-cylindrical spacecraft spinning about a minimum inertia axis, so that I_z is much less than I_x (or I_y), will now be stable if the applied torques do not approach the spin vis viva term $I_z \sigma^2$.

3. Step Products of Inertia

a. Time Histories

Crew or cargo movements within the spacecraft may be represented by equivalent masses m_j with variable position coordinates x_j , y_j ,

and z_j . The movements of the equivalent masses fall into two categories. The first of these includes arbitrary nonperiodic motions along linear paths to some final position. From previous results for symmetrical spacecraft, it appears that the largest rate and attitude errors for such a motion are less than or equal to those for instantaneous motion to the final position. The introduction of step products of inertia corresponding to the final position coordinates of the moving masses gives a limiting case for this type of motion.

The coordinates of the j th mass may thus be written as

$$\left. \begin{aligned} x_j &= x_{j0} \\ y_j &= y_{j0} \\ z_j &= z_{j0}U(t) \end{aligned} \right\} \quad (87)$$

and the corresponding forcing function is

$$\begin{aligned} F = & -\frac{1}{I_x} \left\{ I_{yz} \left[\ddot{\delta}(t) + \sigma^2 \delta(t) \right] + \lambda_y I_{xz} \left[\dot{\delta}(t) + \sigma^2 U(t) \right] \right\} \\ & + \frac{i}{I_y} \left\{ I_{xz} \left[\ddot{\delta}(t) + \sigma^2 \delta(t) \right] - \lambda_x I_{yz} \left[\dot{\delta}(t) + \sigma^2 U(t) \right] \right\} \end{aligned} \quad (88)$$

where the products of inertia now take on the constant values

$$\left. \begin{aligned} I_{xz} &= \sum_{j=1}^n m_j x_{j0} z_{j0} - m_s x_{s0} z_{s0} \\ I_{yz} &= \sum_{j=1}^n m_j y_{j0} z_{j0} - m_s y_{s0} z_{s0} \end{aligned} \right\} \quad (89)$$

The solution for the rate error becomes

$$\begin{aligned} \Omega_{xy} = \tilde{\Omega}_{xy} + (\sigma^2 - \lambda^2) & \left\{ \frac{1}{I_x \sqrt{\lambda_x}} \left[\frac{I_{xz}}{\sqrt{\lambda_x}} \left(\cos \lambda t - \frac{\sigma^2}{\sigma^2 - \lambda^2} \right) - \frac{I_{yz}}{\sqrt{\lambda_y}} \sin \lambda t \right] \right. \\ & \left. + \frac{1}{I_y \sqrt{\lambda_y}} \left[\frac{I_{yz}}{\sqrt{\lambda_y}} \left(\cos \lambda t - \frac{\sigma^2}{\sigma^2 - \lambda^2} \right) + \frac{I_{xz}}{\sqrt{\lambda_x}} \sin \lambda t \right] \right\} - \left(\frac{I_{yz}}{I_x} - \frac{i I_{xz}}{I_y} \right) \delta(t) \end{aligned} \quad (90)$$

and the attitude relation yields

$$\begin{aligned} \alpha = \tilde{\alpha} + & \left\{ \left[\left(\frac{\sigma}{I_y \sqrt{\lambda_y}} - \frac{\lambda}{I_x \sqrt{\lambda_x}} \right) \left(\frac{I_{yz}}{\sqrt{\lambda_y}} \cos \lambda t + \frac{I_{xz}}{\sqrt{\lambda_x}} \sin \lambda t \right) \right] + i \left[\frac{\sigma}{I_x \sqrt{\lambda_x}} \right. \right. \\ & \left. \left. - \frac{\lambda}{I_y \sqrt{\lambda_y}} \left(\frac{I_{yz}}{\sqrt{\lambda_y}} \sin \lambda t - \frac{I_{xz}}{\sqrt{\lambda_x}} \cos \lambda t \right) \right] - \sigma \left[\left(\frac{I_{yz}}{\lambda_y I_y} - \frac{i I_{xz}}{\lambda_x I_x} \right) \right] \right\} \end{aligned} \quad (91)$$

b. Total Errors

The vectorial representation of the total errors reduces to

$$\Omega_{xy} = \tilde{\Omega}_{xy} + B_3 + B_4 e^{i\lambda t} + B_5 e^{-i\lambda t} \quad (92)$$

where

$$\begin{aligned} B_3 = & - \left\{ \sigma^2 \sqrt{\left(\frac{I_{xz}}{\lambda_x I_x} \right)^2 + \left(\frac{I_{yz}}{\lambda_y I_y} \right)^2} \right\} e^{i \tan^{-1} \left[\frac{I_{yz} \lambda_x I_x}{I_{xz} \lambda_y I_y} \right]} \\ & - \left\{ \sqrt{\left(\frac{I_{yz}}{I_x} \right)^2 + \left(\frac{I_{xz}}{I_y} \right)^2} \right\} e^{-i \tan^{-1} \left[\frac{I_{xz} I_x}{I_{yz} I_y} \right]} \delta(t) \end{aligned} \quad (93)$$

$$\left. \begin{aligned} B_4 &= \left\{ \left(\frac{\sigma^2 - \lambda^2}{2} \right) \left(\frac{1}{I_x \sqrt{\lambda_x}} + \frac{1}{I_y \sqrt{\lambda_y}} \right) \sqrt{\left(\frac{I_{xz}}{\sqrt{\lambda_x}} \right)^2 + \left(\frac{I_{yz}}{\sqrt{\lambda_y}} \right)^2} \right\} e^{i \tan^{-1} \left[\frac{I_{yz} \sqrt{\lambda_x}}{I_{xz} \sqrt{\lambda_y}} \right]} \\ B_5 &= \left\{ \left(\frac{\sigma^2 - \lambda^2}{2} \right) \left(\frac{1}{I_x \sqrt{\lambda_x}} - \frac{1}{I_y \sqrt{\lambda_y}} \right) \sqrt{\left(\frac{I_{xz}}{\sqrt{\lambda_x}} \right)^2 + \left(\frac{I_{yz}}{\sqrt{\lambda_y}} \right)^2} \right\} e^{-i \tan^{-1} \left[\frac{I_{yz} \sqrt{\lambda_x}}{I_{xz} \sqrt{\lambda_y}} \right]} \end{aligned} \right\} \quad (93)$$

and

$$\alpha_I = \tilde{\alpha}_I + C_4 e^{i(\sigma+\lambda)t} + C_5 e^{i(\sigma-\lambda)t} + C_6 e^{i\sigma t} \quad (94)$$

where

$$\left. \begin{aligned} C_4 &= \left\{ \left(\frac{\sigma - \lambda}{2} \right) \left(\frac{1}{I_y \sqrt{\lambda_y}} + \frac{1}{I_x \sqrt{\lambda_x}} \right) \sqrt{\left(\frac{I_{yz}}{\sqrt{\lambda_y}} \right)^2 + \left(\frac{I_{xz}}{\sqrt{\lambda_x}} \right)^2} \right\} e^{-i \tan^{-1} \left[\frac{I_{xz} \sqrt{\lambda_y}}{I_{yz} \sqrt{\lambda_x}} \right]} \\ C_5 &= \left\{ \left(\frac{\sigma + \lambda}{2} \right) \left(\frac{1}{I_y \sqrt{\lambda_y}} - \frac{1}{I_x \sqrt{\lambda_x}} \right) \sqrt{\left(\frac{I_{yz}}{\sqrt{\lambda_y}} \right)^2 + \left(\frac{I_{xz}}{\sqrt{\lambda_x}} \right)^2} \right\} e^{i \tan^{-1} \left[\frac{I_{xz} \sqrt{\lambda_y}}{I_{yz} \sqrt{\lambda_x}} \right]} \\ C_6 &= - \left\{ \sigma \sqrt{\left(\frac{I_{yz}}{\lambda_y I_y} \right)^2 + \left(\frac{I_{xz}}{\lambda_x I_x} \right)^2} \right\} e^{-i \tan^{-1} \left[\frac{I_{xz} \lambda_y I_y}{I_{yz} \lambda_x I_x} \right]} \end{aligned} \right\} \quad (95)$$

The trace of the rate error vector is illustrated in figure 9.

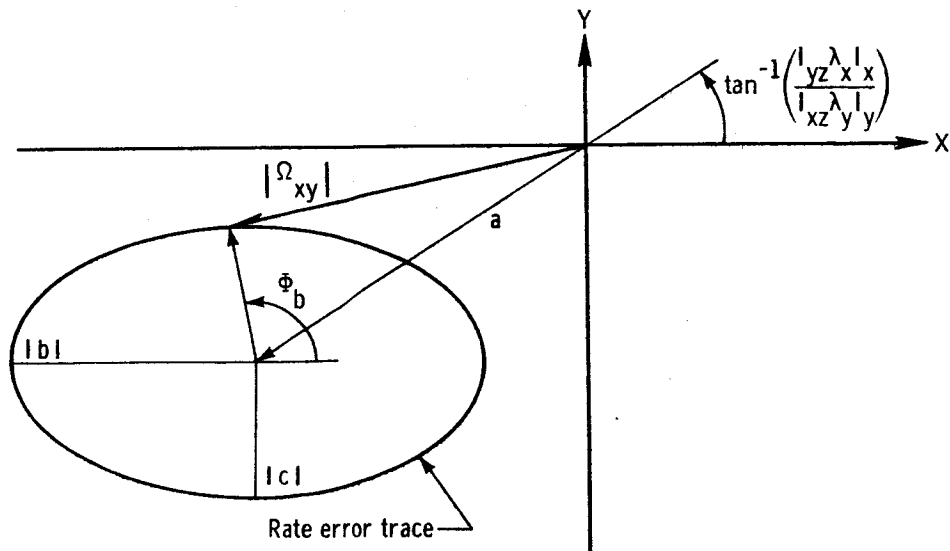


Figure 9.- Rate error trace for step inertia products.

Once more one obtains a displaced ellipse. However, the ellipse now does not intersect the origin.

The radius to the center of this ellipse is

$$a = \sigma^2 \sqrt{\left(\frac{I_{xz}}{\lambda_x I_x}\right)^2 + \left(\frac{I_{yz}}{\lambda_y I_y}\right)^2} \quad (96)$$

and the ellipse characteristics are found from

$$\left. \begin{aligned} b &= \left(\frac{\sigma^2 - \lambda^2}{I_x \sqrt{\lambda_x}}\right) \sqrt{\left(\frac{I_{xz}}{\sqrt{\lambda_x}}\right)^2 + \left(\frac{I_{yz}}{\sqrt{\lambda_y}}\right)^2} \\ c &= \left(\frac{\sigma^2 - \lambda^2}{I_y \sqrt{\lambda_y}}\right) \sqrt{\left(\frac{I_{xz}}{\sqrt{\lambda_x}}\right)^2 + \left(\frac{I_{yz}}{\sqrt{\lambda_y}}\right)^2} \end{aligned} \right\} \quad (97)$$

and

$$\phi_b = \tan^{-1} \left\{ \frac{c}{b} \tan \left[\lambda t + \tan^{-1} \left(\frac{I_{yz} \sqrt{\lambda_x}}{I_{xz} \sqrt{\lambda_y}} \right) \right] \right\} \quad (98)$$

The major semiaxis of the trace ellipse is parallel to the X axis when $I_x > I_y$ and is parallel to the Y axis when $I_y > I_x$. However, the body axis with the largest rate error is determined primarily by the location of the center of the trace ellipse. The period of the counterclockwise motion is again the precession period $\left| \frac{2\pi}{\lambda} \right|$, and the direction of motion is in the direction of the precession rate λ .

To correlate figure 9 with Poincot's development, note that the coordinates of the fixed reference point for the polhode are proportional to

$$\left. \begin{aligned} \Omega_{x0}' &= - \frac{\sigma^2 I_{xz}}{\lambda_x I_x} \\ \Omega_{y0}' &= - \frac{\sigma^2 I_{yz}}{\lambda_y I_y} \end{aligned} \right\} \quad (99)$$

and

from (2) and (3). This shift of the reference point from the coordinate origin to the principal body axis indicates that the maximum possible angular momentum vector lies along the new extreme inertia axis. Steady spin, for which the polhode reduces to a point, is thus possible only about the new maximum or minimum principal axis of inertia. In figure 9, this principal axis passes through the center of the rate ellipse, as specified by (96).

The interpretation of the polhode projection about the fixed reference point becomes somewhat more difficult. Two terms now contribute to the polhode, namely the rotation of the extreme principal axis and the effective acceleration torque produced by introduction of the step product of inertia. The rotation of the extreme principal axis yields the initial rates given in (99). The step introduction of the product of inertia yields the additional rate terms

$$\left. \begin{aligned} \Omega_{x0}'' &= \frac{\lambda_y I_{xz}}{I_x} \\ \Omega_{y0}'' &= \frac{\lambda_x I_{yz}}{I_y} \end{aligned} \right\} \quad (100)$$

and

The polhode projection (59) corresponds to the rate vector trace in figure 9, if the reference body rates Ω_{x0} and Ω_{y0} include both (99) and (100).

The angular position trace for the step products of inertia is presented in figure 10.

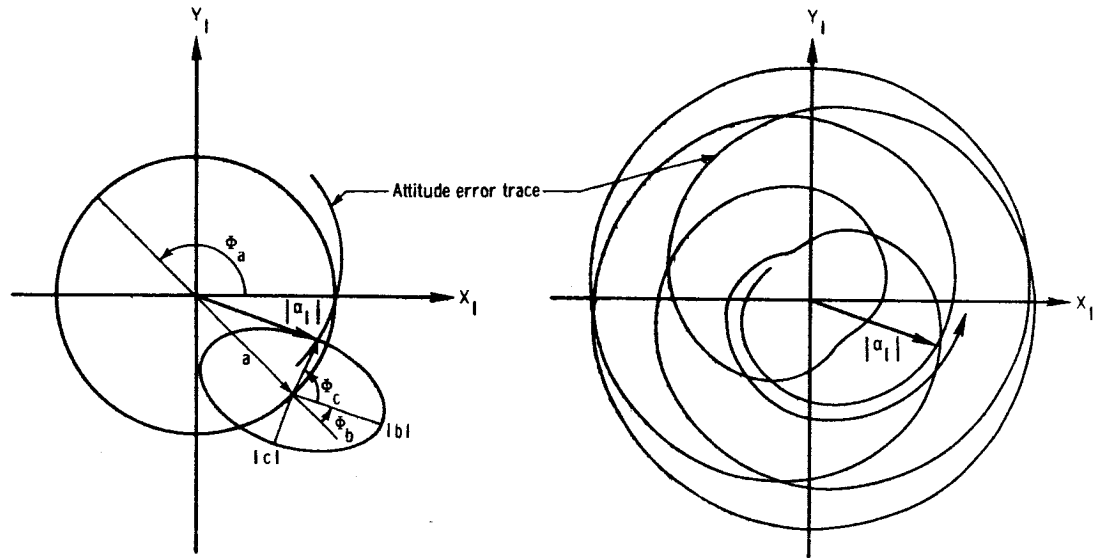


Figure 10.- Attitude error trace for step inertia products.

The trace is produced by a point on an ellipse, which remains fixed with respect to the rotating radius of a stationary circle centered at the origin of the inertial axis system.

The radius of the stationary circle is

$$a = \sigma \sqrt{\left(\frac{I_{yz}}{\lambda_y I_y}\right)^2 + \left(\frac{I_{xz}}{\lambda_x I_x}\right)^2} \quad (101)$$

and the ellipse center is defined by the angle

$$\phi_a = \sigma t - \tan^{-1} \left(\frac{I_{xz} \lambda_y I_y}{I_{yz} \lambda_x I_x} \right) \quad (102)$$

The ellipse semiaxes are found from

$$\left. \begin{aligned} b &= \left(\frac{\sigma}{I_y \sqrt{\lambda_y}} - \frac{\lambda}{I_x \sqrt{\lambda_x}} \right) \sqrt{\left(\frac{I_{yz}}{\sqrt{\lambda_y}} \right)^2 + \left(\frac{I_{xz}}{\sqrt{\lambda_x}} \right)^2} \\ c &= \left(\frac{\sigma}{I_x \sqrt{\lambda_x}} - \frac{\lambda}{I_y \sqrt{\lambda_y}} \right) \sqrt{\left(\frac{I_{yz}}{\sqrt{\lambda_y}} \right)^2 + \left(\frac{I_{xz}}{\sqrt{\lambda_x}} \right)^2} \end{aligned} \right\} \quad (103)$$

and the angle between the stationary circle radius a and the ellipse semiaxis $|b|$ becomes

$$\Phi_b = \tan^{-1} \left(\frac{I_{xz} \lambda_y I_y}{I_{yz} \lambda_x I_x} \right) \quad (104)$$

The position angle of the attitude error vector tip is now

$$\Phi_c = \tan^{-1} \left\{ \frac{c}{b} \tan \left[\lambda t - \tan^{-1} \left(\frac{I_{xz} \sqrt{\lambda_y}}{I_{yz} \sqrt{\lambda_x}} \right) \right] \right\} \quad (105)$$

with respect to the ellipse semiaxis $|b|$.

The period of the precessional motion is $2k\pi$, with k taken as the least common denominator of σ and λ for rational σ and λ .

The general properties of motion for the step inertia product are similar to those for the step torques. However, the fixed space axis corresponding to the maximum angular momentum vector projects as the origin of the $X_I Y_I$ plane, and the direction of the total angular momentum vector for the spacecraft is not changed in inertial space during the step crew motion. The spacecraft motion is bounded by two circles, drawn with center at the origin and tangent to the moving

ellipse. The nature of these boundaries has been discussed in the step torque analysis.

Upper bounds of the errors are

$$|\Omega_{xy}|_{\lim} = \sigma^2 \sqrt{\left(\frac{I_{xz}}{\lambda_x I_x}\right)^2 + \left(\frac{I_{yz}}{\lambda_y I_y}\right)^2} + \left(\frac{\sigma^2 - \lambda^2}{2}\right) \left[\left| \frac{1}{I_x \sqrt{\lambda_x}} \right. \right. \\ \left. \left. + \frac{1}{I_y \sqrt{\lambda_y}} \right| + \left| \frac{1}{I_x \sqrt{\lambda_x}} - \frac{1}{I_y \sqrt{\lambda_y}} \right| \right] \sqrt{\left(\frac{I_{xz}}{\sqrt{\lambda_x}}\right)^2 + \left(\frac{I_{yz}}{\sqrt{\lambda_y}}\right)^2} \quad (106)$$

for the rate vector and

$$|\alpha|_{\lim} = \sigma \sqrt{\left(\frac{I_{yz}}{\lambda_y I_y}\right)^2 + \left(\frac{I_{xz}}{\lambda_x I_x}\right)^2} + \left[\left| \left(\frac{\sigma - \lambda}{2}\right) \left(\frac{1}{I_y \sqrt{\lambda_y}} + \frac{1}{I_x \sqrt{\lambda_x}}\right) \right| \right. \\ \left. + \left| \left(\frac{\sigma + \lambda}{2}\right) \left(\frac{1}{I_y \sqrt{\lambda_y}} - \frac{1}{I_x \sqrt{\lambda_x}}\right) \right| \right] \sqrt{\left(\frac{I_{xz}}{\sqrt{\lambda_x}}\right)^2 + \left(\frac{I_{yz}}{\sqrt{\lambda_y}}\right)^2} \quad (107)$$

for the attitude error vector.

As before, cylindrical spacecraft spinning about a normal axis lead to large errors for small products of inertia in the plane corresponding to the two large inertias. Some differences in the response for the step inertia products and that for step torques can, however, arise after the removal of the disturbance. For the step torques this removal can occur when the rate error vector passes through the origin of the body axis system, so that the only residual error is a constant attitude error corresponding to the attitude at the time of disturbance

removal. This fact may be of use in the design of pure attitude control system for spacecraft which use constant torque pulses to reorient the spacecraft.

For step products of inertia, removal of the disturbance could also null the rate errors if done when the rate error vector passes through its initial position. In practice, the determination of this position does not appear feasible without very exact values for the spacecraft and disturbance characteristics. The elimination of the body rate errors by the timely removal of the product of inertia is a very complex task, and in general will lead to both residual rate and attitude errors.

4. Variable Products of Inertia

A second category of mass movements within the spacecraft involves periodic motions, such as mass transfer along a circumferential path. The uncontrolled motion of the spacecraft is now similar to that of a spring-mass system with a periodic forcing function. The amplitudes of the rate and attitude error are correspondingly multiplied by a magnification factor and resonance may occur for particular mass transfer rates. The determination of the effects of periodic mass motions within the spacecraft is thus an essential prerequisite to the analysis and selection of the spacecraft control system.

There are, unfortunately, an infinite number of possible periodic crew motions. The best approach to a study of these motions may be the formulation of a general forcing function, which permits the development

of stability criteria and rate and attitude errors for a number of representative periodic motions. Particular time histories can then be developed for special cases of the general forcing function.

To arrive at such a general forcing function, assume that the periodic mass motions involve transfer of a single mass and take place in a spin plane perpendicular to the Z axis or along a line parallel to the Z axis. If one adopts a sinusoidal variation of the associated mass position coordinates, the complex forcing function takes the form

$$F = E_0 \cos pt + E_1 \sin pt + E_2 \delta(t) + E_3 \dot{\delta}(t) + E_4 \ddot{\delta}(t) \quad (108)$$

The coefficients E_j are complex constants which must be determined for particular mass motions, and p is the period of the motions.

A number of characteristic motions included in equation (108) are listed in table 4 along with the corresponding coefficients E_j . As seen from the table, the forcing function equation (108) comprises linear periodic motions parallel to each spacecraft axis in the spacecraft reference planes XZ and YZ and circumferential motion in a plane perpendicular to the spacecraft Z axis. Other mass motions can be constructed by combining the forcing functions in the table and by adding the forcing function equation (88) for the static products of inertia with appropriate values of I_{xz} and I_{yz} to the result. Any linear oscillation in a spin plane perpendicular to the Z axis or along a line parallel to the Z axis can be developed by this method.

Only the motions described in table 4 will be considered as examples for the present analysis; the results obtained for these motions can be

readily applied to more complex motions obtained by linear combinations of the forcing functions given by the table.

a. Stability Trends

An assessment of the stability trends for the variable products of inertia can be obtained by examining the forcing function terms in equation (108) together with the solution functions of tables 1 and 3. The uncontrolled spacecraft motion will be unstable when the roots of the governing equations (29) and (34) contain real, positive, nonzero terms or when the forcing functions produce resonance conditions. From table 1, it is apparent that the solution functions for $\delta(t)$, $\dot{\delta}(t)$, and $\ddot{\delta}(t)$ contain only constant and periodic terms. These terms thus cannot cause divergence of the rate and attitude errors.

The solution functions for $\cos pt$ and $\sin pt$ can, however, contain divergent terms and may lead to continuously increasing errors for special frequencies of the periodic motions. These special frequencies are $|p| = |\sigma|$ and $|p| = |\lambda|$. In the first case, the rate errors remain bounded for all finite values of E_0 and E_1 , but precession of the spacecraft may result unless

$$\left. \begin{array}{l} E_0 + iE_1 = 0 \\ E_0 - iE_1 = 0 \end{array} \right\} \quad \text{when } p = \sigma \text{ and} \quad (109)$$

when $p = -\sigma$. Since equation (109) holds for all the values of E_0 and E_1 in table 4, this precession will not occur for the examples considered here.

In the second case, when $|p| = |\lambda|$, both the rate and attitude errors will tend to diverge for nonzero values of E_0 and E_1 . Mass motions with this period thus exhibit definite trends toward instability and should be avoided.

There is, of course, one other instability that may occur for the present solution. From the governing equation (29) for the body rates, one notes that the rate error will diverge when $\lambda^2 < 0$, so that $I_x > I_z > I_y$ or $I_y > I_z > I_x$. This condition results when the Z axis is an intermediate axis of inertia and agrees with the well-known fact that the undamped spacecraft spin is stable only if the spin axis is an axis of maximum or minimum inertia. In terms of the moving mass parameters, one may thus write

$$\left. \begin{aligned} \left[\sum_{j=1}^n m_j (y_{jo}^2 - z_{jo}^2) - m_s (y_{so}^2 - z_{so}^2) \right] &< (I_{y0} - I_{z0}) \\ \left[\sum_{j=1}^n m_j (x_{jo}^2 - z_{jo}^2) - m_s (x_{so}^2 - z_{so}^2) \right] &> (I_{x0} - I_{z0}) \end{aligned} \right\} \quad (110)$$

or

$$\left. \begin{aligned} \left[\sum_{j=1}^n m_j (y_{jo}^2 - z_{jo}^2) - m_s (y_{so}^2 - z_{so}^2) \right] &> (I_{y0} - I_{z0}) \\ \left[\sum_{j=1}^n m_j (x_{jo}^2 - z_{jo}^2) - m_s (x_{so}^2 - z_{so}^2) \right] &< (I_{x0} - I_{z0}) \end{aligned} \right\} \quad (111)$$

as the alternative conditions for instability corresponding to the assumptions of this analysis.

The conditions in this section will serve to indicate possible instabilities for the rotating spacecraft. Since the rate and attitude errors for these instabilities will rapidly exceed the small angle and rate assumptions, time histories for these motions will not be discussed. If the unstable motions do occur, exact computer solutions should be used to assess their effects.

b. Time Histories

From equation (108) and the solution functions of tables 1 and 3, the rate error becomes

$$\begin{aligned} \Omega_{xy} = \tilde{\Omega}_{xy} + \left(\frac{E_0}{\lambda^2 - p^2} \right) \cos pt + \left(\frac{E_1}{\lambda^2 - p^2} \right) \sin pt \\ + E_4 \delta(t) + E_5 \cos \lambda t + E_6 \sin \lambda t \end{aligned} \quad (112)$$

where

$$\left. \begin{aligned} E_5 &= E_3 - \left(\frac{E_0}{\lambda^2 - p^2} \right) \\ E_6 &= \frac{1}{\lambda} \left[(E_2 - \lambda^2 E_4) - p \left(\frac{E_1}{\lambda^2 - p^2} \right) \right] \end{aligned} \right\} \quad (113)$$

while the attitude error is

$$\begin{aligned} \alpha = \tilde{\alpha} + \left(\frac{1}{\sigma^2 - p^2} \right) \left[\left(\frac{pE_1 - i\sigma E_0}{\lambda^2 - p^2} \right) \cos pt - \left(\frac{pE_0 + i\sigma E_1}{\lambda^2 - p^2} \right) \sin pt \right] \\ + \left(\frac{1}{\sigma^2 - \lambda^2} \right) \left[(\lambda E_6 - i\sigma E_5) \cos \lambda t - (\lambda E_5 + i\sigma E_6) \sin \lambda t \right] \\ + E_7 (\cos \sigma t - i \sin \sigma t) \end{aligned} \quad (114)$$

where

$$E_7 = E_4 - \left[\frac{\lambda E_6 - i\sigma E_5}{\sigma^2 - \lambda^2} + \frac{pE_1 - i\sigma E_0}{(\sigma^2 - p^2)(\lambda^2 - p^2)} \right] \quad (115)$$

c. Total Errors

The vectorial representation of these errors yields

$$\Omega_{xy} = \tilde{\Omega}_{xy} + B_3 + B_4 e^{i\lambda t} + B_5 e^{-i\lambda t} + B_6 e^{ipt} + B_7 e^{-ipt} \quad (116)$$

with

$$\left. \begin{aligned} B_3 &= E_4 \delta(t) \\ B_4 &= \frac{1}{2} (E_5 - iE_6) \\ B_5 &= \frac{1}{2} (E_5 + iE_6) \\ B_6 &= \frac{1}{2} \left(\frac{E_0 - iE_1}{\lambda^2 - p^2} \right) \\ B_7 &= \frac{1}{2} \left(\frac{E_0 + iE_1}{\lambda^2 - p^2} \right) \end{aligned} \right\} \quad (117)$$

and, from (18)

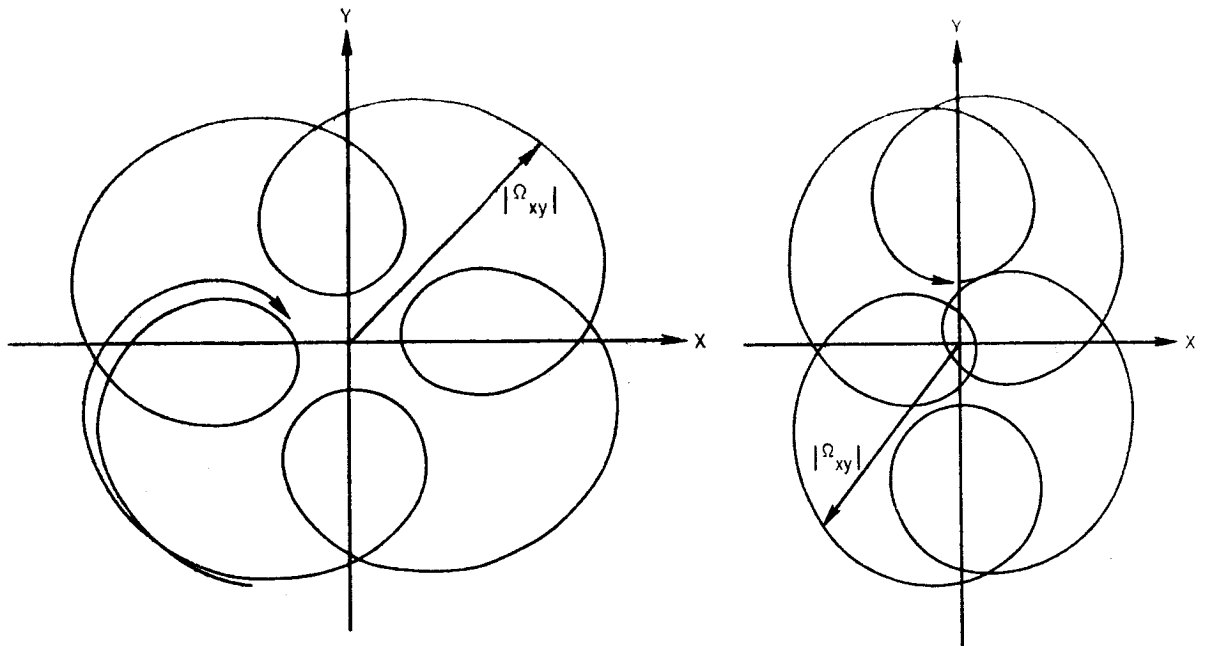
$$\alpha_I = \tilde{\alpha}_I + i \left[C_4 + C_5 e^{i(\sigma+\lambda)t} + C_6 e^{i(\sigma-\lambda)t} + C_7 e^{i(\sigma+p)t} + C_8 e^{i(\sigma-p)t} \right] \quad (118)$$

where

$$\left. \begin{aligned} C_4 &= 1E_4 + \frac{B_4}{\sigma + \lambda} + \frac{B_5}{\sigma - \lambda} + \frac{B_6}{\sigma + p} + \frac{B_7}{\sigma - p} \\ C_5 &= - \frac{B_4}{\sigma + \lambda} \\ C_6 &= - \frac{B_5}{\sigma - \lambda} \\ C_7 &= - \frac{B_6}{\sigma + p} \\ C_8 &= - \frac{B_7}{\sigma - p} \end{aligned} \right\} \quad (119)$$

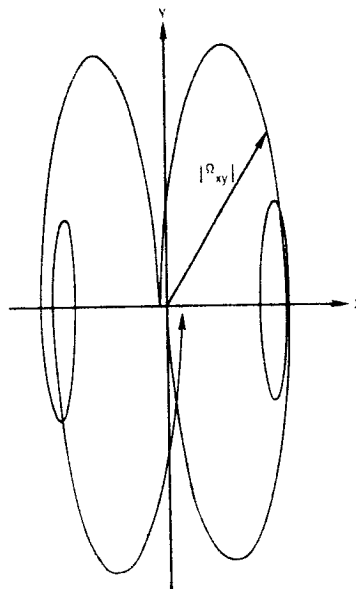
The total error relations given by equations (112)-(119) may now be evaluated for particular motions by substitution of the corresponding coefficients E_0 , E_1 , E_2 , E_3 , and E_4 from table 4. Only the vectorial representations and the upper bounds of the errors will usually have to be considered in an assessment of the effects of mass motion on the spacecraft motion.

To determine the vectorial traces one needs values for E_4 , B_4 , B_5 , B_6 , and B_7 . These expressions have been developed and are shown in tables 4 and 5 for the motions described in table 4. The polar plots of the rate errors now follow directly from equation (116) and are graphed in figure 11 for a number of typical motions.



(a) Circumferential mass motion.

(b) X-axis mass oscillation in XZ plane.



(c) Z-axis mass oscillation in XZ plane.

Figure 11.- Rate error traces for periodic inertia products.

All of these traces are generated by a point on an ellipse, whose center moves along a second ellipse centered at the origin of the body axis system. Figure 12 shows this development of the rate vector trace.

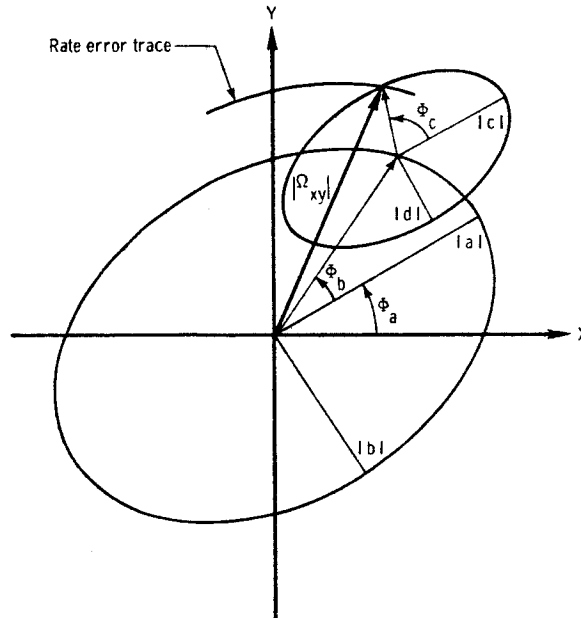


Figure 12.- Rate error trace development for periodic inertia products.

The direction of the ellipse semiaxes $|a|$ and $|c|$ is first located by the relation

$$\left. \begin{aligned} \phi_a &= 0 & a^2 &> 0 \\ \phi_a &= \frac{\pi}{2} & a^2 &< 0 \end{aligned} \right\} \quad (120)$$

The position angles for the fixed and moving ellipses then become

$$\left. \begin{aligned} \phi_b &= \tan^{-1} \left[\frac{b}{a} \tan pt \right] \\ \phi_c &= \tan^{-1} \left[\frac{d}{c} \tan \lambda t \right] \end{aligned} \right\} \quad (121)$$

and

The fixed ellipse has semiaxes $|a|$ and $|b|$, and the moving ellipse has semiaxes $|c|$ and $|d|$. The constants a , b , c , and d are determined from (116) and (117) as

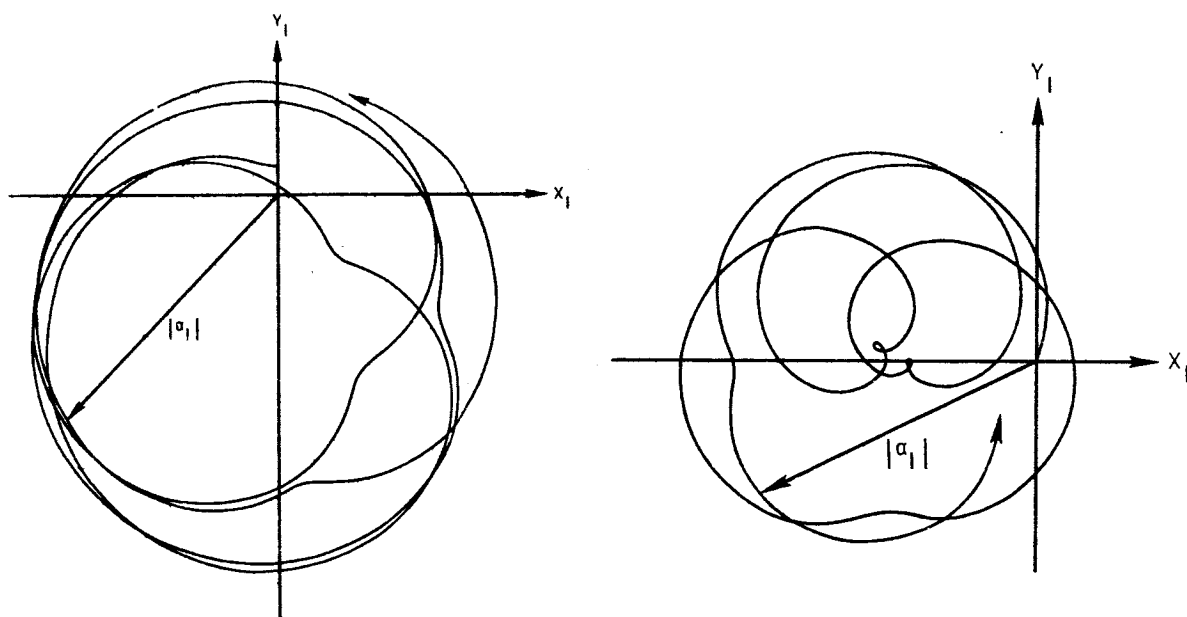
$$\left. \begin{aligned} a &= B_6 + B_7 \\ b &= B_6 - B_7 \\ c &= B_4 + B_5 \\ d &= B_4 - B_5 \end{aligned} \right\} \quad (122)$$

where the values of the B_j terms are taken from table 5.

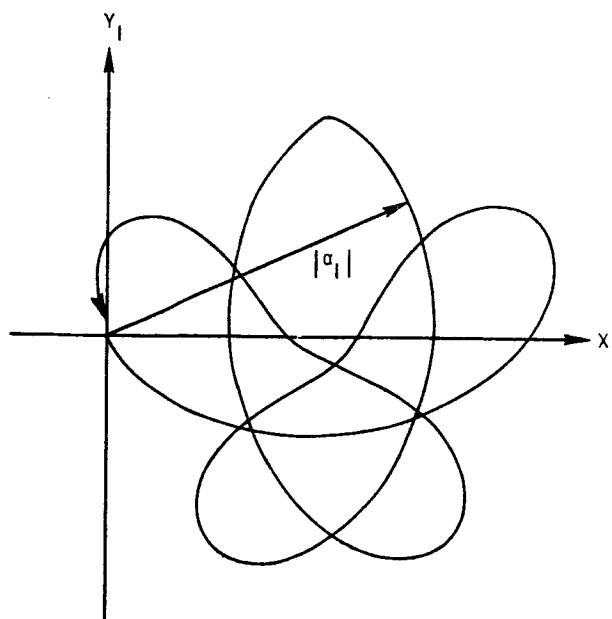
The direction of motion is determined by the signs of p and λ , and the rate vector describes a closed curve when p and λ are both rational. The period of motion is $2k\pi$, where k is the least common denominator of p and λ .

The rate error trace results from the oscillation of the mass with respect to the geometric body axes (p -ellipse), added to the precession of the geometric body axes about the principal body axes (λ -ellipse). The fixed reference point for the trace falls on the origin of the geometric body axis system since the mass oscillation takes place about the origin.

Characteristic traces of the attitude errors for the periodic motions are illustrated in figure 13.



(a) Circumferential mass motion. (b) X-axis mass oscillation in XZ plane.



(c) Z-axis mass oscillation in XZ plane.

Figure 13.- Attitude error traces for periodic inertia products.

These traces are produced by two ellipses which rotate at the spin rate, as sketched in figure 14.

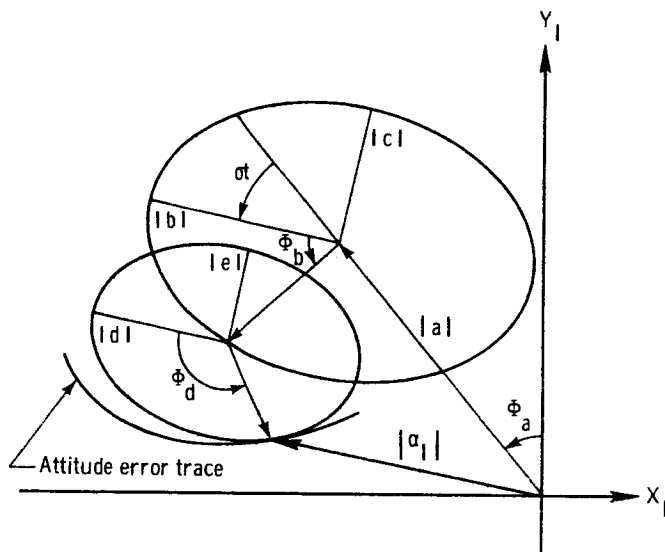


Figure 14.- Attitude error trace development for periodic inertia products.

The center of rotation is defined by the coordinates

$$a = -iE_4 + \frac{B_4}{\sigma + \lambda} + \frac{B_5}{\sigma - \lambda} + \frac{B_6}{\sigma + p} + \frac{B_7}{\sigma - p} \quad (123)$$

and

$$\left. \begin{array}{ll} \Phi_a = 0 & a^2 > 0, \quad a > 0 \\ \Phi_a = \frac{\pi}{2} & a^2 < 0, \quad a > 0 \\ \Phi_a = \pi & a^2 > 0, \quad a < 0 \\ \Phi_a = \frac{3\pi}{2} & a^2 < 0, \quad a < 0 \end{array} \right\} \quad (124)$$

The direction of the ellipse semiaxes $|b|$ and $|d|$ is located by the angle σt , measured from the positive Y_I axis when $\phi_a = 0$ or π and measured from the negative X_I axis when $\phi_a = \frac{\pi}{2}$ or $\frac{3\pi}{2}$. The angular coordinates within the ellipses now become

$$\left. \begin{aligned} \phi_b &= \tan^{-1} \left[\frac{c}{b} \tan pt \right] \\ \text{and} \\ \phi_d &= \tan^{-1} \left[\frac{e}{d} \tan \lambda t \right] \end{aligned} \right\} \quad (125)$$

while the ellipse semimajor axes $|b|$, $|c|$, $|d|$, and $|e|$ are derived from

$$\left. \begin{aligned} b &= - \left(\frac{B_6}{\sigma + p} + \frac{B_7}{\sigma - p} \right) \\ c &= - \left(\frac{B_6}{\sigma + p} - \frac{B_7}{\sigma - p} \right) \\ d &= - \left(\frac{B_4}{\sigma + \lambda} + \frac{B_5}{\sigma - \lambda} \right) \\ \text{and} \\ e &= - \left(\frac{B_4}{\sigma + \lambda} - \frac{B_5}{\sigma - \lambda} \right) \end{aligned} \right\} \quad (126)$$

The motion is a closed curve when σ , p , and λ are all rational. The precession period is $2k\pi$ where k is the least common denominator of σ , p , and λ .

The attitude trace for the spacecraft with periodic inertia products exhibits a change in the direction of the angular momentum vector in inertial space. This rotation of the momentum vector to the

center of the p ellipse results from the initial mass acceleration terms, which exert a torque on the spacecraft. The motion, in body coordinates referred to the fixed momentum reference point, can be visualized as the sum of the mass oscillation with respect to the body axes (p-ellipse) and the precession of the body axes about the principal axes (λ -ellipse). In the intermediate inertial coordinates, this motion is rotated through the angle σt .

Values for the upper bounds of the rate and attitude errors may be calculated from

$$|\Omega_{xy}|_{\text{lim}} = |B_4| + |B_5| + |B_6| + |B_7| \quad (127)$$

and

$$\begin{aligned} |\alpha|_{\text{lim}} = & \left| -iE_4 + \frac{B_4}{\sigma + \lambda} + \frac{B_5}{\sigma - \lambda} + \frac{B_6}{\sigma + p} + \frac{B_7}{\sigma - p} \right| \\ & + \left| \frac{B_4}{\sigma + \lambda} \right| + \left| \frac{B_5}{\sigma - \lambda} \right| + \left| \frac{B_6}{\sigma + p} \right| + \left| \frac{B_7}{\sigma - p} \right| \end{aligned} \quad (128)$$

by using the coefficient equations for E_4 and B_j from tables 4 and 5.

From an examination of these coefficient equations, one notes that the maximum error relations for small disturbance frequencies p yield the error limit terms corresponding to the introduction of step products of inertia. Both principal-axis-rotation and acceleration terms result for the circumferential motions; only principal-axis-rotation terms appear for the radial and vertical oscillations. A first estimate of the limiting errors for the periodic inertia products can

accordingly be obtained from the appropriate step inertia product terms, when the disturbance frequency $|p|$ is much less than the precession frequency $|\lambda|$.

As the disturbance frequency increases, the error limits also increase. As expected, divergence of the errors is predicted when $|p| = |\lambda|$. For a further increase in the disturbance frequencies, the error limits continue to increase.

When the disturbance frequency $|p|$ is much greater than the spin rate σ , the error relations for the periodic inertia products become directly proportional to $|p|$. Doubling of the disturbance frequency will thus double the resultant error limits, and large errors can be introduced by small, rapidly oscillating masses which may occur in onboard motors, generators, or other equipment.

Several additional trends are indicated by tables 4 and 5. For circumferential motion, maximum errors result when the sign of the angular velocity p of the motion coincides with the sign of the precession rate λ . Motion at a negative spin rate ($p = -\sigma$) will eliminate all but the initial acceleration effects. Motion at a negative or positive spin rate ($p = \pm\sigma$) also nulls the errors caused by vertical mass oscillations, but does not significantly affect the errors caused by the radial mass oscillations.

D. Characteristic Disturbances for Symmetric Spacecraft

A large number of spinning spacecraft will be symmetric about their spin axis, so that $I \equiv I_x = I_y$. These spacecraft include rockets and

ballistic missiles which are spin-stabilized to maintain their flight path angle under initial body rates; unmanned satellites which are spin-stabilized to maintain a fixed inertial position for communication and observation purposes; and large manned space stations which provide an artificial gravity field for their crew. A reduction of the general solutions developed in the previous chapter to the special case of symmetric spacecraft would accordingly have many applications.

Most of the resultant solutions have been previously obtained by various approximation and numerical integration techniques and are scattered through the literature (refs. 4-20). The results in this chapter thus make no claim to originality, but do accomplish two important objectives.

The first objective involves the determination of the form of the geometric error traces and of the maximum error limits for the various disturbances. These important properties of the motion have been only partially treated in the literature, and tend to be obscured by the component form in which past solutions are primarily expressed. The simple trace geometry, that results from the complex vector representation of the present analysis should be of considerable value.

The second objective is the comparison of the approximate solution with applicable previous results. This comparison will point out the principal differences between the present and past solutions and will summarize the trends of the motion with variations in the disturbance and spacecraft characteristics.

The discussions of the polhode projections and of the motion representation by means of the unit sphere will not be repeated here. If desired, these relations can be readily deduced from the analysis for the nonsymmetric case and the equations of this chapter.

1. Impulsive Torques

For impulsive torque disturbances of the form

$$M \equiv M_x + iM_y = T\delta(t) \equiv (T_x + iT_y)\delta(t)$$

the forcing function (48) becomes

$$F = \frac{T}{I} [\dot{\delta}(t) + i\lambda\delta(t)] \quad (129)$$

The total rate and attitude error equations (49) and (50) yield

$$\Omega_{xy} = \tilde{\Omega}_{xy} + \frac{T}{I} (\cos \lambda t + i \sin \lambda t) \quad (130)$$

and

$$\alpha = \tilde{\alpha} + \frac{T}{\sigma I_z} [(\sin \lambda t - i \cos \lambda t) + (\sin \sigma t + i \cos \sigma t)] \quad (131)$$

Initial error contributions in (130) and (131) are

$$\tilde{\Omega}_{xy} = \Omega_{xy0} (\cos \lambda t + i \sin \lambda t) \quad (132)$$

and

$$\begin{aligned} \tilde{\alpha} = \alpha_0 (\cos \sigma t - i \sin \sigma t) + i \left(\frac{i\Omega_{xy0}}{\sigma I_z} \right) [(\cos \sigma t - i \sin \sigma t) \\ - (\cos \lambda t + i \sin \lambda t)] \end{aligned} \quad (133)$$

from (40) and (41).

The total error vectors for the impulsive torques reduce to

$$\Omega_{xy} = \tilde{\Omega}_{xy} + \left(\frac{T}{I}\right)e^{i\lambda t} \quad (134)$$

and

$$\alpha_I = \tilde{\alpha}_I + i\left(\frac{T}{\sigma I_z}\right)\left[1 - e^{i(\sigma+\lambda)t}\right] \quad (135)$$

where the initial condition vectors are

$$\tilde{\Omega}_{xy} = \Omega_{xy0}e^{i\lambda t} \quad (136)$$

and

$$\tilde{\alpha}_I = \alpha_0 + i\left(\frac{I\Omega_{xy0}}{\sigma I_z}\right)\left(1 - e^{i(\sigma+\lambda)t}\right) \quad (137)$$

The rate vector trace for symmetrical spacecraft with initial rate and attitude errors is shown in figure 15.

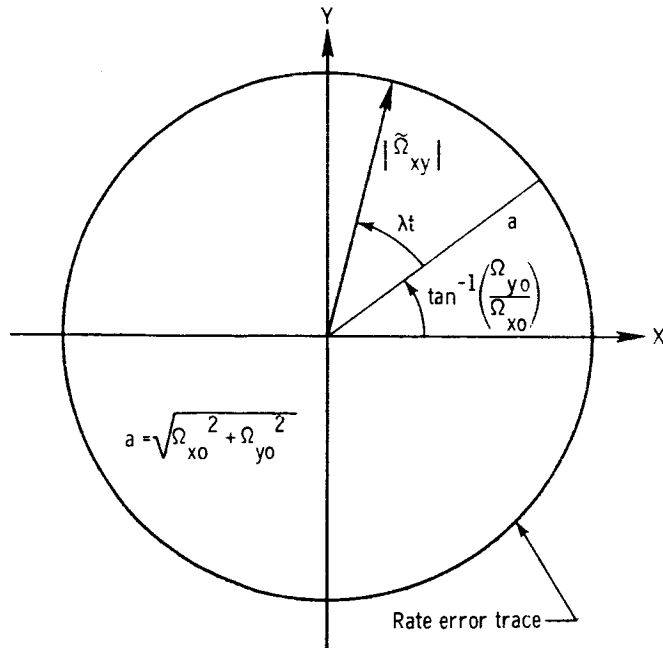


Figure 15.- Rate error trace for initial conditions and symmetric spacecraft.

The curve traced out by the $\tilde{\Omega}_{xy}$ vector is a circle whose radius is the magnitude of the initial rate error vector Ω_{xy0} . The rate vector $\tilde{\Omega}_{xy}$ rotates with the precession rate λ to generate the error envelope.

The attitude error trace, shown in figure 16,

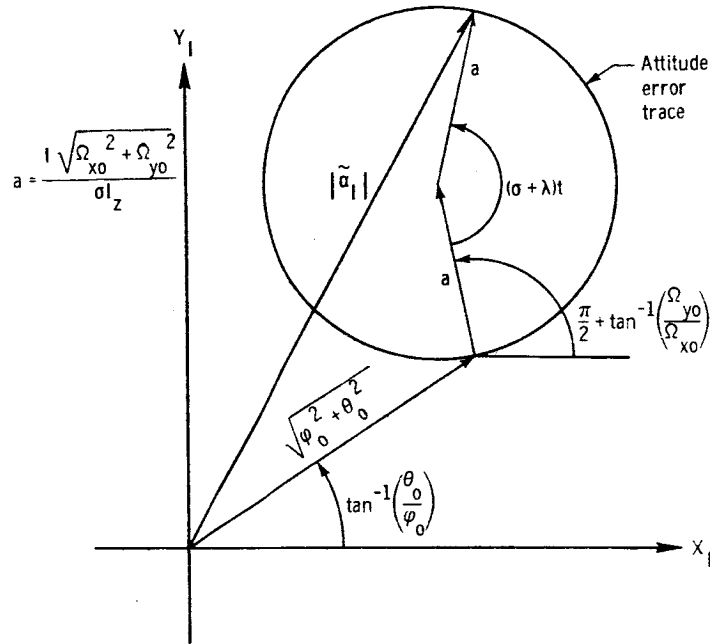


Figure 16.- Attitude error trace for initial conditions and symmetric spacecraft.

is also a circle. The center of this circle is determined by the vector $\alpha_0 + i \frac{I \Omega_{xy0}}{\sigma I_z}$, and the radius of the circle is the ratio of the inplane and spin momentum. The period of motion is $\frac{2\pi}{\sigma + \lambda}$, and the attitude error vector moves in the direction of spin.

Maximum error values can be derived from figures 15 and 16. The result is

$$|\Omega_{xy}|_{\max} = \sqrt{\Omega_{xo}^2 + \Omega_{yo}^2} \quad (138)$$

and

$$|\alpha|_{\max} = \sqrt{(\Phi_0 - \Omega_{yo} + \cos \Phi)^2 + (\theta_0 + \Omega_{xo} + a \sin \Phi)^2} \quad (139)$$

where

$$\left. \begin{aligned} a &= \frac{I \sqrt{\Omega_{xo}^2 + \Omega_{yo}^2}}{\sigma I_z} \\ \Phi &= \tan^{-1} \left(\frac{\theta_0 + \Omega_{xo}}{\Phi_0 - \Omega_{yo}} \right) \end{aligned} \right\} \quad (140)$$

From (139), it can be seen that the spacecraft inertia ratio $\frac{I}{I_z}$ does not affect the maximum rate error. The inertia ratio does, however, enter into the relation for the maximum attitude error which decreases with a decrease in the inertia ratio. Spacecraft, whose inertia ratio approaches that of a flat disk, will thus yield the minimum total attitude error for a given set of initial error values.

The error relations developed here have been partially described by Leon (ref. 5) for the case of a spinning symmetric rocket, and the applicable present results agree with his conclusions. His work does not, however, develop the detailed trace representation or the maximum error relations. Thomson (ref. 6) includes the trace representations for the initial errors, but his geometrical interpretation is incorrect (see page 201). The initial error vector α_0 and the initial body rate Ω_{xy0} are not generally orthogonal, as depicted in Thomson's work.

The error traces and maximum error values for the impulsive torques can be again found by setting $\frac{T_x}{I} = \Omega_{x0}$, $\frac{T_y}{I} = \Omega_{y0}$, and $\phi_0 = \theta_0 = 0$ in equations (136) - (140) and figures 15 and 16.

2. Step Torques

For constant step torques described by

$$M \equiv M_x + iM_y = TU(t) \equiv (T_x + iT_y)U(t)$$

the forcing function (66) yields

$$F = \frac{T}{I} [\delta(t) - i\lambda U(t)] \quad (141)$$

for the symmetrical spacecraft.

From (67) and (68), the error time histories are

$$\Omega_{xy} = \tilde{\Omega}_{xy} + \frac{T}{\lambda I} [\sin \lambda t + i(1 - \cos \lambda t)] \quad (142)$$

and

$$\alpha = \tilde{\alpha} + \frac{T}{\sigma I_z} \left[\frac{I_z}{\lambda I} - \frac{1}{\lambda} (\cos \lambda t + i \sin \lambda t) - \frac{1}{\sigma} (\cos \sigma t - i \sin \sigma t) \right] \quad (143)$$

The total error vectors are

$$\Omega_{xy} = \tilde{\Omega}_{xy} + i \left(\frac{T}{\lambda I} \right) (1 - e^{i\lambda t}) \quad (144)$$

and

$$\alpha_I = \tilde{\alpha}_I + \left(\frac{T}{\sigma I_z} \right) \left[\left(\frac{I_z}{\lambda I} \right) e^{i\sigma t} - \frac{1}{\lambda} e^{i(\sigma+\lambda)t} - \frac{1}{\sigma} \right] \quad (145)$$

Curves for the rate error trace are given in figure 17.

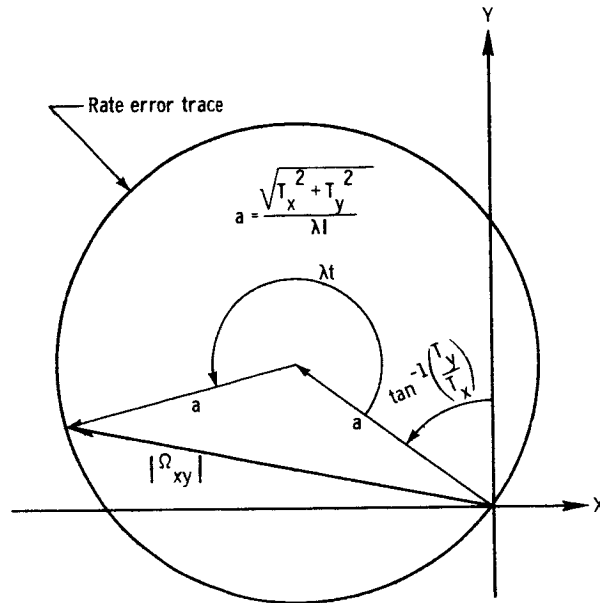


Figure 17.- Rate error trace for step torques and symmetric spacecraft.

The rate error trace is a displaced circle whose center is located by the vector $\frac{iT}{\lambda I}$. The radius of the circle is $\frac{T}{\lambda I}$, and the period of the precessional motion is $\left| \frac{2\pi}{\lambda} \right|$.

Curves for the attitude error trace are depicted in figure 18. This trace is generated by a point on a circle of radius $\frac{\sqrt{T_x^2 + T_y^2}}{\sigma \lambda I_z}$, whose center moves along the circumference of a displaced circle with radius $\frac{\sqrt{T_x^2 + T_y^2}}{\sigma \lambda I}$. The center of this displaced circle is located by the vector $-\frac{T}{\sigma^2 I_z}$ and the period of motion is $2k\pi$, where k is the least common denominator of σ and λ for rational σ and λ .

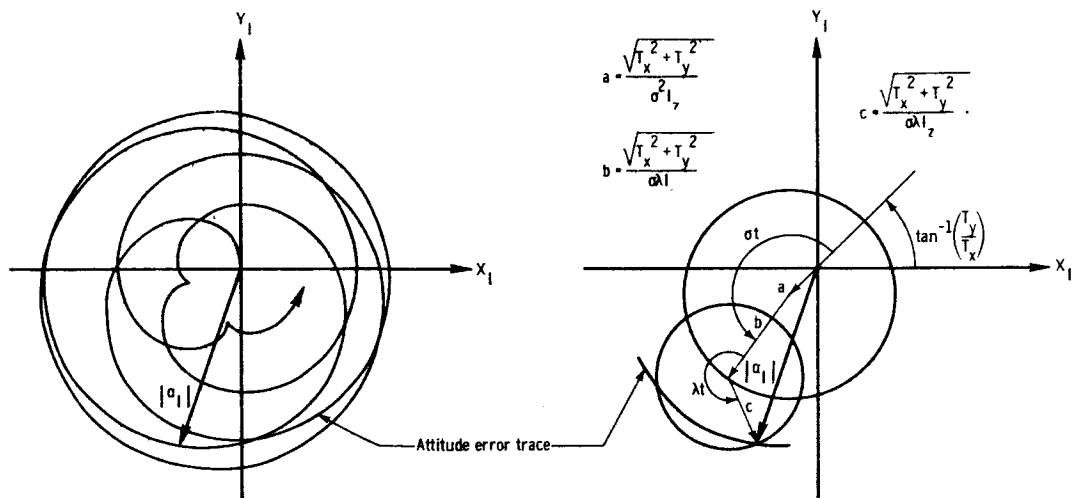


Figure 18.- Attitude error trace for step torques and symmetric spacecraft.

The maximum values of the errors become

$$|\Omega_{xy}|_{\max} = \frac{2 \sqrt{T_x^2 + T_y^2}}{|I_z - I| \sigma} \quad (146)$$

and

$$|\alpha|_{\lim} = \left[\left| \frac{I_z + I}{I_z - I} \right| + 1 \right] \frac{\sqrt{T_x^2 + T_y^2}}{\sigma^2} \quad (147)$$

The error vector relations for the step torques and symmetric spacecraft agree with Thomson's results (ref. 6, pages 198 and 207). Maximum attitude error limits for this disturbance have also been developed by Suddath and include the residual errors after removal of the disturbance (ref. 14, page 8). His limits, which are smaller than or equal to the limits obtainable during the torque application, do not represent the worst case and are thus somewhat misleading.

Note that the error limits are inversely proportional to the inertia difference $|I_z - I|$ and predict minimum errors for a disklike configuration. When applied to a sphere the limits predict divergence, confirming the statement that a sphere cannot be spin-stabilized.

3. Step Products of Inertia

When step products of inertia of the form

$$I_{xz} = \sum_{j=1}^n m_j x_{jo} z_{jo} - m_s x_{so} z_{so}$$

$$I_{yz} = \sum_{j=1}^n m_j y_{jo} z_{jo} - m_s y_{so} z_{so}$$

occur in symmetrical spacecraft, one may introduce

$$I_{rz} \equiv I_{xz} + iI_{yz} \quad (148)$$

to get the forcing function

$$F = - \frac{I_{rz}}{I} \left\{ \lambda \left[\ddot{\delta}(t) + \sigma^2 U(t) \right] - i \left[\ddot{\delta}(t) + \sigma^2 \delta(t) \right] \right\} \quad (149)$$

from (88).

The error solutions (90) and (91) give

$$\Omega_{xy} = \tilde{\Omega}_{xy} + \left(\frac{I_{rz}}{I} \right) \left[\left(\frac{\sigma^2 - \lambda^2}{\lambda} \right) (\cos \lambda t + i \sin \lambda t) - \frac{\sigma^2}{\lambda} + i\delta(t) \right] \quad (150)$$

and

$$\alpha = \tilde{\alpha} + i \left(\frac{I_{rz}}{\lambda I} \right) \left[\sigma - (\sigma - \lambda) (\cos \lambda t + i \sin \lambda t) \right] \quad (151)$$

for the symmetric spacecraft.

In vector form, one has

$$\Omega_{xy} = \tilde{\Omega}_{xy} + \left(\frac{I_{rz}}{I} \right) \left[\left(\frac{\sigma^2 - \lambda^2}{\lambda} \right) e^{i\lambda t} - \frac{\sigma^2}{\lambda} + i\delta(t) \right] \quad (152)$$

and

$$\alpha_I = \tilde{\alpha}_I + i \left(\frac{I_{rz}}{\lambda I} \right) \left[\sigma e^{i\sigma t} - (\sigma - \lambda) e^{i(\sigma + \lambda)t} \right] \quad (153)$$

The polar graph of the rate error is illustrated in figure 19.

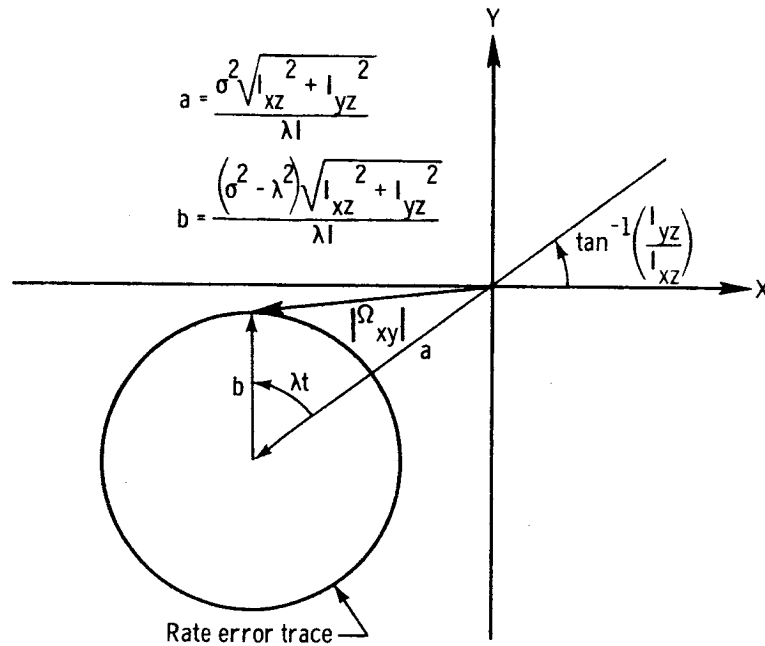


Figure 19.- Rate error trace for step inertia products and symmetric spacecraft.

The error trace is a displaced circle with center determined by the vector $-\frac{\sigma^2 I_{rz}}{\lambda I}$. The radius of the circle is $\left(\frac{\sigma^2 - \lambda^2}{\lambda I} \right) \sqrt{I_{xz}^2 + I_{yz}^2}$ and the precession period of the motion is $\left| \frac{2\pi}{\lambda} \right|$.

The graph of the attitude error for the step product of inertia is given in figure 20.

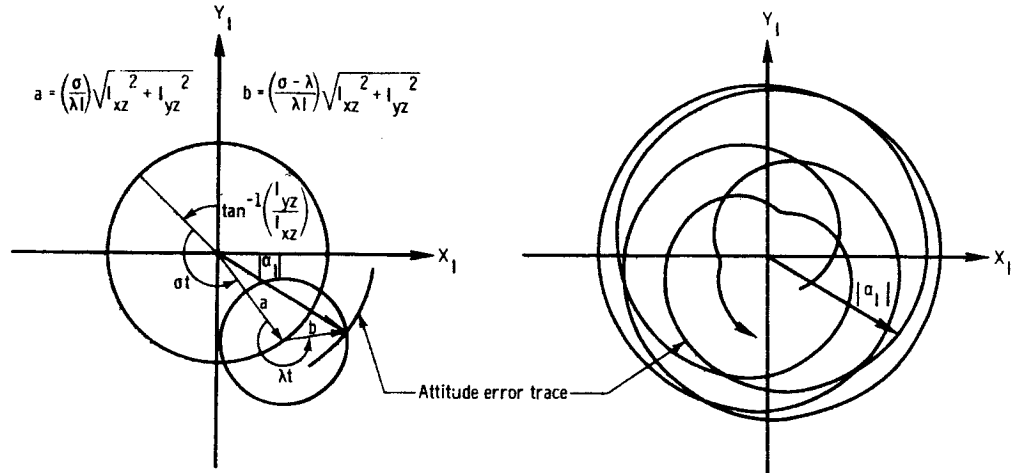


Figure 20.- Attitude error trace for step inertia products and symmetric spacecraft.

The error trace now is produced by a point on a rotating circle with radius $\left(\frac{\sigma - \lambda}{\lambda I}\right) \sqrt{I_{xz}^2 + I_{yz}^2}$ which moves around the circumference of a circle with center at the origin and radius $\left(\frac{\sigma}{\lambda I}\right) \sqrt{I_{xz}^2 + I_{yz}^2}$. The period of motion is $2k\pi$, where k is the least common denominator of σ and λ , and the trace curve does not close unless σ and λ are rational.

Maximum error values become

$$|\Omega_{xy}|_{\max} = \left| \frac{2\sigma^2 - \lambda^2}{\lambda I} \right| \sqrt{I_{xz}^2 + I_{yz}^2} \quad (154)$$

for the rate vector and

$$|\alpha|_{\lim} = \left| \frac{2\sigma - \lambda}{\lambda I} \right| \sqrt{I_{xz}^2 + I_{yz}^2} \quad (155)$$

for the attitude vector.

The errors predicted by (152) to (155) do not agree with previous results (refs. 4, 5, 6) for product of inertia disturbances. This might be expected, however, since the previous analyses have neglected the energy associated with the introduction of the product of inertia.

The limiting errors (154) and (155) diverge for a spherical configuration. Attitude error bounds for a long slender cylinder ($\lambda \rightarrow -\sigma$) are three times as large as the attitude error bounds for a flat disk ($\lambda \rightarrow \sigma$). Rate error bounds for these limiting configurations are, however, equal.

4. Variable Products of Inertia

Forcing functions, stability criteria, and solutions for variable periodic products of inertia and symmetrical spacecraft retain the form (108) to (119). The symmetric spacecraft does, however, permit a simpler combination of the inertia products and yields a better understanding of the effects of the spacecraft parameters on the error traces.

Consider a product of inertia of the form

$$\begin{aligned} I_{rz} &= I_{xz} + iI_{yz} \\ &= Qz_0(x_0 + iy_0) \end{aligned} \tag{156}$$

as produced by the motion of a single mass. Circumferential, radial, and vertical oscillations which yield this inertia product can now be examined.

a. Circumferential Mass Motion

The circumferential mass motion begins at the point $x_0 = r_0 \cos pt_0$, $y_0 = r_0 \sin pt_0$, z_0 and continues at a constant angular rate p around the perimeter of the spacecraft.

The associated position coordinates may be written as

$$\left. \begin{aligned} x &= r_0 \cos p(t + t_0) \\ y &= r_0 \sin p(t + t_0) \\ z &= z_0 U(t_0) \\ r_0 &= \sqrt{x_0^2 + y_0^2} \end{aligned} \right\} \quad (157)$$

where

The solution coefficients are taken from table 5, with the result

$$\left. \begin{aligned} B_4 &= \frac{I_{rz}}{I} \left[\frac{(\sigma + p)^2 - (\lambda^2 - p^2)}{\lambda - p} + \frac{p}{2} \right] \\ B_5 &= - \frac{I_{rz} p}{2I} \\ B_6 &= - \frac{I_{rz} (\sigma + p)^2}{(\lambda - p)I} \\ B_7 &= 0 \end{aligned} \right\} \quad (158)$$

and

$$\left. \begin{aligned} C_4 &= - \frac{p I_{rz}}{I} \left[\frac{2\sigma - \lambda}{\sigma^2 - \lambda^2} \right] \\ C_5 &= - \frac{I_{rz}}{I} \left[\frac{(\sigma + p)^2 - (\lambda^2 - p^2)}{(\sigma + \lambda)(\lambda - p)} + \frac{p}{2(\sigma + \lambda)} \right] \\ C_6 &= \frac{p I_{rz}}{2(\sigma - \lambda)I} \\ C_7 &= \frac{(\sigma + p) I_{rz}}{(\lambda - p)I} \end{aligned} \right\} \quad (159)$$

The rate and attitude error vector equations (116) and (118) reduce to

$$\Omega_{xy} = \tilde{\Omega}_{xy} + \frac{I_{rz}}{I} \left\{ \left[\frac{(\sigma + p)^2 - (\lambda^2 - p^2)}{\lambda - p} + \frac{p}{2} \right] e^{i\lambda t} - \frac{p}{2} e^{-i\lambda t} - \frac{(\sigma + p)^2}{(\lambda - p)} e^{ipt} + i\delta(t) \right\} \quad (160)$$

and

$$\alpha_I = \tilde{\alpha}_I - \frac{iI_{rz}}{I} \left\{ \left[\frac{p(2\sigma - \lambda)}{\sigma^2 - \lambda^2} \right] + \left[\frac{(\sigma + p)^2 - (\lambda^2 - p^2)}{(\sigma + \lambda)(\lambda - p)} + \frac{p}{2(\sigma + \lambda)} \right] e^{i(\sigma + \lambda)t} - \left[\frac{p}{2(\sigma - \lambda)} \right] e^{i(\sigma - \lambda)t} - \left[\frac{\sigma + p}{\lambda - p} \right] e^{i(\sigma + p)t} \right\} \quad (161)$$

The rate vector trace, illustrated in figure 21,

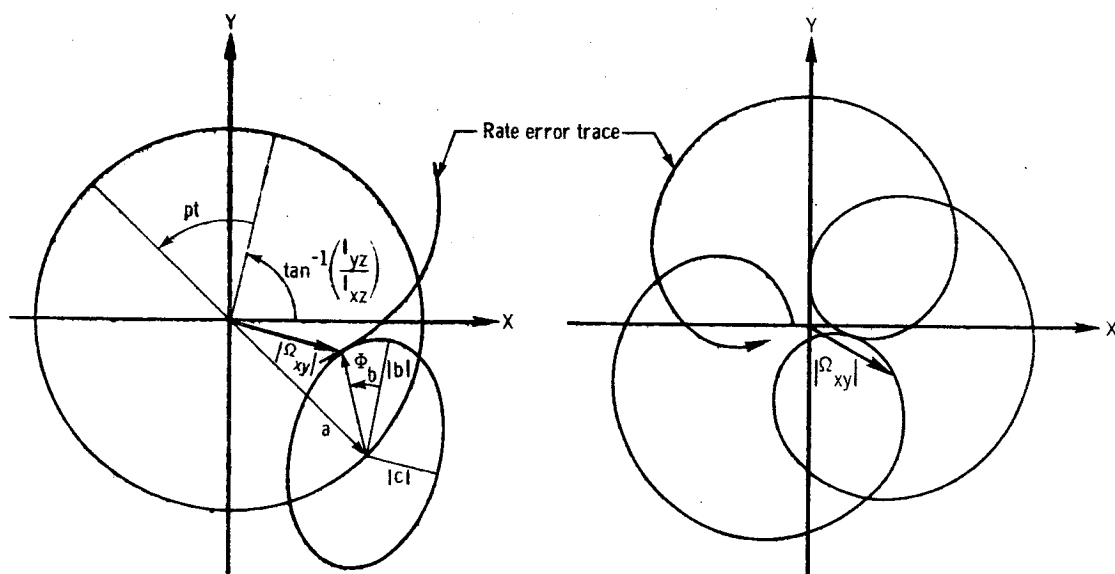


Figure 21.- Rate error trace for circumferential mass motion and symmetric spacecraft.

is produced by an ellipse, whose center travels along the circumference of a circle.

The radius of this circle is

$$a = \left[\frac{(\sigma + p)^2}{\lambda - p} \right] \frac{\sqrt{I_{xz}^2 + I_{yz}^2}}{I} \quad (162)$$

and the ellipse center is determined by the angle ϕ_t , measured from the axis corresponding to the radial inertia product. The ellipse semiaxis $|b|$ also lies along the radial inertia product axis, and the precession angle of the rate vector tip within the ellipse is

$$\phi_b = \tan^{-1} \left(\frac{c}{b} \tan^{-1} \lambda t \right) \quad (163)$$

where

$$\left. \begin{aligned} b &= \left[\frac{(\sigma + p)^2}{\lambda - p} - (\lambda + p) \right] \frac{\sqrt{I_{xz}^2 + I_{yz}^2}}{I} \\ \text{and} \\ c &= \left[\frac{(\sigma + p)^2}{\lambda - p} - \lambda \right] \frac{\sqrt{I_{xz}^2 + I_{yz}^2}}{I} \end{aligned} \right\} \quad (164)$$

define the ellipse semiaxes.

The attitude error trace in inertial space, shown in figure 22, is derived by a rotating ellipse whose center translates along the circumference of a displaced circle.

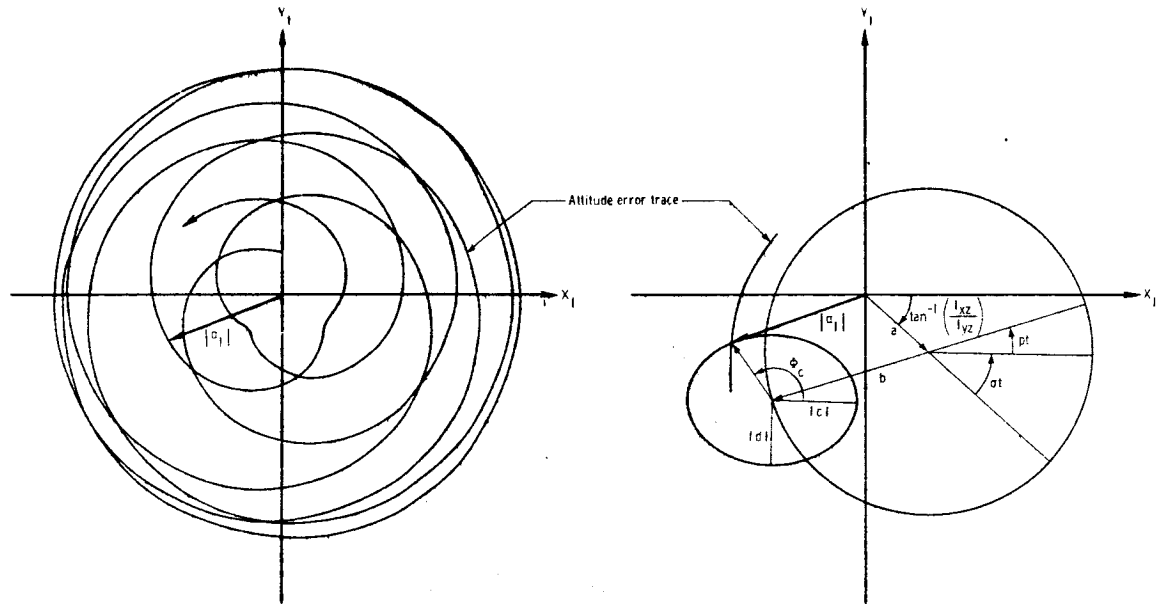


Figure 22.- Attitude error trace for circumferential mass motion and symmetric spacecraft.

The center of the displaced circle is located by

$$a = \left(\frac{p(2\sigma - \lambda)}{\sigma^2 - \lambda^2} \right) \frac{\sqrt{I_{xz}^2 + I_{yz}^2}}{I} \quad (165)$$

and the circle radius becomes

$$b = \left(\frac{\sigma + p}{\lambda - p} \right) \frac{\sqrt{I_{xz}^2 + I_{yz}^2}}{I} \quad (166)$$

The center of the moving ellipse is specified by the angle $(\sigma + p)t$ and the semiaxis $|c|$ rotates at the spin rate.

The angle to the attitude vector tip and the semiaxes of the ellipse are found from

$$\Phi_c = \tan^{-1} \left[\frac{d}{c} \tan \lambda t \right] \quad (167)$$

and

$$\left. \begin{aligned} c &= \left[\frac{(\sigma + p)^2 - (\lambda^2 - p^2)}{\lambda - p} - \frac{p\lambda}{\sigma - \lambda} \right] \frac{\sqrt{I_{xz}^2 + I_{yz}^2}}{(\sigma + \lambda)I} \\ d &= \left[\frac{(\sigma + p)^2 - (\lambda^2 - p^2)}{\lambda - p} + \frac{p\sigma}{\sigma - \lambda} \right] \frac{\sqrt{I_{xz}^2 + I_{yz}^2}}{(\sigma + \lambda)I} \end{aligned} \right\} \quad (168)$$

respectively.

Limiting error values can be computed from the upper bound relations

$$\begin{aligned} |\alpha_{xy}|_{\lim} &= \left[\left| \frac{(\sigma + p)^2 - (\lambda^2 - p^2)}{\lambda - p} + \frac{p}{2} \right| + \left| \frac{p}{2} \right| \right. \\ &\quad \left. + \left| \frac{(\sigma + p)^2}{\lambda - p} \right| \frac{\sqrt{I_{xz}^2 + I_{yz}^2}}{I} \right] \end{aligned} \quad (169)$$

and

$$\begin{aligned} |\alpha|_{\lim} &= \left[\left| \frac{p(2\sigma - \lambda)}{\sigma^2 - \lambda^2} \right| + \left| \frac{(\sigma + p)^2 - (\lambda^2 - p^2)}{(\sigma + \lambda)(\lambda - p)} + \frac{p}{2(\sigma + \lambda)} \right| \right. \\ &\quad \left. + \left| \frac{p}{2(\sigma - \lambda)} \right| + \left| \frac{\sigma + p}{\lambda - p} \right| \frac{\sqrt{I_{xz}^2 + I_{yz}^2}}{I} \right] \end{aligned} \quad (170)$$

These results indicate that the rate and attitude errors for the circumferential motion will be larger than those for the static products of inertia, for which p vanishes. The limiting errors increase with an increase in p and tend to diverge as p approaches λ . For values of p greater than λ , the error continues to increase with an increase in p .

For very small disturbance frequencies ($|p| \ll |\lambda|$), the upper error bounds are given by

$$|\Omega_{xy}|_{\lim} \approx \left| \frac{2\sigma^2 - \lambda^2}{\lambda} \right| \frac{\sqrt{I_{xz}^2 + I_{yz}^2}}{I} \quad (171)$$

and

$$|\alpha|_{\lim} \approx \left| \frac{2\sigma - \lambda}{\lambda} \right| \frac{\sqrt{I_{xz}^2 + I_{yz}^2}}{I} \quad (172)$$

As might be expected, the maximum errors now resemble the error bounds for the step products of inertia. The resultant bounds are essentially independent of the disturbance frequency.

For very large disturbance frequencies ($p \gg \sigma$), one has

$$|\Omega_{xy}|_{\lim} \approx \frac{4|p| \sqrt{I_{xz}^2 + I_{yz}^2}}{I} \quad (173)$$

and

$$|\alpha|_{\lim} \approx \left| \frac{p(5\sigma - 3\lambda)}{\sigma^2 - \lambda^2} \right| \frac{\sqrt{I_{xz}^2 + I_{yz}^2}}{I} \quad (174)$$

so that both error bounds increase linearly with $|p|$ for this case.

The relations (171) to (174) can be used to determine error limits and their variation with the disturbance characteristics, when the absolute disturbance frequency is much less than the absolute precession rate or when the absolute disturbance frequency is much greater than the spin rate.

b. Radial Mass Oscillation

The radial mass motion begins at the point $0, 0, z_0$ and is defined by the coordinates

$$\left. \begin{aligned} x &= x_0 \sin pt \\ y &= y_0 \sin pt \\ z &= z_0 U(t) \end{aligned} \right\} \quad (175)$$

The solution coefficients, taken from table 5, now become

$$\left. \begin{aligned} B_4 &= \frac{ipI_{rz}}{I} \left[\frac{1}{2} - \frac{\sigma^2 + 2\sigma\lambda + p^2}{\lambda^2 - p^2} \right] \\ B_5 &= \frac{ipI_{rz}}{2I} \\ B_6 &= \frac{i(\sigma + p)^2 I_{rz}}{2(\lambda - p)I} \\ B_7 &= \frac{-i(\sigma - p)^2 I_{rz}}{2(\lambda + p)I} \end{aligned} \right\} \quad (176)$$

and

$$\left. \begin{aligned} C_4 &= \frac{ip(2\sigma - \lambda)I_{rz}}{(\sigma^2 - \lambda^2)I} \\ C_5 &= - \left[\frac{ipI_{rz}}{(\sigma + \lambda)I} \right] \left[\frac{1}{2} - \frac{\sigma^2 + 2\sigma\lambda + p^2}{\lambda^2 - p^2} \right] \\ C_6 &= - \frac{ipI_{rz}}{2(\sigma - \lambda)I} \\ C_7 &= - \frac{i(\sigma + p)I_{rz}}{2(\lambda - p)I} \\ C_8 &= \frac{i(\sigma - p)I_{rz}}{2(\lambda + p)I} \end{aligned} \right\} \quad (177)$$

Rate and attitude vectors are

$$\begin{aligned} \Omega_{xy} = \tilde{\Omega}_{xy} + \frac{ipI_{rz}}{2I} \left\{ \left[1 - \frac{2(\sigma^2 + 2\sigma\lambda + p^2)}{\lambda^2 - p^2} \right] e^{i\lambda t} + e^{-i\lambda t} \right. \\ \left. + \left[\frac{(\sigma + p)^2}{p(\lambda - p)} \right] e^{ipt} - \left[\frac{(\sigma - p)^2}{p(\lambda + p)} \right] e^{-ipt} \right\} \end{aligned} \quad (178)$$

and

$$\begin{aligned} \alpha_I = \tilde{\alpha}_I - \frac{pI_{rz}}{2I} \left\{ \left[\frac{2(2\sigma - \lambda)}{\sigma^2 - \lambda^2} \right] - \left(\frac{1}{\sigma + \lambda} \right) \left[1 - \frac{2(\sigma^2 + 2\sigma\lambda + p^2)}{\lambda^2 - p^2} \right] e^{i(\sigma + \lambda)t} \right. \\ \left. - \left(\frac{1}{\sigma - \lambda} \right) e^{i(\sigma - \lambda)t} - \left[\frac{\sigma + p}{p(\lambda - p)} \right] e^{i(\sigma + p)t} + \left[\frac{\sigma - p}{p(\lambda + p)} \right] e^{i(\sigma - p)t} \right\} \end{aligned} \quad (179)$$

as determined from substitution of (176) and (177) into (116) and (118).

The rate error trace is shown in figure 23.

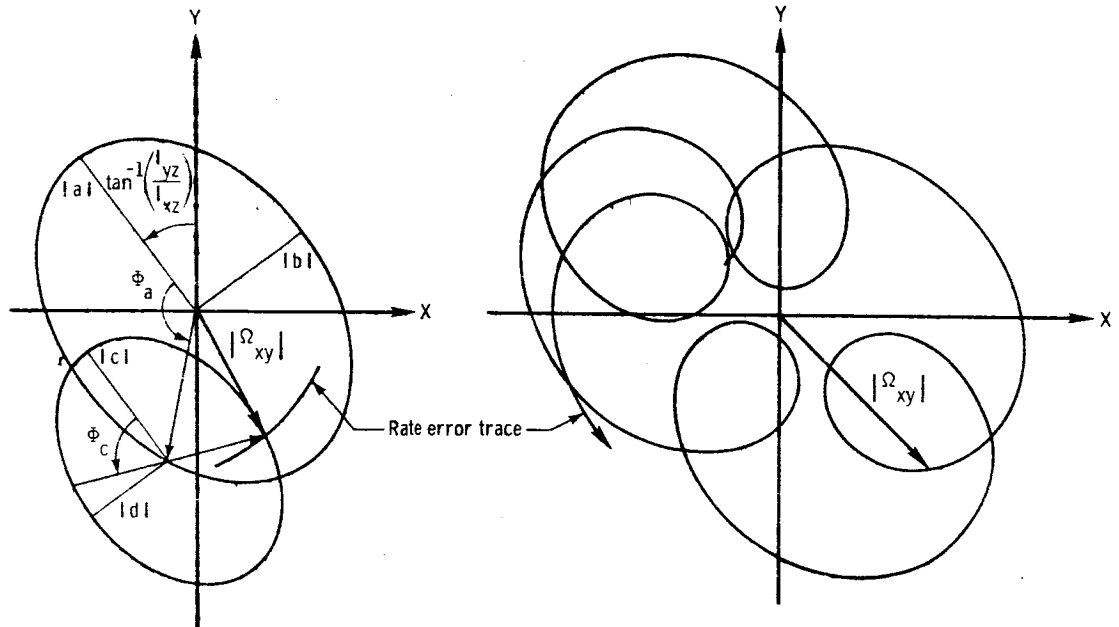


Figure 23.- Rate error trace for radial mass oscillation and symmetric spacecraft.

This trace is generated by two ellipse envelopes, whose semiaxes $|a|$ and $|c|$ lie along a line normal to the radial product of inertia axis. The characteristics of these ellipse envelopes are developed from

$$\left. \begin{aligned} a &= p \left[\frac{\sigma^2 + 2\sigma\lambda + \lambda^2}{\lambda^2 - p^2} \right] \frac{\sqrt{I_{xz}^2 + I_{yz}^2}}{I} \\ b &= \left[\frac{(\sigma^2 + p^2)\lambda + 2\sigma p^2}{\lambda^2 - p^2} \right] \frac{\sqrt{I_{xz}^2 + I_{yz}^2}}{I} \\ c &= p \left[\frac{\sigma^2 + 2\sigma\lambda + p^2}{\lambda^2 - p^2} - 1 \right] \frac{\sqrt{I_{xz}^2 + I_{yz}^2}}{I} \\ d &= p \left[\frac{\sigma^2 + 2\sigma\lambda + p^2}{\lambda^2 - p^2} \right] \frac{\sqrt{I_{xz}^2 + I_{yz}^2}}{I} \end{aligned} \right\} \quad (180)$$

and the precession angles within the ellipses become

$$\left. \begin{aligned} \Phi_a &= \tan^{-1} \left[\frac{b}{a} \tan pt \right] \\ \Phi_c &= \tan^{-1} \left[\frac{d}{c} \tan \lambda t \right] \end{aligned} \right\} \quad (181)$$

The attitude error trace is also derived from two ellipses and takes the form illustrated in figure 24.

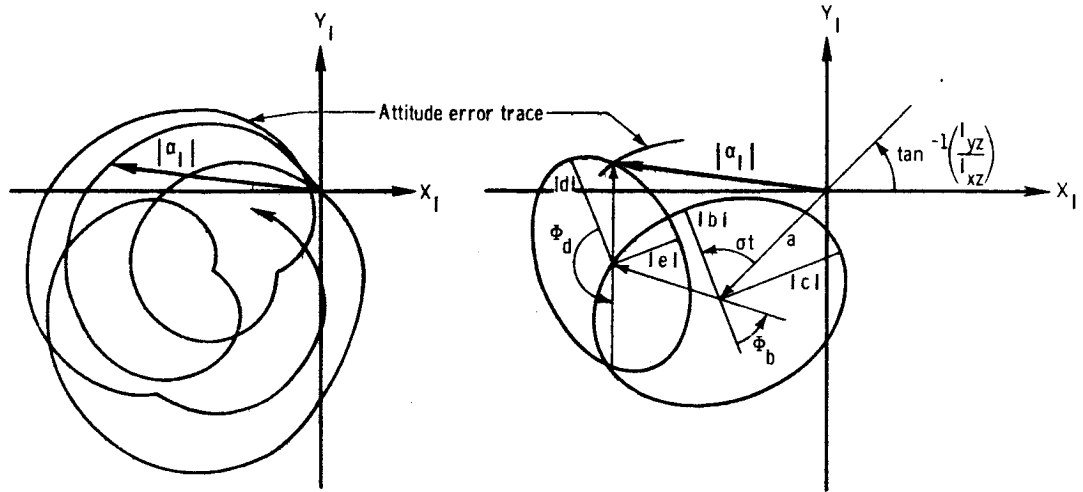


Figure 24.- Attitude error trace for radial mass motion oscillation and symmetric spacecraft.

The ellipse semiaxes $|b|$ and $|d|$ initially coincide with the radial-inertia-product axis and precess at the spin rate. The center of the inner ellipse is given by

$$a = \left[\frac{p(2\sigma - \lambda)}{\sigma^2 - \lambda^2} \right] \frac{\sqrt{I_{xz}^2 + I_{yz}^2}}{I} \quad (182)$$

and the semiaxes for the two rotating ellipses become

$$\left. \begin{aligned} b &= \left[\frac{p(\sigma + \lambda)}{\lambda^2 - p^2} \right] \frac{\sqrt{I_{xz}^2 + I_{yz}^2}}{I} \\ c &= \left[\frac{\sigma\lambda + p^2}{\lambda^2 - p^2} \right] \frac{\sqrt{I_{xz}^2 + I_{yz}^2}}{I} \end{aligned} \right\} \quad (183)$$

$$\left. \begin{aligned} d &= \left(\frac{p}{\sigma + \lambda} \right) \left[\frac{\sigma^2 + 2\sigma\lambda + p^2}{\lambda^2 - p^2} - \frac{\sigma}{\sigma - \lambda} \right] \frac{\sqrt{I_{xz}^2 + I_{yz}^2}}{I} \\ e &= \left(\frac{p}{\sigma + \lambda} \right) \left[\frac{\sigma^2 + 2\sigma\lambda + p^2}{\lambda^2 - p^2} + \frac{\lambda}{\sigma - \lambda} \right] \frac{\sqrt{I_{xz}^2 + I_{yz}^2}}{I} \end{aligned} \right\} \quad (183)$$

from (179). The precession angles within the ellipses are

$$\left. \begin{aligned} \Phi_b &= \tan^{-1} \left[\frac{c}{b} \tan^{-1} pt \right] \\ \Phi_d &= \tan^{-1} \left[\frac{e}{d} \tan^{-1} \lambda t \right] \end{aligned} \right\} \quad (184)$$

and

The upper bounds of the error magnitudes become

$$\begin{aligned} |\Omega_{xy}|_{\lim} &= \left[1 + \left| 1 - \frac{2(\sigma^2 + 2\sigma\lambda + p^2)}{\lambda^2 - p^2} \right| + \left| \frac{(\sigma + p)^2}{p(\lambda - p)} \right| \right. \\ &\quad \left. + \left| \frac{(\sigma - p)^2}{p(\lambda + p)} \right| \right] \frac{|p| \sqrt{I_{xz}^2 + I_{yz}^2}}{2I} \end{aligned} \quad (185)$$

and

$$\begin{aligned} |\alpha|_{\lim} &= \left[\left| \frac{2(2\sigma - \lambda)}{\sigma^2 - \lambda^2} \right| + \frac{1}{\sigma + \lambda} \left| 1 - \frac{2(\sigma^2 + 2\sigma\lambda + p^2)}{\lambda^2 - p^2} \right| + \frac{1}{\sigma - \lambda} \right. \\ &\quad \left. + \left| \frac{\sigma + p}{p(\lambda - p)} \right| + \left| \frac{\sigma - p}{p(\lambda + p)} \right| \right] \frac{|p| \sqrt{I_{xz}^2 + I_{yz}^2}}{2I} \end{aligned} \quad (186)$$

These error limits again increase as $|p|$ increases and diverge as $|p|$ approaches $|\lambda|$.

When the disturbance frequency is very small ($|p| \ll |\lambda|$), one may use

$$|\Omega_{xy}|_{\lim} \cong \left| \frac{\sigma^2}{\lambda} \right| \frac{\sqrt{I_{xz}^2 + I_{yz}^2}}{I} \quad (187)$$

and

$$|\alpha|_{\text{lim}} \cong \left| \frac{\sigma}{\lambda} \right| \frac{\sqrt{I_{xz}^2 + I_{yz}^2}}{I} \quad (188)$$

as the approximate upper bounds for the rate and attitude errors. These upper bounds correspond to the maximum principal-axis rotation for the inertia product and do not contain the disturbance frequency.

When the disturbance frequency is very large ($|p| \gg \sigma$), one has

$$|\alpha_{xy}|_{\text{lim}} \cong \frac{2|p| \sqrt{I_{xz}^2 + I_{yz}^2}}{I} \quad (189)$$

and

$$|\alpha|_{\text{lim}} = \left| \frac{2p(2\sigma - \lambda)}{\sigma^2 - \lambda^2} \right| \frac{\sqrt{I_{xz}^2 + I_{yz}^2}}{I} \quad (190)$$

The upper bounds (189) and (190) increase linearly with $|p|$.

A comparison of (171) to (174) with (187) to (190) shows that the errors for the radial mass oscillation will be smaller than those predicted for the circumferential mass motion, when the disturbance (p , I_{rz}) and spacecraft (σ , λ , I) characteristics are equal.

c. Vertical Mass Oscillation

The vertical mass oscillation comprises a periodic mass motion, which starts at the point x_0 , y_0 , 0 and is described by

$$\left. \begin{aligned} x &= x_0 \\ y &= y_0 \\ z &= z_0 \sin pt \end{aligned} \right\} \quad (191)$$

The solution coefficients for this motion are

$$\left. \begin{aligned} B_4 &= - \frac{ip(\sigma^2 - p^2)I_{rz}}{(\lambda^2 - p^2)I} \\ B_5 &= 0 \\ B_6 &= \frac{i(\sigma^2 - p^2)I_{rz}}{2(\lambda - p)I} \\ B_7 &= - \frac{i(\sigma^2 - p^2)I_{rz}}{2(\lambda + p)I} \end{aligned} \right\} \quad (192)$$

and

$$\left. \begin{aligned} C_4 &= \frac{-ipI_{rz}}{(\sigma + \lambda)I} \\ C_5 &= \frac{ip(\sigma^2 - p^2)I_{rz}}{(\sigma + \lambda)(\lambda - p)I} \\ C_6 &= 0 \\ C_7 &= - \frac{i(\sigma - p)I_{rz}}{2(\lambda - p)I} \\ C_8 &= \frac{i(\sigma + p)I_{rz}}{2(\lambda + p)I} \end{aligned} \right\} \quad (193)$$

The error vectors, as developed from (116) and (118), yield

$$\Omega_{xy} = \tilde{\Omega}_{xy} - \frac{i(\sigma^2 - p^2)I_{rz}}{2(\lambda^2 - p^2)I} \left[2pe^{i\lambda t} - (\lambda + p)e^{ipt} + (\lambda - p)e^{-ipt} \right] \quad (194)$$

and

$$\alpha_I = \tilde{\alpha}_I + \frac{I_{rz}}{I} \left\{ \frac{p}{\sigma + \lambda} \left[1 - \left(\frac{\sigma^2 - p^2}{\lambda^2 - p^2} \right) e^{i(\sigma - \lambda)t} \right] + \frac{1}{2} \left[\left(\frac{\sigma - p}{\lambda - p} \right) e^{i(\sigma + p)t} - \left(\frac{\sigma + p}{\lambda + p} \right) e^{i(\sigma - p)t} \right] \right\} \quad (195)$$

The rate error trace for the vertical periodic motions is given in figure 25.

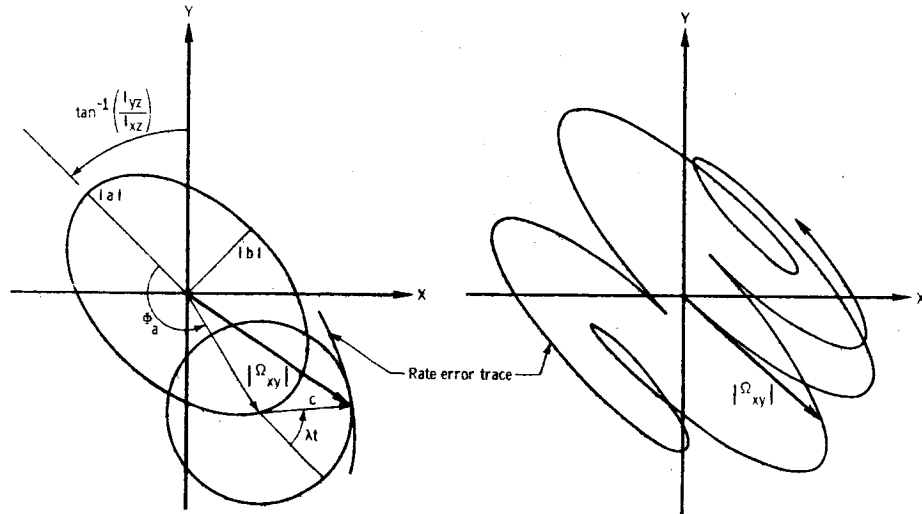


Figure 25.- Rate error trace for vertical mass oscillation and symmetric spacecraft.

This trace is generated by a point on a circle, whose center traces out an ellipse in the XY plane. At time zero, both the ellipse semiaxis $|a|$ and the circle radius vector lie along an axis, which is perpendicular to the mass position radius. The ellipse semiaxes are computed from

$$\left. \begin{aligned} a &= \left[\frac{\lambda(\sigma^2 - p^2)}{\lambda^2 - p^2} \right] \frac{\sqrt{I_{xz}^2 + I_{yz}^2}}{I} \\ b &= \left[\frac{p(\sigma^2 - p^2)}{\lambda^2 - p^2} \right] \frac{\sqrt{I_{xz}^2 + I_{yz}^2}}{I} \end{aligned} \right\} \quad (196)$$

and the circle radius is

$$c = \left[\frac{p(\sigma^2 - p^2)}{\lambda^2 - p^2} \right] \frac{\sqrt{I_{xz}^2 + I_{yz}^2}}{I} \quad (197)$$

The location of the center of the circle along the ellipse is

$$\phi_a = \tan^{-1} \left[\frac{p}{\lambda} \tan pt \right] \quad (198)$$

and the rate vector tip precesses at the rate λ within the circle.

The attitude error trace is sketched in figure 26.

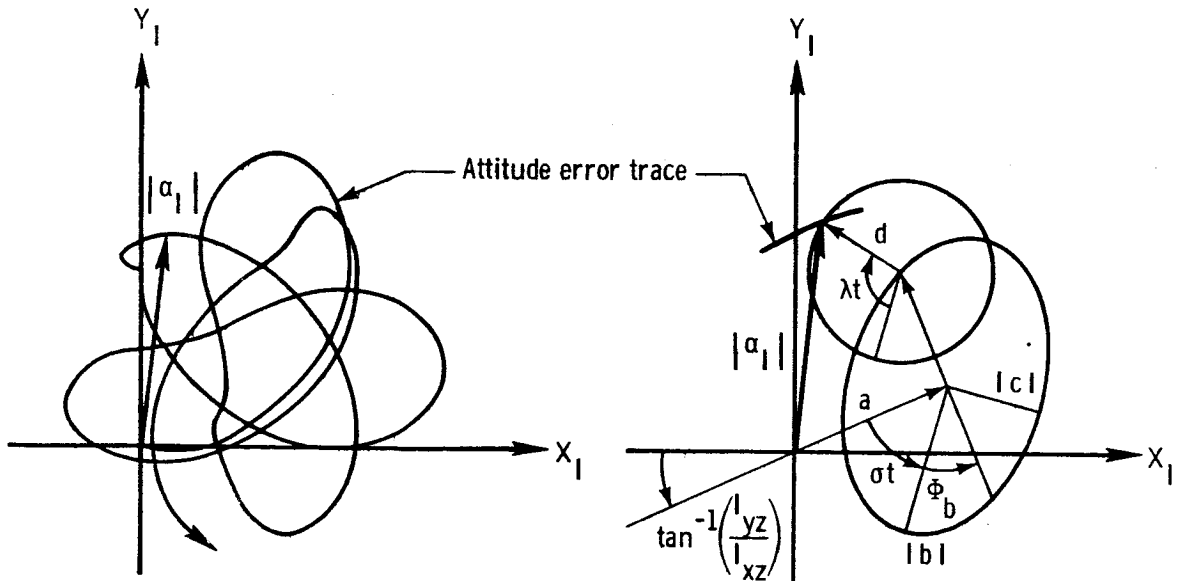


Figure 26.- Attitude error trace for vertical mass oscillation and symmetric spacecraft.

The trace curve is produced by a circle which travels along the p ellipse. Both circle and ellipse rotate at the spin rate σ , and are initially aligned with the radial product of inertia axis. The center of the ellipse is determined from

$$a = \left(\frac{p}{\sigma + \lambda} \right) \frac{\sqrt{I_{xz}^2 + I_{yz}^2}}{I} \quad (199)$$

and the ellipse semiaxes are given by

$$\left. \begin{aligned} b &= \left[\frac{p(\sigma - \lambda)}{\lambda^2 - p^2} \right] \frac{\sqrt{I_{xz}^2 + I_{yz}^2}}{I} \\ \text{and} \\ c &= \left[\frac{\sigma\lambda - p^2}{\lambda^2 - p^2} \right] \frac{\sqrt{I_{xz}^2 + I_{yz}^2}}{I} \end{aligned} \right\} \quad (200)$$

The center of the precessing circle is at

$$\Phi_b = \tan^{-1} \left[\frac{c}{b} \tan pt \right] \quad (201)$$

and the radius of the circle becomes

$$d = \left[\frac{p(\sigma^2 - p^2)}{(\sigma + \lambda)(\lambda^2 - p^2)} \right] \frac{\sqrt{I_{xz}^2 + I_{yz}^2}}{I} \quad (202)$$

This radius moves with the precession rate λ within the circular envelope.

Values for the upper limits of the rate and attitude error magnitudes may be calculated by using

$$|\Omega_{xy}|_{\lim} = \left| \frac{\sigma^2 - p^2}{\lambda^2 - p^2} \right| \left[|p| + \frac{1}{2} \left(|\lambda - p| + |\lambda + p| \right) \right] \frac{\sqrt{I_{xz}^2 + I_{yz}^2}}{I} \quad (203)$$

and

$$|\alpha|_{\text{lim}} = \left[\left| \frac{p}{\sigma + \lambda} \right| \left(1 + \left| \frac{\sigma^2 - p^2}{\lambda^2 - p^2} \right| \right) + \frac{1}{2} \left(\left| \frac{\sigma + p}{\lambda + p} \right| + \left| \frac{\sigma - p}{\lambda - p} \right| \right) \right] \frac{\sqrt{I_{xz}^2 + I_{yz}^2}}{I} \quad (204)$$

The upper bounds of the errors increase as p increases. The instability trend at $|p| = |\lambda|$ is obvious from (203) and (204).

If $|p|$ is small ($|p| \ll |\lambda|$), these equations yield

$$|\Omega_{xy}|_{\text{lim}} \approx \left| \frac{\sigma^2}{\lambda} \right| \frac{\sqrt{I_{xz}^2 + I_{yz}^2}}{I} \quad (205)$$

and

$$|\alpha|_{\text{lim}} \approx \left| \frac{\sigma}{\lambda} \right| \frac{\sqrt{I_{xz}^2 + I_{yz}^2}}{I} \quad (206)$$

so that both error bounds are approximately independent of $|p|$ and contain only the terms associated with the principal-axis rotation.

If $|p|$ is large ($|p| \gg \sigma$), the upper bounds reduce to

$$|\Omega_{xy}|_{\text{lim}} \approx \frac{2|p| \sqrt{I_{xz}^2 + I_{yz}^2}}{I} \quad (207)$$

and

$$|\alpha|_{\text{lim}} = 2 \left| \frac{p}{\sigma} \right| \frac{\sqrt{I_{xz}^2 + I_{yz}^2}}{I_z} \quad (208)$$

as a first approximation. Both these error bounds are directly proportional to $|p|$.

From (171)-(174), (187)-(190), and (205)-(208) it can be seen that the error bounds predicted for the vertical mass oscillation closely resemble those developed for the radial mass oscillation. The attitude

errors for the periodic vertical motions will, however, be somewhat lower than the attitude errors for the periodic radial motions, when the disturbance and spacecraft characteristics are equal.

In concluding this discussion of the variable products of inertia for symmetric spacecraft, one observes that the variation of the limiting errors with inertia distribution is similar to that described for the step products of inertia. Flat disk configurations yield the minimum errors, and spherical configurations are unstable. However, the magnitudes of the rate and attitude errors are now considerably larger than the errors produced by the step products of inertia.

E. Controlled Spacecraft Characteristics

1. Governing Equations

The motion of the controlled spacecraft can be defined by a method similar to that for the uncontrolled case. The torques produced by the control system are now particular functions of the measured vehicle angular position and rate. These torques can thus be considered as forcing functions applied to the uncontrolled vehicle equations. The solutions of the resultant differential equations yield the spacecraft's angular position and rate errors, as before.

The analysis begins with the selection of a control torque command and the development of the corresponding equations of motion. As an example, a linear control torque g will be introduced as

$$\begin{aligned}
 g = g_x I_x + i g_y I_y = & \left[K_{1x} \Omega_x + K_{2x} \int^t \Omega_y dt + K_{3x} \theta + \dots \right] \\
 & + i \left[K_{1y} \Omega_y + K_{2y} \int^t \Omega_x dt + K_{3y} \phi + \dots \right] \quad (209)
 \end{aligned}$$

where the K_{jk} are the physical control gains that must be provided by the stabilization system. The error signals are amplified by these gains, and a control moment, whose value is equal to the sum of the amplified error terms given by (209), is then applied to the spacecraft.

Particular nonlinear control torques, which lead to governing equations of the form discussed in the literature (refs. 21-24) could also be considered. The present application will, however, be restricted to a discussion of the linear control functions in (209). These linear control laws can be readily mechanized and allow a simple interpretation of the mechanics of motion for various types of sensor inputs (such as those derived directly from rate gyros, stable platforms, or Euler angle computers).

In an analysis of the spacecraft's stability, it is easier to deal with nondimensional control gains. One may define such gains by

$$\begin{aligned}
 & k_{1x} = \frac{K_{1x}}{\lambda I_x} \quad k_{2x} = \frac{K_{2x}}{\lambda \lambda_y I_y} \quad k_{3x} = \frac{K_{3x}}{\sigma \lambda I_x} \\
 \text{and} \quad & k_{1y} = \frac{K_{1y}}{\lambda I_y} \quad k_{2y} = \frac{K_{2y}}{\lambda \lambda_x I_x} \quad k_{3y} = \frac{K_{3y}}{\sigma \lambda I_y} \quad (210)
 \end{aligned}$$

so that g_x and g_y become

$$\left. \begin{aligned} g_x &= \lambda \left[k_{1x} \Omega_x + k_{2x} \left(\frac{\lambda_y I_y}{I_x} \right) \int^t \Omega_y dt + \sigma k_{3x} \theta + \dots \right] \\ \text{and} \\ g_y &= \lambda \left[k_{1y} \Omega_y + k_{2y} \left(\frac{\lambda_x I_x}{I_y} \right) \int^t \Omega_x dt + \sigma k_{3y} \varphi + \dots \right] \end{aligned} \right\} \quad (211)$$

The equations of motion can now be written in the form

$$\left. \begin{aligned} \dot{\Omega}_x + \left(\frac{\lambda_y I_y}{I_x} \right) \Omega_y &= g_x + f_x \\ \text{and} \\ \dot{\Omega}_y - \left(\frac{\lambda_x I_x}{I_y} \right) \Omega_x &= g_y + f_y \end{aligned} \right\} \quad (212)$$

where

$$\begin{aligned} f_x &= \frac{1}{I_x} \left\{ M_x + \sigma (\dot{I}_{xz} - I_{yz} \sigma) + \left[\sum_{j=1}^n m_j (z_j \dot{x}_j - x_j \dot{z}_j) - m_s (z_s \dot{x}_s - x_s \dot{z}_s) \right] \sigma \right. \\ &\quad \left. + \sum_{j=1}^n m_j (z_j \ddot{y}_j - y_j \ddot{z}_j) - m_s (z_s \ddot{y}_s - y_s \ddot{z}_s) \right\} \\ &= \frac{1}{I_x} \left\{ M_x - \sum_{j=1}^n m_j \left[z_j (\sigma^2 y_j - 2\sigma \dot{x}_j + \ddot{y}_j) + \ddot{z}_j y_j \right] \right. \\ &\quad \left. + m_s \left[z_s (\sigma^2 y_s - 2\sigma \dot{x}_s + \ddot{y}_s) + \ddot{z}_s y_s \right] \right\} \end{aligned} \quad (213)$$

and

$$\begin{aligned}
 f_y &= \frac{1}{I_y} \left\{ M_y + \sigma(\dot{I}_{yz} + I_{xz}\sigma) + \left[\sum_{j=1}^n m_j(z_j\dot{y}_j - y_j\dot{z}_j) - m_s(z_s\dot{y}_s - y_s\dot{z}_s) \right] \sigma \right. \\
 &\quad \left. + \sum_{j=1}^n m_j(x_j\ddot{z}_j - z_j\ddot{x}_j) - m_s(x_s\ddot{z}_s - z_s\ddot{x}_s) \right\} \\
 &= \frac{1}{I_y} \left\{ M_y + \sum_{j=1}^n m_j \left[z_j(\sigma^2 x_j + 2\sigma\dot{y}_j - \ddot{x}_j) + \ddot{z}_j x_j \right] \right. \\
 &\quad \left. - m_s \left[z_s(\sigma^2 x_s + 2\sigma\dot{y}_s - \ddot{x}_s) + \ddot{z}_s x_s \right] \right\} \quad (214)
 \end{aligned}$$

with the spin rate σ taken as constant and positive.

The Euler angle relations may be expressed as

$$\left. \begin{aligned} \dot{\phi} - \sigma\theta &= \Omega_x \\ \dot{\theta} + \sigma\phi &= \Omega_y \end{aligned} \right\} \quad (215)$$

and the simultaneous solution of (212) and (215) will specify the spacecraft's motion.

2. Control Requirements

In practice, the spacecraft's rate and inertial position errors must be kept within specified deadbands which are determined by the spacecraft mission requirements. Control of the spacecraft to these accuracies may be provided by a reaction jet system and a momentum storage system, and the torques that must be produced by the system actuators can be readily

determined if the required control torques about the body axes are specified. With a reaction jet system, these torques are generated by variable-mass-flow or pulse-modulated jets, and for a momentum storage system composed of control moment gyros or reaction wheels the corresponding torque components along the gyro gimbal or reaction wheel axis are computed and applied. Concern will be given to the actual mechanization of such systems later; for the time being only the body axis torques necessary to stabilize the spacecraft will be developed.

Since the magnitude of the angular error in inertial space is equal to the magnitude of the body-referred angular error, the damping of α and Ω_{xy} will assure the adequate stabilization of the spacecraft with respect to both body-fixed and inertial frames. The problem is thus reduced to the determination of control torques that will damp α and Ω_{xy} to zero or to small steady state values.

3. Control Law Formulation

To investigate particular control laws, the corresponding control torque functions g_x and g_y must first be specified. The associated governing equations follow from (212) and (215). The stability regions for the governing equations can then be defined by making use of the conditions developed by Routh (ref. 11) and Hurwitz (ref. 25). If the selected control torques allow stable solutions for the Euler angles or body rates, time histories and complex error solutions can be found by the Laplace transform technique or by numerical integration of the linearized equations. If no stable solutions are possible, the control torques can be rejected immediately.

To illustrate the applications of this technique, a number of example control laws will be analyzed.

a. Pure Rate Control Law

For a pure rate control law, consider

$$\left. \begin{aligned} \xi_x &= \frac{K_{1x}}{I_x} \Omega_x = \lambda k_{1x} \Omega_x \\ \xi_y &= \frac{K_{1y}}{I_y} \Omega_y = \lambda k_{1y} \Omega_y \end{aligned} \right\} \quad (216)$$

so that the moment equations yield

$$\left. \begin{aligned} \dot{\Omega}_x - \lambda k_{1x} \Omega_x + \left(\frac{\lambda_y I_y}{I_x} \right) \Omega_y &= f_x \\ \dot{\Omega}_y - \lambda k_{1y} \Omega_y - \left(\frac{\lambda_x I_x}{I_y} \right) \Omega_x &= f_y \end{aligned} \right\} \quad (217)$$

and

The Laplace formulation of the corresponding complex rate error is

$$\left[s^2 - \lambda(k_{1x} + k_{1y})s + \lambda^2(1 + k_{1x}k_{1y}) \right] \Omega_{xy}(s) = V(s) \quad (218)$$

where the transform of the effective forcing function is given by

$$\begin{aligned} V(s) \equiv V_x(s) + iV_y(s) &= \left\{ \left[(s - \lambda k_{1y}) \Omega_{xo} - \left(\frac{\lambda_y I_y}{I_x} \right) \Omega_{yo} \right] \right. \\ &+ \left. \left[(s - \lambda k_{1y}) f_x(s) - \left(\frac{\lambda_y I_y}{I_x} \right) f_y(s) \right] \right\} + i \left\{ \left[(s - \lambda k_{1x}) \Omega_{yo} \right. \right. \\ &+ \left. \left. \left(\frac{\lambda_x I_x}{I_y} \right) \Omega_{xo} \right] + \left[(s - \lambda k_{1x}) f_y(s) + \left(\frac{\lambda_x I_x}{I_y} \right) f_x(s) \right] \right\} \end{aligned} \quad (219)$$

The time solution of (218) consists of the sum of a general solution, for which $f_x(s)$ and $f_y(s)$ are set equal to zero in (219), and a particular solution of the complete equation (218), for which $f_x(s)$ and $f_y(s)$ are specified for the applied disturbances. The functions $f_x(t)$ and $f_y(t)$ are the explicit, continuous functions of time defined by (213) and (214), and do not contain the rate or attitude errors.

The particular solution of (218) is directly dependent on the disturbance under consideration, but characteristic trends for this solution can be indicated when the general solution is a damped vibration. Step functions in (213) and (214) will lead to constant residual rate and attitude errors; impulse functions and their derivatives will lead to damped transient rate and attitude errors which approach zero as time increases; and sinusoidal forcing functions will produce residual sinusoidal rate and attitude errors. The amplitude of these residual errors is reduced with an increase in the damping ratio.

The actual development of time histories for the various applied disturbances will not be attempted here. The primary tasks of the control system are the minimization of errors during a disturbance and the elimination of residual errors after removal of the disturbance. Both these tasks can be accomplished by the selection of stable gains that yield large damping ratios consistent with realistic control systems, and do not require the development of time solutions.

Stable gains are gains for which all roots in the general solution have negative real parts. The characteristic equation for this general solution is

$$s^2 - \lambda(k_{1x} + k_{1y})s + \lambda(1 + k_{1x}k_{1y}) = 0 \quad (220)$$

and stability of the complex rate error requires that

$$\left. \begin{array}{l} -\lambda k_{1y} > \lambda k_{1x} \\ k_{1x}k_{1y} > -1 \end{array} \right\} \quad (221)$$

and

One should note that (220) has the form

$$s^2 + 2r_D\omega_N s + \omega_N^2 = 0 \quad (222)$$

The damped natural frequency ω_N may be expressed as

$$\omega_N = |\lambda| \sqrt{1 + k_{1x}k_{1y}} \quad (223)$$

while the damping ratio r_D and time constant t_D are

$$r_D = -\left[\frac{k_{1x} + k_{1y}}{2 \sqrt{1 + k_{1x}k_{1y}}} \right] \text{sgn } \lambda \quad (224)$$

and

$$t_D \equiv \frac{1}{r_D\omega_N} = \frac{-2}{\lambda(k_{1x} + k_{1y})} \quad (225)$$

respectively.

Selection of the control gains is generally based on a desired time constant and damping ratio. For the present case, this yields the relations

$$k_{lx} = -\frac{1}{\lambda t_D} \left[1 \pm \sqrt{(\lambda t_D)^2 + \left(1 - \frac{1}{r_D^2}\right)} \right] \quad (226)$$

and

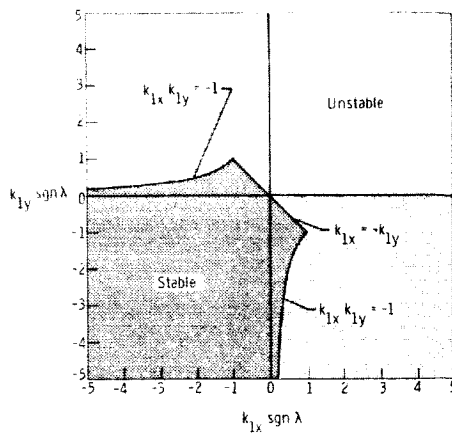
$$k_{ly} = -\frac{1}{\lambda t_D} \left[1 \mp \sqrt{(\lambda t_D)^2 + \left(1 - \frac{1}{r_D^2}\right)} \right] \quad (227)$$

where

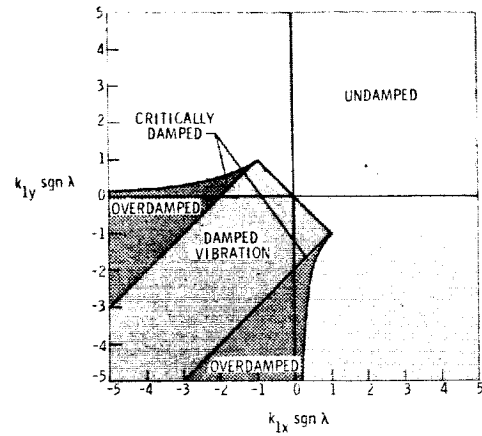
$$\frac{1}{r_D^2} \leq \left[1 + (\lambda t_D)^2 \right] \quad (228)$$

for the specified real values of k_{lx} and k_{ly} . The stability conditions (221) are automatically satisfied by (226) and (227) for positive real values of the damping ratio and time constant. Control gains for particular damping characteristics can thus be determined directly from the above equations.

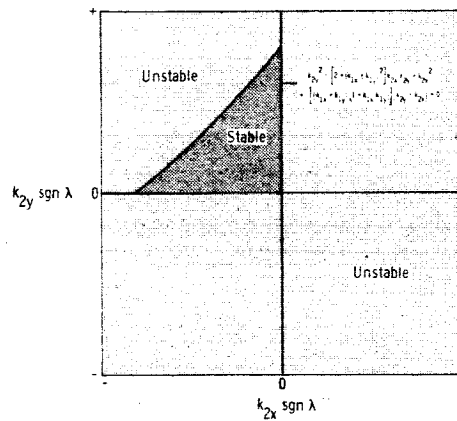
The resulting regions of stability for the control gain functions $k_{lx} \operatorname{sgn} \lambda$ and $k_{ly} \operatorname{sgn} \lambda$ are illustrated in figure 27(a). The gain functions must be in the area bounded above by the rectangular hyperbolas $k_{lx} k_{ly} = -1$ and the straight line $k_{lx} = -k_{ly}$. Of particular interest is the fact that either of the two gains can be zero. This means that damping of the spacecraft's rates is possible with torques applied about a single spacecraft axis and derived from a single rate gyro for that



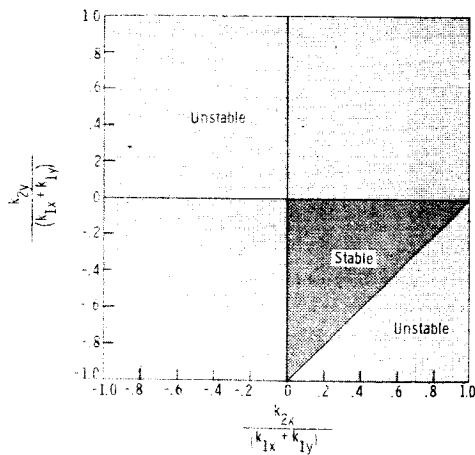
(a) Rate gains.



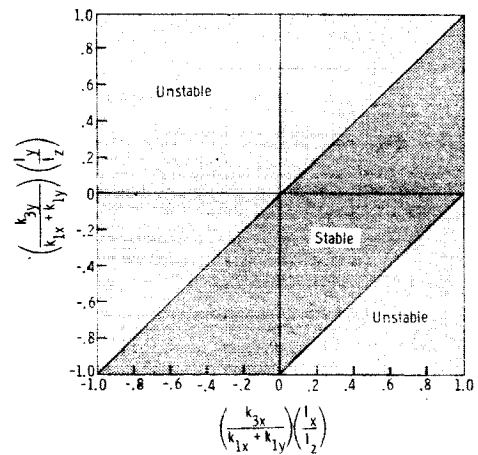
(b) Rate damping.



(c) Rate integral gains.



(d) Rate integral gains for small rate gains.



(e) Attitude gains for small rate and attitude gains.

Figure 27.- Stability characteristics for the controlled spacecraft.

axis. Hence, a control system providing rate control torques about two axes has inherent redundancy in case of failure of one of the system torquers.

An indication of the damping characteristics obtained for the pure rate control is given in figure 27(b). This figure shows the overdamped, critically damped, and damped vibration regions corresponding to the stable control gains. Critical damping occurs when $r_D = 1$, and yields the conditions

$$\text{and } \left. \begin{aligned} k_{1x} &= k_{1y} + 2 \\ k_{1x} &= k_{1y} - 2 \end{aligned} \right\} \quad (229)$$

from (224). Stable gains that fall outside of the straight lines defined by these conditions will yield overdamped spacecraft motion; gains that fall between the straight lines will yield vibrational, damped spacecraft motion.

From (224) and (225), it is apparent that the time constant is smallest when the two rate gains have the same sign. To optimize both the time constant and the damping ratio, one of the two gains can be selected as zero. Single-axis rate control for the spacecraft should thus be quite efficient.

The transformed complex position equation is

$$\begin{aligned} (s + i\sigma) \left[s^2 - \lambda(k_{1x} + k_{1y})s + \lambda^2(1 + k_{1x}k_{1y}) \right] \alpha(s) \\ = V(s) + \left[s^2 - \lambda(k_{1x} + k_{1y}) + \lambda^2(1 + k_{1x}k_{1y}) \right] \alpha_0 \end{aligned} \quad (230)$$

Since this equation contains a purely imaginary root, the solutions for the complex position error will be neutrally stable. The pure rate command is thus limited in its usefulness to those applications where only rate damping is needed. An example of such an application would be a manned space station, where the functions of rate damping and attitude control are often provided by different subsystems and where the rate control law is used to command onboard momentum storage system.

From (218), the rate error may be written as

$$\Omega_{xy} = \frac{e^{\frac{1}{2}(s_1+s_2)t}}{s_1 - s_2} \left\{ \left[\lambda(k_{1x} - k_{1y})\Omega_{x0} - \left(\frac{\lambda_y I_y}{I_x} \right) \Omega_{y0} \right] \sinh(s_1 - s_2)t + \left[\Omega_{x0}(s_1 - s_2) \right] \cosh(s_1 - s_2)t \right\} + i \left\{ \left[\lambda(k_{1y} - k_{1x})\Omega_{y0} + \left(\frac{\lambda_x I_x}{I_y} \right) \Omega_{x0} \right] \sinh(s_1 - s_2)t + \left[\Omega_{y0}(s_1 - s_2) \right] \cosh(s_1 - s_2)t \right\} + \int_{-\infty}^t \frac{\left\{ (s - \lambda k_{1y})f_s(s) - \left(\frac{\lambda_y I_y}{I_x} \right) f_y(s) + i \left[(s - \lambda k_{1x})f_y(s) + \left(\frac{\lambda_x I_x}{I_y} \right) f_x(s) \right] \right\}}{(s - s_1)(s - s_2)} ds \quad (231)$$

where

$$\left. \begin{aligned} s_1 &= \frac{\lambda}{2} \left[(k_{1x} + k_{1y}) + \sqrt{(k_{1x} - k_{1y})^2 - 4} \right] \\ s_2 &= \frac{\lambda}{2} \left[(k_{1x} + k_{1y}) - \sqrt{(k_{1x} - k_{1y})^2 - 4} \right] \end{aligned} \right\} \quad (232)$$

The response of the spacecraft is analogous to that of a spring-mass system with forced vibration and damping. The free vibration term corresponding to the initial conditions approaches zero as time increases, and the forced vibration term corresponding to the applied torque and mass motion effects is multiplied by a magnification factor or is damped to zero. The magnification factor is a function of the control gains and decreases as the terms k_{lx} and k_{ly} take on larger stable values. The attitude error for the pure rate control becomes

$$\begin{aligned} \alpha = \alpha_0 e^{-i\sigma t} - \frac{1}{(s_1 + i\lambda)(s_2 + i\lambda)} & \left\{ \left[\left[k_{lx} \Omega_{x0} + \left(\frac{\lambda_y I_y - \lambda I_x}{I_x} \right) \Omega_{y0} \right] \right. \right. \\ & + i \left[k_{lx} \Omega_{y0} - \left(\frac{\lambda_x I_x - \lambda I_y}{I_y} \right) \Omega_{x0} \right] \Big\} e^{-i\lambda t} + \frac{1}{s_1 - s_2} \left\{ \left[(s_1 - k_{ly}) \Omega_{x0} \right. \right. \\ & + \left(\frac{\lambda_y I_y}{I_x} \right) \Omega_{y0} \Big] + i \left[(s_1 - k_{lx}) \Omega_{y0} - \left(\frac{\lambda_x I_x}{I_y} \right) \Omega_{x0} \right] \Big\} e^{s_1 t} - \left\{ \left[(s_2 - k_{ly}) \Omega_{x0} \right. \right. \\ & + \left(\frac{\lambda_y I_y}{I_x} \right) \Omega_{y0} \Big] + i \left[(s_2 - k_{ly}) \Omega_{y0} - \left(\frac{\lambda_x I_x}{I_y} \right) \Omega_{x0} \right] \Big\} e^{s_2 t} \Big\} \\ & + \mathcal{L}^{-1} \left\{ \frac{\left[(s - k_{ly}) f_x(s) - \left(\frac{\lambda_y I_y}{I_x} \right) f_y(s) \right] + i \left[(s - k_{lx}) f_y(s) + \left(\frac{\lambda_x I_x}{I_y} \right) f_x(s) \right]}{(s - s_1)(s - s_2)(s + i\lambda)} \right\} \end{aligned} \quad (233)$$

where s_1 and s_2 are given by (232).

From inspection of (233), it is apparent that the initial errors α_0 and Ω_{xy0} contribute both free and damped vibration terms to the

spacecraft's motion. Since the damped terms will vanish for large time, only the purely oscillatory terms need be considered. The amplitude of the motion due to the initial position error α_0 is not affected by the pure rate control law, as one would expect from the results of the stability analysis. The amplitude of the motion resulting from initial rate errors can, however, be reduced by proper choice of the control gains for the particular spacecraft under investigation.

In summary, one may thus conclude that the pure rate control law is adequate for the damping of the spacecraft's angular velocities. If no initial attitude errors or reorientation requirements exist for the spacecraft, it should also be possible to select control gains which will hold the spacecraft to small oscillations about its initial position in the presence of crew motions and other internal disturbances. The latter function is particularly important in spacecraft with solar cell panels or similar equipment, which must be approximately maintained in a given inertial direction. The effectiveness of the attitude hold mode for the rate control law should, however, be checked by substitution of "worst case" forcing functions for the spacecraft into (233).

b. Rate Plus Rate Integral Control Law

When the control torque is derived from both rate gyros and integrating rate gyros, one may take

$$\left. \begin{aligned} g_x &= \frac{1}{I_x} \left(K_{1x} \Omega_x + K_{2x} \int^t \Omega_y dt \right) = \lambda \left[k_{1x} \Omega_x + k_{2x} \left(\frac{\lambda_y I_y}{I_x} \right) \int^t \Omega_y dt \right] \\ \text{and} \\ g_y &= \frac{1}{I_y} \left(K_{1y} \Omega_y + K_{2y} \int^t \Omega_x dt \right) = \lambda \left[k_{2x} \Omega_x + k_{2y} \left(\frac{\lambda_x I_x}{I_y} \right) \int^t \Omega_x dt \right] \end{aligned} \right\} (234)$$

with the governing equations

$$\left. \begin{aligned} \dot{\Omega}_x - \lambda k_{1x} \Omega_x + \left(\frac{\lambda_y I_y}{I_x} \right) \left[\Omega_y - \lambda k_{2x} \int^t \Omega_y dt \right] &= f_x \\ \dot{\Omega}_y - \lambda k_{1y} \Omega_y - \left(\frac{\lambda_x I_x}{I_y} \right) \left[\Omega_x + \lambda k_{2y} \int^t \Omega_x dt \right] &= f_y \end{aligned} \right\} \quad (235)$$

The characteristic equation for the general solution for the rate error is given by

$$s^4 - \lambda(k_{1x} + k_{1y})s^3 + \lambda^2(1 + k_{1x}k_{1y})s^2 + \lambda^3(k_{2y} - k_{2x})s - \lambda^4 k_{2x}k_{2y} = 0 \quad (236)$$

and the stability conditions are

$$\left. \begin{aligned} -\lambda k_{1y} &> \lambda k_{1x} \\ k_{1x}k_{1y} &> -1 \\ -k_{2x}k_{2y} &> 0 \\ \lambda k_{2y} &> \lambda k_{2x} \end{aligned} \right\} \quad (237)$$

and

$$\left. \begin{aligned} (k_{1x} + k_{1y})k_{2x}k_{2y} &> (k_{2y} - k_{2x}) \left[(k_{2y} - k_{2x}) \right. \\ &\quad \left. + (k_{1x} + k_{1y})(1 + k_{1x}k_{1y}) \right] \end{aligned} \right\}$$

Here, the nondimensional gains k_{jl} are defined as in (212).

The governing equation for the general solution for the position error yields the relation

$$\begin{aligned} & \left[s + i\sigma \right] \left[s^4 - \lambda(k_{1x} + k_{1y})s^3 + \lambda^2(1 + k_{1x}k_{1y})s^2 \right. \\ & \left. + \lambda^3(k_{2y} - k_{2x})s - \lambda^4 k_{2x}k_{2y} \right] \alpha(s) = 0 \end{aligned} \quad (238)$$

Once again, the attitude equation contains a purely imaginary root, leading to neutral stability of the position error. The trends of the spacecraft's motion for the rate plus rate integral control law are thus similar to those for the pure rate control law.

The stability regime for this control law is shown graphically in figures 27(a) and 27(c). The nondimensional gains k_{1x} , k_{1y} , k_{2x} , and k_{2y} must now be selected to satisfy the conditions (237). The first two of these conditions are identical to those for the pure rate control law and are given by figure 27(a). The next two conditions lead to stable motion in the second quadrant of figure 27(c), subject to the last restriction which represents a compatibility relation between the rate and rate integral gains. This compatibility condition yields a hyperbola with the equation

$$\begin{aligned} & k_{2y}^2 - \left[2 + (k_{1x} + k_{1y})^2 \right] k_{2x}k_{2y} + k_{2x}^2 \\ & + (k_{2y} - k_{2x}) \left[(k_{1x} + k_{1y})(1 + k_{1x}k_{1y}) \right] = 0 \end{aligned} \quad (239)$$

as sketched in figure 27(c). The stable region in this figure is then the area between the upper segment of the hyperbola and the $k_{2x} \operatorname{sgn} \lambda$ and $k_{2y} \operatorname{sgn} \lambda$ axes.

If the nondimensional rate gains are small in comparison with unity, as would be the case for most practical control systems, then (239) can be approximated by

$$(k_{1x} + k_{1y}) = (k_{2x} - k_{2y}) \quad (240)$$

and the resultant stability characteristics are given in figure 27(d). The spacecraft's motion is stable if the rate integral gains are selected from a triangular area of the fourth quadrant for a set of stable rate gains.

By examining (235) and (236), one notes that the modified characteristic equation for the rate error reduces to a cubic equation when either of the two rate integral gains vanishes. This special case would occur during single-axis control of the spacecraft and is thus of particular interest.

Stability restrictions are given by the standard rate gain restrictions and the relation

$$\left. \begin{array}{l} 0 > k_{2x} \operatorname{sgn} \lambda > (k_{1x} + k_{1y})(1 + k_{1x}k_{1y})\operatorname{sgn} \lambda \\ \text{or} \\ 0 > -k_{2y} \operatorname{sgn} \lambda > (k_{1x} + k_{1y})(1 + k_{1x}k_{1y})\operatorname{sgn} \lambda \end{array} \right\} \quad (241)$$

The resultant gains will fall on the boundary of the stable region in figures 27(c) and 27(d). Accordingly, stable control of the spacecraft is possible with single-axis rate plus rate integral commands.

Returning to the governing equations (235), one observes that numerical integration will be necessary to determine the rate time histories for particular values of the control gains. Some general conclusions can, however, be drawn for the case where the nondimensional rate gains are chosen to be considerably larger than the nondimensional rate integral gains. Inspection of (236) shows that the last two terms in this equation are now small during an initial transient period after a disturbance, when the rates are large and their integrals are small. The rate equation is thus approximately equal to (217) and the rate gains can be selected from (226) and (227) to yield the desired damping characteristics during the transient period. As steady state conditions are approached, the rate integral terms will predominate and the resultant control torques will tend to eliminate any residual rate errors. The net effect of this law will be a reduction in the gain magnitudes since the high rate error gains will no longer be needed to reduce standoff errors in the steady state condition. Damping and attitude hold characteristics for the rate plus rate integral law should thus be quite efficient.

c. Rate Plus Attitude Control Law

Next, consider control torques developed from both rate and attitude errors and given by

$$\left. \begin{aligned} g_x &= \frac{1}{I_x}(K_{1x}\dot{\theta}_x + K_{3x}\theta) = \lambda(k_{1x}\dot{\theta}_x + \sigma k_{3x}\theta) \\ g_y &= \frac{1}{I_y}(K_{1y}\dot{\theta}_y + K_{3y}\theta) = \lambda(k_{1y}\dot{\theta}_y + \sigma k_{3y}\theta) \end{aligned} \right\} \quad (242)$$

The resultant equations of motion are

$$\left. \begin{aligned} \dot{\Omega}_x - \lambda k_{1x} \Omega_x + \left(\frac{\lambda_y I_y}{I_x} \right) \Omega_y - \sigma \lambda k_{3x} \theta &= f_x \\ \dot{\Omega}_y - \lambda k_{1y} \Omega_y - \left(\frac{\lambda_x I_x}{I_y} \right) \Omega_x - \sigma \lambda k_{3y} \varphi &= f_y \end{aligned} \right\} \quad (243)$$

leading to the general characteristic equation for the complex rate error

$$\begin{aligned} s^4 - \lambda(k_{1x} + k_{1y})s^3 + \left[\sigma^2 + \lambda^2(1 + k_{1x}k_{1y}) \right] s^2 + \sigma \left[\left(\frac{k_{3y}^2 \lambda_x I_x}{I_y} - \frac{k_{3x}^2 \lambda_y I_y}{I_x} \right) - \right. \\ \left. \sigma \lambda(k_{1x} + k_{1y}) \right] s + \sigma^2 \lambda^2 [k_{1x}k_{1y} + k_{1x} - k_{1y}] = 0 \end{aligned} \quad (244)$$

The associated Hurwitz stability criteria yield the conditions

$$\left. \begin{aligned} -\lambda k_{1y} &> \lambda k_{1x} \\ k_{1x}k_{1y} &> -\left[1 + \left(\frac{\sigma}{\lambda} \right)^2 \right] \\ \left(\frac{k_{3y}^2 \lambda_x I_x}{I_y} - \frac{k_{3x}^2 \lambda_y I_y}{I_x} \right) &> \sigma \lambda(k_{1x} + k_{1y}) \\ \text{and} \quad \left(\frac{k_{3y}^2 \lambda_x I_x}{I_y} - \frac{k_{3x}^2 \lambda_y I_y}{I_x} \right) &> \frac{\lambda(k_{1x} + k_{1y})}{\sigma} \left\{ \left[\sigma^2 - \lambda^2(1 + k_{1x}k_{1y}) \right] \right. \\ &\quad \left. + \sqrt{\left[\sigma^2 - \lambda^2(1 + k_{1x}k_{1y}) \right]^2 + 4\sigma^2 \lambda^2(1 + k_{1y} - k_{1x})} \right\} \end{aligned} \right\} \quad (245)$$

for stability of the rate errors.

After substitution of (215) into (242), the characteristic equation associated with the general solution for the attitude error becomes

$$\begin{aligned} s^4 - \lambda(k_{1x} + k_{1y})s^3 + \left[\sigma^2 + \lambda^2(1 + k_{1x}k_{1y}) \right] s^2 \\ - \sigma^2 \lambda \left[(I_x + I_y - I_z) \left(\frac{k_{3y}}{I_x} - \frac{k_{3x}}{I_y} \right) + (k_{1x} + k_{1y}) \right] s \\ + \sigma^2 \lambda^2 \left[1 + (k_{1x} - k_{3x})(k_{1y} + k_{3y}) \right] = 0 \end{aligned} \quad (246)$$

Corresponding stability conditions are

$$\left. \begin{aligned} -\lambda k_{1y} &> \lambda k_{1x} \\ k_{1x}k_{1y} &> - \left[1 + \left(\frac{\sigma}{\lambda} \right)^2 \right] \\ \lambda \left(\frac{k_{3x}}{I_y} - \frac{k_{3y}}{I_x} \right) &> \left(\frac{k_{1x} + k_{1y}}{I_x + I_y - I_z} \right) \lambda \\ (k_{1x} - k_{3x})(k_{1y} + k_{3y}) &> -1 \end{aligned} \right\} \quad (247)$$

and

$$\begin{aligned} \lambda^2(k_{1x} + k_{1y})^2(k_{3x}k_{3y} - k_{1x}k_{3y} - k_{1y}k_{3x}) &> (I_x + I_y - I_z) \left(\frac{k_{3y}}{I_x} \right. \\ &\left. - \frac{k_{3x}}{I_y} \right) \left\{ \sigma^2(I_x + I_y - I_z) \left(\frac{k_{3y}}{I_x} - \frac{k_{3x}}{I_y} \right) + (k_{1x} + k_{1y}) \left[\sigma^2 - \lambda^2(1 + k_{1x}k_{1y}) \right] \right\} \end{aligned}$$

for the attitude errors.

Both (245) and (247) must hold for stable error histories. In most cases the nondimensional rate and attitude gains are small in comparison with unity, and the stability conditions given by these equations can be approximately represented by

$$\left. \begin{aligned} -\lambda k_{ly} &> \lambda k_{lx} \\ k_{lx} k_{ly} &> -1 \\ \text{and} \quad 0 &> \left[\left(\frac{k_{3x}}{k_{lx} + k_{ly}} \right) \left(\frac{I_x}{I_z} \right) - \left(\frac{k_{3y}}{k_{lx} + k_{ly}} \right) \left(\frac{I_y}{I_z} \right) \right] > 1 \end{aligned} \right\} \quad (248)$$

The rate gain restrictions are now identical to those for the pure rate law and are thus shown in figure 27(a). The attitude gain restrictions, illustrated in figure 27(e), yield a stable region falling between the lines

$$\left. \begin{aligned} \left(\frac{k_{3y}}{k_{lx} + k_{ly}} \right) \left(\frac{I_y}{I_z} \right) &= \left(\frac{k_{3x}}{k_{lx} + k_{ly}} \right) \left(\frac{I_x}{I_z} \right) \\ \text{and} \quad \left(\frac{k_{3y}}{k_{lx} + k_{ly}} \right) \left(\frac{I_y}{I_z} \right) &= \left(\frac{k_{3x}}{k_{lx} + k_{ly}} \right) \frac{I_x}{I_z} - 1 \end{aligned} \right\} \quad (249)$$

It is worthwhile to note that either of the two attitude gains may be zero, and attitude and rate damping of the spacecraft is thus possible with torques applied about a single spacecraft axis. The error signals needed in the calculation of these required torques can be taken from

a single rate gyro and a single sun sensor mounted on that axis, and the mechanization of such a control system appears to be very simple.

As seen from (244) and (246), the determination of the damped rate and attitude errors again requires the numerical integration of (243). One observes, however, that both damping and reorientation control can be provided by the rate plus attitude control law, and that this law can correspondingly be used to maneuver the spacecraft. In comparison, the rate and the rate plus rate integral control laws were restricted to holding an already established inertial position.

In addition, it may be noted that pure attitude control, for which $k_{1x} = k_{1y} = 0$, will result in several zero coefficients in (244) and (246). The associated spacecraft motion is, at best, neutrally damped and may diverge for certain forcing functions. Pure attitude control then provides no damping of the spacecraft rate and attitude errors. This conclusion is, of course, in agreement with previous results.

d. General Considerations

Other control laws may be investigated in an identical manner by selecting the control torques, developing the complex governing equations, and defining the resulting stability regions for the spacecraft's motion. If the control system gains are chosen to satisfy these criteria, the motion of the spacecraft will be damped. The determination of time histories of the controlled spacecraft motion becomes a rather tedious task, however, and is perhaps easiest if the governing equations (212) and (215) are programed on a digital or analog computer. Having assured

that the selected control gains lead to stable motion of the spacecraft, cases with particular disturbance functions can then be run on the computer to determine the spacecraft time histories.

Extension of the method to include nonlinear control commands is possible, but nonlinear techniques (refs. 21-27) must then be used to define the stability of the governing equations. A preliminary selection of the type of on-off control commands, as represented by step torques, may be made by noting that the spacecraft response for an amplitude-limited control system with high gains approaches that for an on-off control system. Sensor inputs and the signs of the control torques may thus be chosen from the proportional analysis. Time histories for the on-off commands can then be obtained by substitution of the corresponding step functions in (42). The solutions for the body rates and Euler angles now are found by a piecemeal process, and the forcing and solutions functions change whenever the deadbands for the on-off system are crossed,

Linear control optimization (ref. 28), as represented by a minimum mean square error criterion, may also be considered. Maximum torque or error limitations can be included as restraints in such an analysis.

4. Control System Selection

Having determined a control law which leads to acceptable damped motion of the spacecraft, one must next select physical systems that can develop the actuator-torque histories required by the control law. The choice of such control systems is generally made on a minimum-launch-weight basis; and relations between the control system weight and its impulse or momentum storage capacity are needed to evaluate the comparative merits of various control hardware. Preferably, these relations should not necessitate the detailed design and optimization of competitive systems for a particular spacecraft.

An empirical representation of the total control-system launch-weight in terms of the angular momentum or impulse provided by the system will be used in this analysis. Such a representation gives reasonable approximate values for the control system launch weight, and allows the rapid comparison of different control actuation schemes. Furthermore, the empirical results are completely independent of the spacecraft inertia characteristics or dynamics.

There remain then two tasks, namely sizing and implementation of the control system. To size the system, one first determines the spacecraft's angular momentum envelope by integration of the torques corresponding to simultaneous application of all "worst-case" disturbances. The launch weight for the control system can then be developed from the empirical data, and a preferred system concept can be selected. The implementation of this concept requires the solution of the control

system equations to define the actual torques the system must generate in order to provide the desired control law and eliminate cross coupling moments caused by any angular momentum stored in the control system.

Control system components may be divided into the general classes of momentum storage units and reaction control units. Momentum storage units comprise reaction wheels, single-gimbaled control moment gyroscopes, and double-gimbaled control moment gyroscopes. Reaction control units consist of reaction jets with variable mass flow or pulse modulation.

The angular momentum envelopes for these two classes of control components are then given by

$$\begin{aligned} H_M &\equiv H_{Mx} + iH_{My} \\ &= \left[I_x \int_0^{t_d} f_x dt \right] + i \left[I_y \int_0^{t_d} f_y dt \right] \end{aligned} \quad (250)$$

for the momentum storage units, and

$$\begin{aligned} H_R &= H_{Rx} + iH_{Ry} \\ &= \left[I_x \int_0^{t_d} |f_x| dt \right] + i \left[I_y \int_0^{t_d} |f_y| dt \right] \end{aligned} \quad (251)$$

for the reaction control units. The integration is carried on over t_d , the time interval of application of the "worst-case" disturbances.

a. Reaction Wheels

For sizing purposes the reaction wheel will be taken as a flywheel which is accelerated by means of a torque motor to produce reaction

torques on the spacecraft. A sketch of a control system using two such wheels is shown in figure 28.

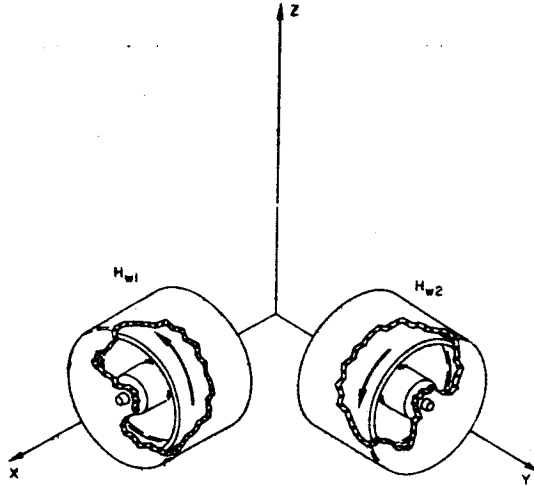


Figure 28.- Spacecraft control with reaction wheels.

From manufacturer's data*, the basic weight of a reaction wheel (ref. 29) with a minimum alternating-current motor configuration is

$$W_W = 6.3 + 170 \frac{H_W}{\omega_S} \quad (252)$$

where W_W is the total reaction wheel and motor weight in pounds, H_W is the angular momentum capacity in ft lb sec, and ω_S is the synchronous wheel speed in rad/sec.

Similarly, the reaction wheel power may be derived from empirical data (ref. 30) as

$$P_W = 2.77 G_S \omega_S \quad (253)$$

*Reproduced and used by courtesy of the Bendix Corporation.

where G_S is the stall torque in ft lb. If one introduces a power weight conversion factor of a lb/watt, then the equivalent power system weight for the reaction wheel is

$$W_P = 2.77 a G_S \omega_S \quad (254)$$

and the total weight chargeable to one reaction wheel becomes

$$W_{WT} = W_W + W_P = 6.3 + 170 \frac{H_W}{\omega_S} + 2.77 a G_S \omega_S \quad (255)$$

To optimize the total weight for a given angular momentum and stall torque, one differentiates the total weight with respect to wheel speed and equates the result to zero. Substitution of the corresponding wheel speed into (255) gives

$$W_{WT} = 6.3 + 21.7 \sqrt{a G_S H_W} \quad (256)$$

The control torques may be assumed to be sinusoidal with amplitude G_S and frequency λ , so that one can take

$$g = -G_S e^{i\lambda t} \quad (257)$$

as a good approximation to the control moments. Since these control moments are equal to the total rate of change of the angular momentum components for the reaction wheels, it follows that

$$\left. \begin{aligned} G_S \cos \lambda t &= \dot{H}_{W1} - \sigma H_{W2} \\ G_S \sin \lambda t &= \dot{H}_{W2} + \sigma H_{W1} \end{aligned} \right\} \quad (258)$$

or introducing

$$H_{xy} = H_{W1} + iH_{W2} \quad (259)$$

one obtains

$$G_S e^{i\lambda t} = \dot{H}_{xy} + i\sigma H_{xy} \quad (260)$$

This expression can be integrated to give

$$H_{xy} = \left(\frac{G_S}{\sigma + \lambda} \right) e^{i\lambda t} \quad (261)$$

for no initial wheel momentum. Maximization of (261) further yields the value

$$H_W = \frac{G_S}{\sigma + \lambda} \quad (262)$$

for each of the two reaction wheels.

Substitution of (262) into (256) leads to the expression

$$W_{WT} = 6.3 + \left[21.7 \sqrt{a(\sigma + \lambda)} \right] H_W \quad (263)$$

which is plotted in figure 29.

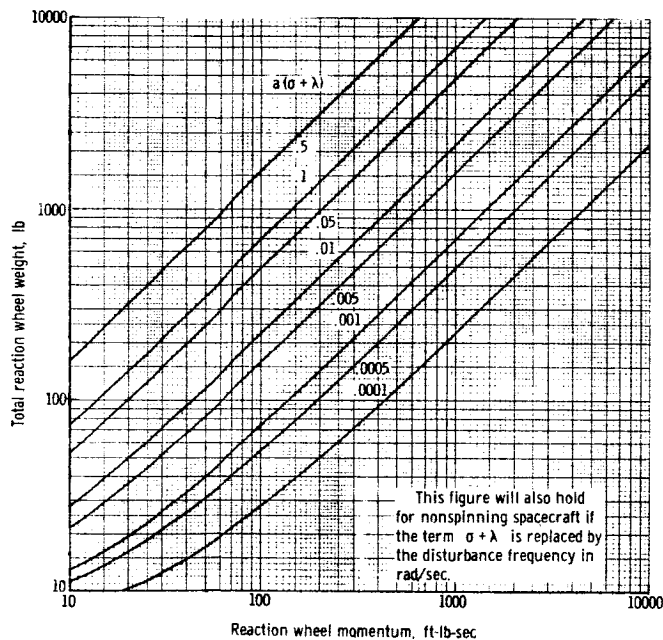


Figure 29.- Variation of total reaction wheel weight with required angular momentum.

The weight of the reaction wheel control system is now given by

$$W_T = W_{WT}(H_{Mx}) + W_{WT}(H_{My}) \quad (264)$$

where $W_{WT}(H_{Mx})$ and $W_{WT}(H_{My})$ are taken from the figure, using the values of H_{Mx} and H_{My} previously determined from (250).

One should note that the spin rate σ must be very small if reaction wheels are to be efficient. As an example, a power conversion factor of 1 lb/watt and a spin rate of 0.25 rad/sec for a flat disk configuration would yield $W_T = 3,074$ lb for an angular momentum requirement of 100 ft lb sec along each axis. Since such exorbitant weight penalties are impractical, reaction wheels generally are unacceptable for the damping control of spinning spacecraft.

If such wheels are used for spacecraft with very low spin rates, the governing torque relations become

$$g = -G = -\dot{H}_{xy} - i\sigma H_{xy} \quad (265)$$

and

$$T_z = \Omega_y H_x - \Omega_x H_y \quad (266)$$

where G is the complex torque applied to the reaction wheels, and T_z is the cross coupling torque applied to the spacecraft by the control system. Since the body rates are small, this sinusoidal cross coupling torque is relatively small and its effect on the spin rate σ will be neglected.

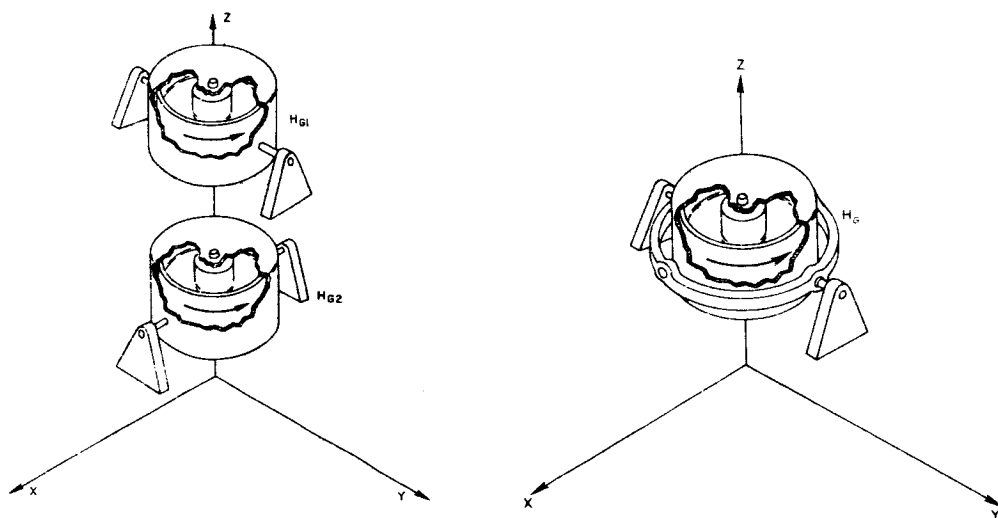
The desired control torques are then obtained by directly applying the reaction wheel torques

$$\mathbf{G} = \mathbf{G}_{W1} + i\mathbf{G}_{W2} = -\mathbf{g} \quad (267)$$

by means of the wheel actuators.

b. Control Moment Gyroscopes

A control moment gyroscope consists of a flywheel which spins at a constant speed and is mounted on a single or double gimbal arrangement. Control torques are now developed by precessing the flywheel. Torque actuators mounted on the gimbals provide the necessary precession torques. Sketches of control systems using single- and double-gimbaled gyros are given in figures 30(a) and 30(b), respectively.



(a) Single-gimbaled gyros.

(b) Double-gimbaled gyro.

Figure 30.- Spacecraft control with control moment gyros.

Since the weights of single- and double-gimbaled gyros do not differ appreciably, launch weights for both these units will be assumed to be identical. The basic weight of a control moment gyroscope can again be developed from manufacturer's data (ref. 31) and becomes

$$W_G = 1.37 H_G^{0.68} \quad (268)$$

Power requirements now are derived primarily from the windage and friction losses for the flywheel, and can be approximated by empirical data derived from computer analyses (ref. 32) as

$$W_P = 1.47 aH_G^{0.362} \quad (269)$$

The power required by the gimbal actuators is small and will be neglected. The total weight of the gyro is then

$$W_{GT} = W_G + W_P = 1.37 H_G^{0.68} + 1.47 aH_G^{0.362} \quad (270)$$

Launch weights of the gyro are plotted against angular momentum in figure 31, and a comparison with figure 29 shows that the total weight for a system using gyros is much less than that for a system using reaction wheels.

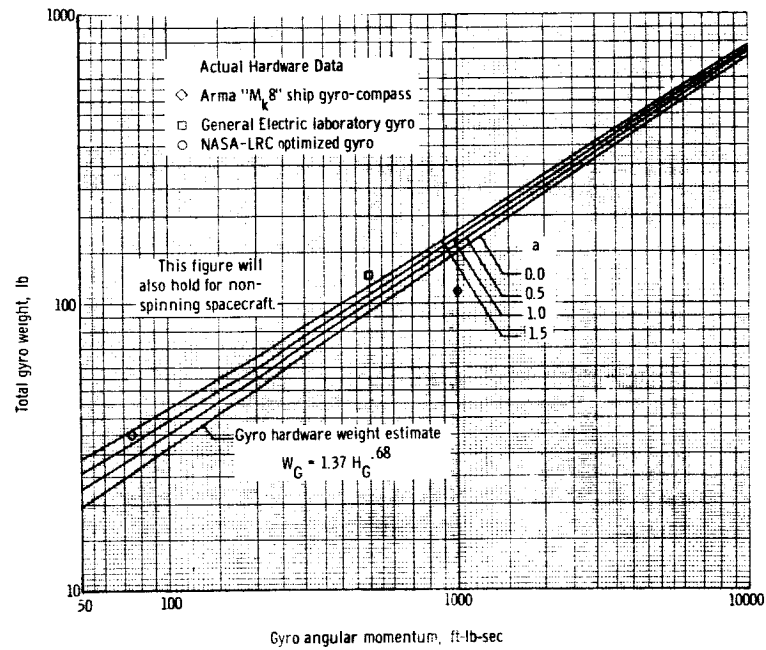


Figure 31.- Variation of total gyro weight with required angular momentum.

In comparing single- and double-gimbaled control moment gyros, one observes that the weight for the single-gimbaled gyro system is derived from

$$W_T = W_{GT}(H_{MX}) + W_{GT}(H_{MY}) \quad (271)$$

while the weight for the double-gimbaled gyro system becomes

$$W_T = W_{GT} \left(\frac{\sqrt{H_{MX}^2 + H_{MY}^2}}{\cos \alpha_g} \right) \quad (272)$$

where α_g is the limiting gimbal angle and H_{MX} and H_{MY} are again found from (250). Since α_g is generally 60° , the double-gimbaled gyro

system is somewhat lighter than a control system using two single-gimbaled gyros.

To derive the gimbal actuator commands for the implementation of the desired control laws, one notes that these torques are again derived from the total rate of change of the angular momentum vector for the gyro system. Thus, the complex control torque is

$$g = -G_{xy} = -\dot{H}_{xy} - i \left[\sigma H_{xy} - H_z \Omega_{xy} \right] \quad (273)$$

and the cross coupling moment becomes

$$T_z = -\dot{H}_z + \Omega_y H_x - \Omega_x H_y \quad (274)$$

The minor changes in the spin rate σ due to T_z will be neglected in this linear formulation, and the necessary control commands are now found by expressing H_{xy} and H_z in terms of the gimbal angles.

For the single-gimbaled gyros this gives

$$\left. \begin{aligned} H_{xy} &= H_x + iH_y = H_{G1} \sin \theta_g - iH_{G2} \sin \phi_g \\ H_z &= H_{G1} \cos \theta_g + H_{G2} \cos \phi_g \end{aligned} \right\} \quad (275)$$

The governing torque equations now reduce to

$$g = -G_{xy} = - \left\{ \left[H_{G1}(\dot{\theta}_g + \Omega_y) \cos \theta_g + H_{G2}(\sigma \sin \phi_g + \Omega_y \cos \phi_g) \right] + i \left[H_{G2}(\dot{\phi}_g - \Omega_x) \cos \phi_g + H_{G1}(\sigma \sin \theta_g - \Omega_x \cos \theta_g) \right] \right\} \quad (276)$$

and

$$T_z = H_{G1}(\dot{\theta}_g + \Omega_y) \sin \theta + H_{G2}(\dot{\phi}_g - \Omega_x) \sin \phi \quad (277)$$

where the small gimbal accelerations have been neglected. Gimbal torques may be commanded directly from

$$G_{xy} = G_x + iG_y = -g \quad (278)$$

in an open-loop system.

For the double-gimbaled gyro the angular momentum components along the spacecraft's axes become

$$H_{xy} = H_G(\sin \theta_g - i \sin \varphi_g \cos \theta_g) \quad (279)$$

and

$$H_z = H_G \cos \varphi_g \cos \theta_g$$

The torque relations thus are

$$\begin{aligned} g &= -G_{xy} = -(G_x + iG_y \cos \varphi_g) \\ &= -H_G \left\{ \left[\dot{\theta}_g + \sigma \sin \varphi_g + \Omega_y \cos \varphi_g \right] \cos \theta_g - i \left[(\dot{\varphi}_g + \Omega_x) \cos \theta_g \cos \varphi_g \right. \right. \\ &\quad \left. \left. - (\sigma + \dot{\theta}_g \sin \varphi_g) \sin \theta_g \right] \right\} \end{aligned} \quad (280)$$

and

$$\begin{aligned} T_z &= -G_y \sin \varphi_g = H_G \left\{ (\dot{\varphi}_g + \Omega_x) \sin \varphi_g \cos \theta_g \right. \\ &\quad \left. + (\Omega_y + \dot{\theta}_g \cos \varphi_g) \sin \theta_g \right\} \end{aligned} \quad (281)$$

where the gimbal acceleration terms are again neglected.

Necessary gimbal torques are developed from

$$\left. \begin{aligned} G_x &= -I_x \dot{\phi}_x \\ G_y &= -I_y \dot{\phi}_y \sec \phi_g \end{aligned} \right\} \quad (282)$$

and require the measurement of the gimbal angle ϕ_g .

c. Reaction Jets

The reaction jet system comprises the propellant, oxidizer, engines, and tankage weight necessary for the spacecraft's control. To arrive at weight estimates for such a system it was assumed that the usable specific impulse considering engine efficiency, expulsion efficiency, and ullage would be 290 lb_fsec/lbm and that the propellants would be storable hypergolics housed in tanks with positive feed expulsion diaphragms. Manufacturer's data* can then be extrapolated (ref. 33) to yield the idealized total system weight

$$W_T = 0.0101 I_T^{0.912} \quad (283)$$

which is presented in figure 32. Here I_T is the total impulse in lb sec. This impulse may be written in terms of the total momentum envelope for the spacecraft, giving

$$I_T = \left(\frac{H_{Rx}}{l_x} + \frac{H_{Ry}}{l_y} + \frac{H_{Rz}}{l_z} \right)_T \quad (284)$$

where l_x , l_y , and l_z are the moment arms about the X, Y, and Z body axes.

*Reproduced and used by courtesy of the Minneapolis-Honeywell Regulator Company.

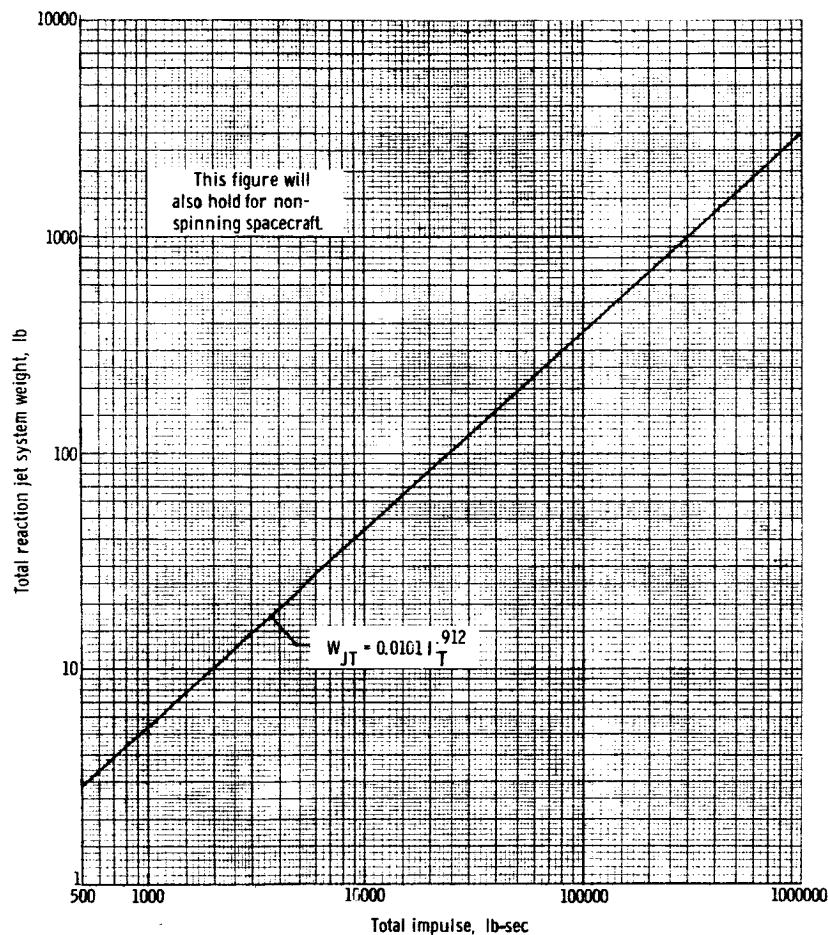


Figure 32.- Variation of total reaction jet system weight with required total impulse.

An assessment of the weight of the reaction jet system thus requires the development of total momentum envelopes for the spacecraft mission. The momentum for particular disturbances must be determined from (251) and the resulting momentum components along the spacecraft's axes must then be multiplied by the probable frequency of occurrence of each disturbance. By repeating this process for all disturbances and summing the individual momenta along each axis, a total momentum envelope per sampling period is obtained. The weight crossover time between

momentum storage and reaction control system can now be established from figure 32, since the total momentum envelope per unit time has been developed. If the mission time exceeds this crossover time, momentum storage systems should be selected for damping of the spacecraft's motion.

If reaction-jet systems are chosen, they can be combined with a mass-balancing system which compensates for any constant products of inertia resulting from crew motion or cargo transfer and eliminates limit cycling of the jets about the new principal moments of inertia. Such a system could, for example, pump the propellant to different positions within the spacecraft to obtain its control torques. Since the design of this mass-balancing system is very much dependent on the spacecraft geometry, it will not be considered here.

In most cases, however, the control system will consist of both reaction jets and momentum storage systems. The jets then provide for attitude control and orbit keeping and the momentum storage system is used to damp any oscillatory motion of the spacecraft. Attitude control commands are now used to actuate the reaction jets while rate and rate integral commands provide control laws for the momentum storage system. The development of such combined systems is again dependent on specific spacecraft and disturbances and will not be attempted in this analysis.

F. Comparison of Exact and Approximate Solution

Two possible manned spacecraft were considered for a comparison of the results of the numerical integration of the exact equations of motion

and the results of the present analytical solution. These spacecraft were a cylindrical manned orbital research laboratory and a large hexagonal space station.

1. Manned Orbital Research Laboratory - MORL

The MORL is proposed as an earth-orbital laboratory in which scientific and engineering experiments could be conducted over extended time periods. The basic laboratory is designed to support a crew of six astronauts in a 200-nautical-mile orbit for up to 5 years. During spinning operation, the laboratory module and the last stage of its Saturn booster would remain attached by a system of cables and would rotate about a common mass center. The resultant centrifugal force would produce an effective gravity field in the manned module. A sketch of the corresponding MORL configuration is shown in figure 33.

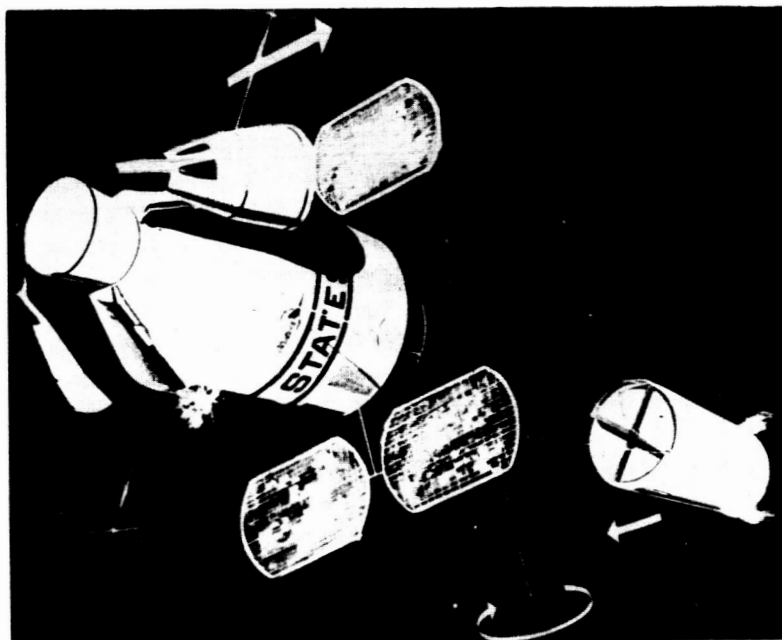


Figure 33.- Artist's sketch of possible manned orbital research laboratory.

Assumed inertia and mass characteristics (ref. 34) for this configuration are given in table 6. The inertia distribution is near-cylindrical, and the manned module and booster counterweight rotate about the Z axis at 0.4 rad/sec. A gravitational acceleration, equal to one-fourth that at the earth's surface, acts on the manned module due to this rotational rate.

The effects of various disturbances on MORL are summarized in table 7. The disturbances include residual rate and attitude errors after spinup, moments applied by an attitude control system valve failure in the open position, and several "worst-case" crew motions. These motions comprise step translation to an extreme position within the laboratory and linear oscillations which could result from trampoline exercise, ladder climbing, or floor pacing. A linear velocity of 4 ft/sec is selected for all oscillatory motions, and the entire crew of six is taken as a single equivalent mass with a mass factor Q of 36 slugs.

Equations defining these disturbances are listed in the second column of the table. The resulting error limits have been found by hand calculations of the analytical upper bounds and by extrapolation of the error time histories obtained from numerical integration of the exact equations of motion on an IBM 7094 computer.

Both rate and attitude error limits are given in the table. The rate error limits range from about 0.004 rad/sec for the step inertia product to about 0.025 rad/sec for the step torques, and the attitude error limits vary from approximately 0.01 rad/sec for the step inertia

product to approximately 0.18 rad/sec for the residual errors after spinup. Significantly, the errors caused by the periodic mass motions are several times greater than those produced by instantaneous motion to a final position. Predictions of maximum spacecraft errors due to crew motion must thus consider any periodic crew motions that may occur. Onboard experiments, which require high-accuracy control of the spacecraft, may be adversely affected by the oscillatory crew motions and may require restriction of these motions.

The approximate error limits developed from the analytical solutions show reasonable agreement with the maximum errors determined from the exact solutions. The deviations of the approximate error limits from the exact error limits are generally less than 20 percent of the exact error limits. These upper bounds of the spacecraft errors will thus give a conservative estimate of the effects of various disturbances and should be sufficient for initial engineering design applications.

About 3 hours of hand calculations were required for the determination of the approximate error limits, as compared with about 6 hours of data processing and computing for the calculation of the exact error limits. When one further considers the complexities associated with the programing and numerical integration of the exact equations of motion and the nonavailability of an IBM 709⁴ computer to many scientists, the advantages of the analytical results are apparent.

Two of the solutions described in table 7 have been selected for a comparison of the actual error histories and the error histories given by the analytical solution. The disturbances are the step product of

inertia and the vertical mass oscillation. Both the uncontrolled and the controlled spacecraft motions were considered. Solutions for the uncontrolled case were obtained from numerical integration of the exact equations of motion and from evaluation of the error relations developed in this analysis. Solutions for the controlled case were obtained from numerical integration of both the linearized and the exact equations of motion. All calculations were carried out on an IBM 709⁴ computer.

Single-axis control commands, which apply torques about the X or minimum-inertia axis of MORL, will be most efficient. One may accordingly set the nondimensional rate damping gain k_{1y} in (227) equal to zero. This yields

$$k_{1x} = -\frac{2}{\lambda t_D} = -2r_D \quad (285)$$

as the nondimensional rate damping gain for the X axis. The corresponding rate integral gain, when used, is arbitrarily selected as

$$k_{2x} = \frac{k_{1x}}{4}$$

to fall in the stable region of figure 27(d).

For MORL, the time constant t_D will be equated to one spin cycle or 20 sec. Values of the control constants are then

$$K_{1x} = -13,300$$

and

$$K_{2x} = -2,040$$

The rate damping ratio becomes

$$r_D = 0.1$$

and state-of-the-art gyros (ref. 35) in the 500 to 1000 ft-lb-sec class (see fig. 31) and jet hardware can provide the necessary control torques.

The MORL response to the step product of inertia is illustrated in figures 34 and 35. The uncontrolled rate and attitude errors are given in figure 34.

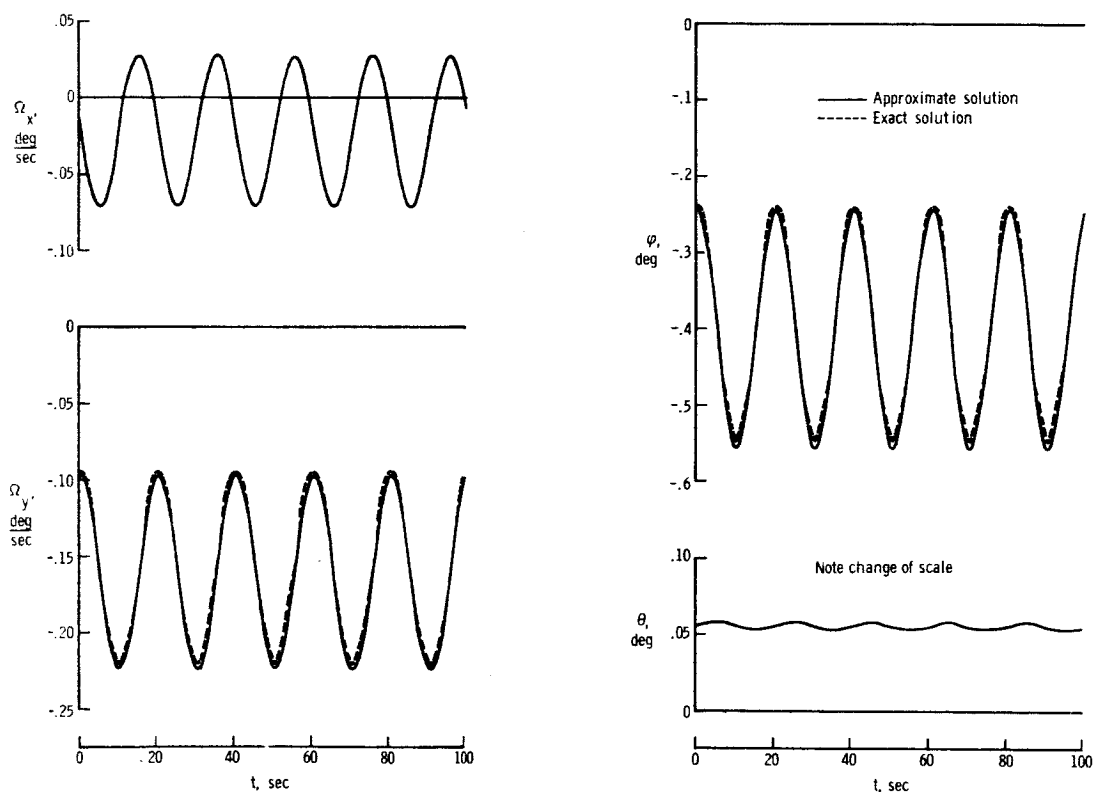


Figure 34.- Uncontrolled laboratory error histories for step inertia products.

It is apparent that the exact and approximate solutions are virtually identical. Both the rate and the attitude errors are biased sinusoids. As expected from the trace analysis, the largest rate error occurs about the Y axis and the largest attitude error corresponds to rotation about

the X axis (see figs. 9 and 10). To the crew, the rate error appears as a minute rolling motion of the laboratory floor with a maximum amplitude of 0.6° .

The controlled response of the laboratory to this disturbance is shown in figure 35.

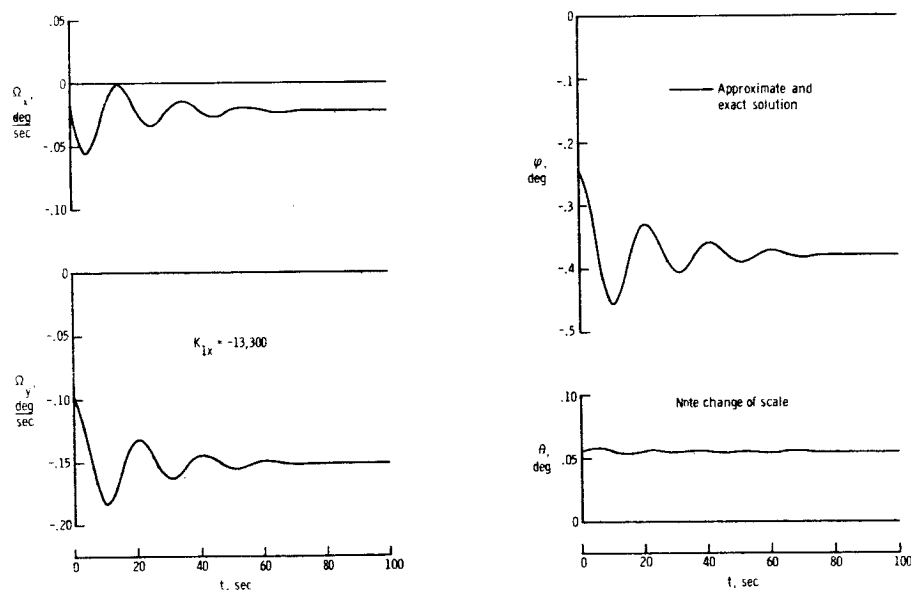


Figure 35.- Laboratory error histories for step inertia products and pure rate control.

This figure, which corresponds to pure rate control about the minimum inertia axis, again gives the same results for both the exact and the approximate solution. The laboratory oscillation is reduced to steady coning in about three spin cycles. The constant residual rate errors

produce constant control torques which counteract the mass unbalance torques produced by the products of inertia. The effective disturbance torque is thus less than it was for the uncontrolled case, and the residual rate errors are correspondingly somewhat smaller than the constant components of the uncontrolled rate errors. The oscillatory terms in the uncontrolled rate errors are due to the acceleration terms associated with the introduction of the inertia products and tend to zero in the controlled error histories.

The attitude errors for the damped rate errors become

$$\alpha_r = \varphi_r + i\theta_r = \alpha_0 e^{-i\sigma t} - \frac{i\Omega_{xyr}}{\sigma} \quad (286)$$

from (215). For the step products of inertia, the attitude errors result from changes in the body rates which do not affect the total spacecraft momentum. The contribution α_0 of the transient oscillatory terms in the body rates to the attitude errors will tend to zero, and residual attitude errors are given by

$$\left. \begin{aligned} \varphi_r &= \frac{\Omega_{yr}}{\sigma} \\ \text{and} \quad \theta_r &= -\frac{\Omega_{xr}}{\sigma} \end{aligned} \right\} \quad (287)$$

where Ω_{xr} and Ω_{yr} denote the residual body rates. Both the rate and attitude errors approach constant values for the theoretical solution.

As predicted by the analysis of the controlled spacecraft characteristics, single-axis rate control is acceptable for normal operation and experiments which do not require high-accuracy stabilization of the spacecraft.

The MORL response to a vertical periodic motion of the entire crew is depicted in figures 36 and 37. Figure 36 illustrates the uncontrolled results.

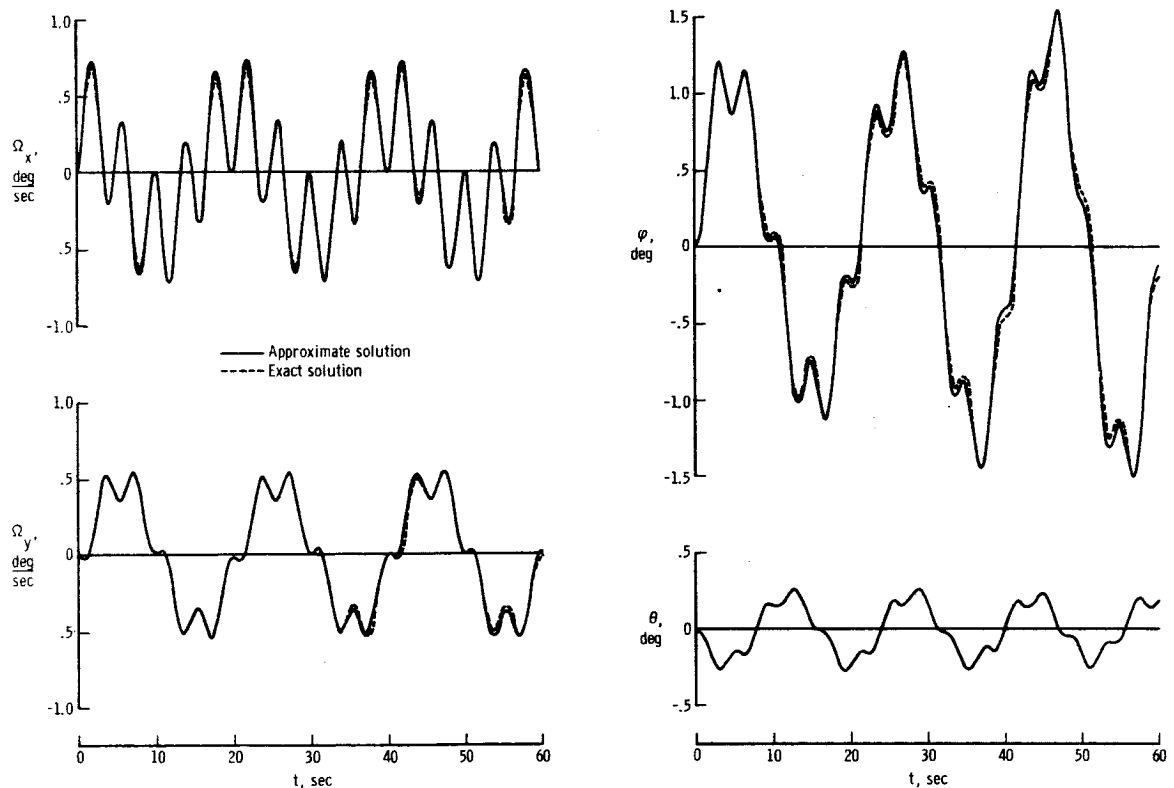


Figure 36.- Uncontrolled laboratory error histories for vertical mass oscillation.

The exact and approximate solutions check very closely. The rate and attitude errors now comprise a low-frequency, large-amplitude sinusoidal oscillation due to precession within the outer (λ) ellipses and high-frequency, small-amplitude oscillations due to precession within the inner (p) ellipses (see figs. 12 and 13). The maximum errors are two to three times as high as the corresponding errors for the step inertia.

product. The laboratory floor also undergoes irregular rolling motions with maximum amplitudes of about 2° . Since the distance (ref. 34) from the center of rotation to the laboratory floor is approximately 50 feet, this roll can produce a 2-foot total translation of the station floor and could present some difficulties to a moving astronaut within the laboratory.

The controlled laboratory motion is presented in figure 37.

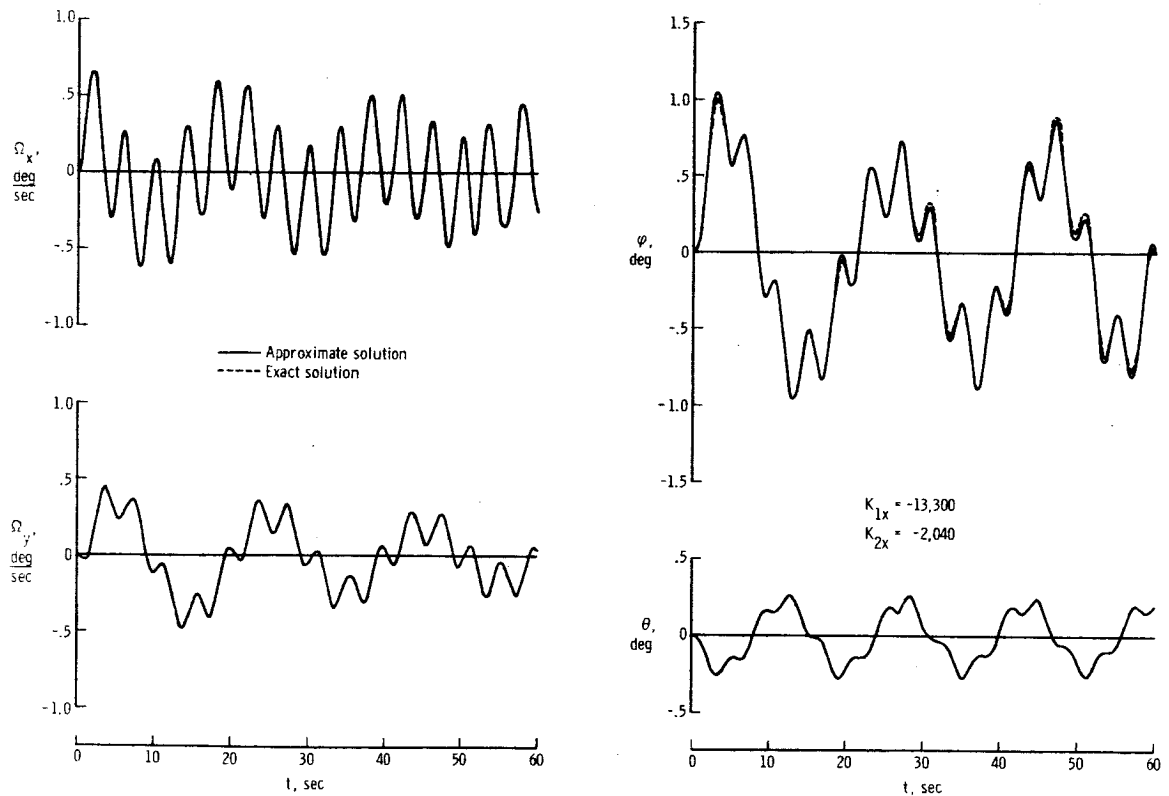


Figure 37.- Laboratory error histories for vertical mass oscillation and rate plus rate integral control.

Control torques are applied about a single axis, but a combined rate and rate integral control law is used. The laboratory motion is quite similar

to the uncontrolled motion, but exhibits damping of the free vibrations, as is apparent from the gradual decrease in the corresponding error terms. Since the periodic forcing function terms predominate, this type of response is to be expected. Agreement between the approximate and exact solutions is very good, and the small differences in the error histories can only be detected for the angle Φ .

The uncontrolled and controlled error histories developed from the approximate solution for the nonsymmetric MORL are practically coincident with the exact error histories for all the disturbances that have been examined. The analytical solution is thus a useful tool for the study of the nonsymmetric laboratory motion.

2. Large Manned Space Station

A second possible type of manned rotating spacecraft is the large spinning space station, such as the 150-foot station which will be considered here. This station (ref. 1), shown in figure 38, has six cylindrical outer modules arranged in the shape of a hexagon. The outer modules are connected to a central hub and docking port by three spokes. Rotation about the maximum inertia axis provides artificial gravity for the living modules. The crew of this space station would vary from 6 to 21 astronauts.

Assumed characteristics for the 150-foot space station are listed in table 8. The inertia distribution approaches that of a flat disk and the spin rate is 3 rpm. The crew is taken as six astronauts with an effective mass factor Q of about 36 slugs.

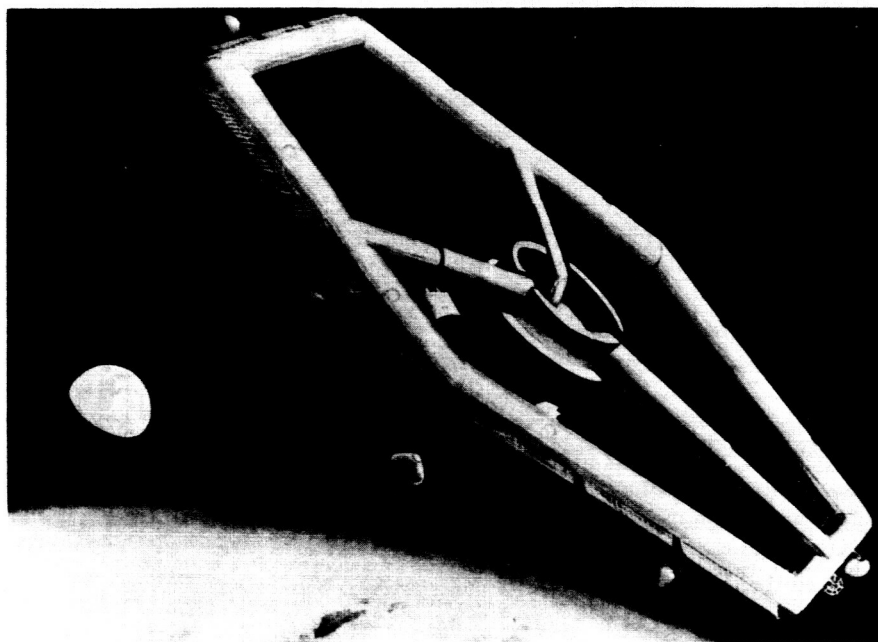


Figure 38.- Artist's sketch of possible 150-foot manned space station.

Disturbance effects on this station are summarized in table 9. The disturbances are similar to the MORL disturbances, and periodic crew motions are simulated by motion of a single equivalent mass with a linear velocity of 4 ft/sec. The rate error limits range from approximately 0.006 rad/sec for the step inertia products to approximately 0.015 rad/sec for the circumferential mass motion. The attitude error limits vary from about 0.017 rad/sec for the step inertia products to about 0.18 rad/sec for the residual errors. The errors due to periodic motions are considerably greater than those introduced by the step products of inertia.

Circumferential crew motions and the residual errors were chosen for a further comparison of the approximate and exact solutions. Both uncontrolled and controlled solutions were developed.

Control torques were now applied about both station axes and the corresponding control gains were assumed to be equal. Referring to (226) and (227), one notes that this yields

$$k_{1x} = k_{1y} = -\frac{1}{\lambda t_D} = -\left[\frac{1}{\sqrt{\frac{1}{r_D^2} - 1}} \right] \quad (288)$$

as the nondimensional damping gains. The corresponding rate integral and attitude gains, when used, are selected as

$$k_{2x} = -k_{2y} = \frac{k_{1x}}{4}$$

and

$$k_{3x} = -k_{3y} = k_{1x}$$

from the stable regions of figure 27(d) and 27(e). The physical control gains become

$$K_{1x} = K_{2x} = -222,817$$

$$K_{2x} = -K_{2y} = -75,000$$

and

$$K_{3x} = -K_{3y} = -70,000$$

from (210). A time constant of about three spin cycles or 54 sec was selected to give the damping ratio

$$r_D = 0.02$$

Higher values of damping would require exorbitant control moment gyro and reaction jet control systems. Even the selected value will require gyros in the 5,000 to 10,000 ft-lb-sec class and will exceed the present state-of-the-art in gyro hardware (see fig. 31). Rapid jet damping, although feasible, will result in large fuel consumption.

The advantages of single-axis control for nonsymmetric vehicles become obvious when one notes that the MORL, with about one-half the spin momentum of the 150-foot station, requires a control system that is an order of magnitude smaller. In addition, the MORL is able to achieve lower time constants and considerably better damping ratios. These results lead to the conclusion that nonsymmetric spacecraft, spinning about a maximum inertia axis, are preferable from the control standpoint and that single-axis stabilization about the minimum inertia axis can result in major control system weight savings for these spacecraft.

The 150-foot station motion for the circumferential mass transfer is given in figure 39. The approximate and exact solutions are in good agreement, and the time histories exhibit slow oscillations. These oscillations (see figs. 21 and 22) consist of a large-amplitude sinusoid with the mass motion frequency p and small-amplitude sinusoids with, approximately, the precession frequency λ . The angular deviation of the gravity vector has an amplitude of about 3° and appears as a corresponding slow rolling motion to the crew. For the 150-foot space station this rolling motion produces a 4-foot oscillation of the station floor.

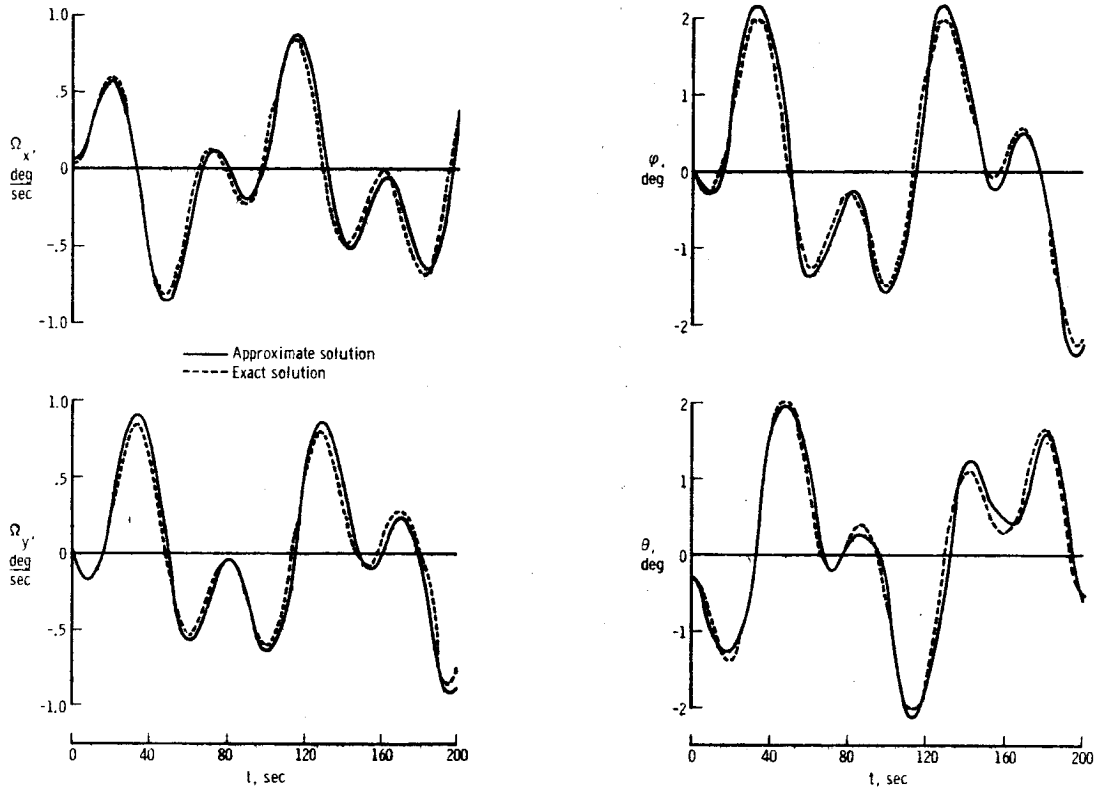


Figure 39.- Uncontrolled station error histories for circumferential mass motion.

The controlled station response is illustrated in figure 40. Control is derived from rate plus rate integral commands, and the station rates are damped to a purely sinusoidal trace in approximately nine spin cycles. The constant rate term in the damped trace will eventually disappear under the action of the rate integral commands. Residual rate errors may then be expressed as

$$\Omega_{xyr} = -\Omega_r e^{ipt} \quad (289)$$

where Ω_r denotes the half-amplitude of the residual rate. From (160), this residual rate amplitude term is

$$\Omega_r \approx \frac{I_{rz}(\sigma + p)^2}{I(\lambda - p)}$$

so that

$$\Omega_{xyr} \approx - \left[\frac{I_{rz}(\sigma + p)^2}{I(\lambda - p)} \right] e^{ipt}$$

The corresponding residual rate error becomes

$$\alpha_r \approx i \left[\frac{I_{rz}(\sigma + p)}{I(\lambda - p)} \right] e^{ipt}$$

and

$$\varphi_r = \left(\frac{\Omega_{yr}}{\sigma + p} \right) \approx - \left[\frac{I_{rz}(\sigma + p)}{I(\lambda - p)} \right] \sin pt$$

$$\theta_r = - \left(\frac{\Omega_{xr}}{\sigma + p} \right) \approx \left[\frac{I_{rz}(\sigma + p)}{I(\lambda - p)} \right] \cos pt$$

The residual terms correspond to the coefficients of e^{ipt} in the uncontrolled solution functions. The control system thus has to have little effect on the magnitude of the errors directly due to the constant circumferential mass motion as would be expected for the selected low value of the damping ratio. The approximate solution compares favorably with the exact solution for this example.

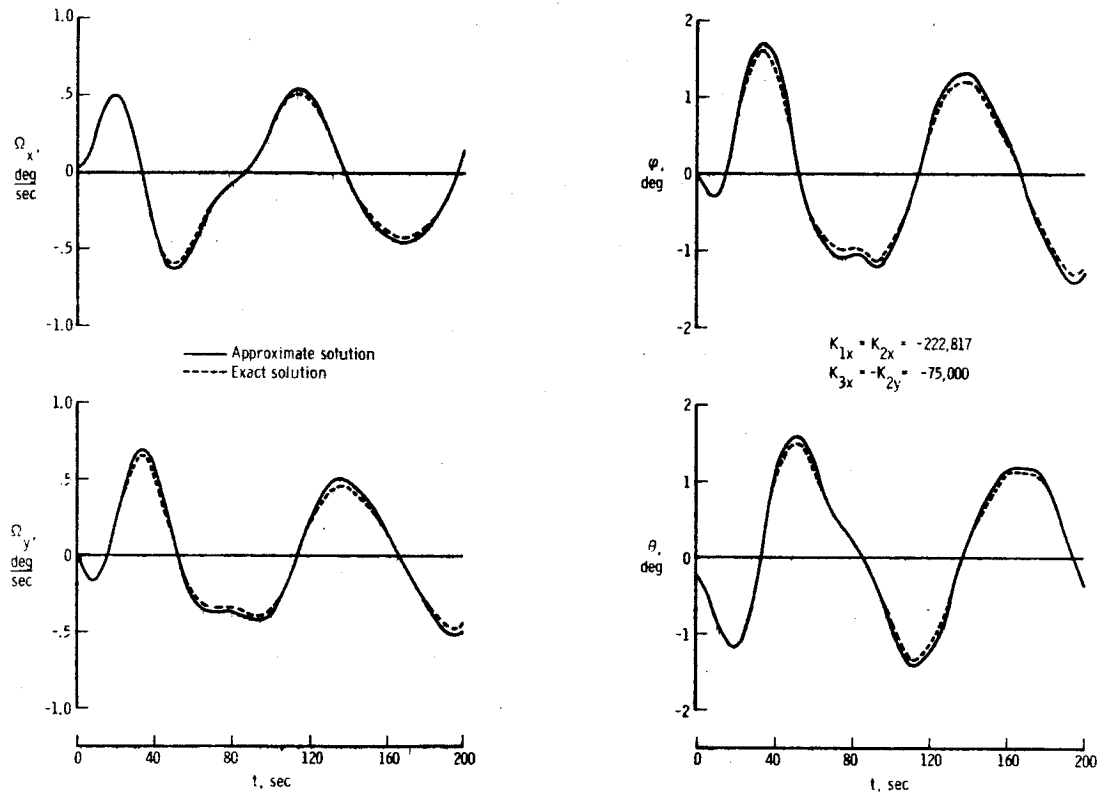


Figure 40.- Station error histories for circumferential mass motion and rate plus rate integral control.

Figure 41 presents the station response for residual rate and attitude errors. As anticipated from figure 15, the rate errors are simple sine and cosine curves. The attitude errors, following (133), are somewhat more complex sinusoids. The exact and approximate solutions checked to within three significant figures.

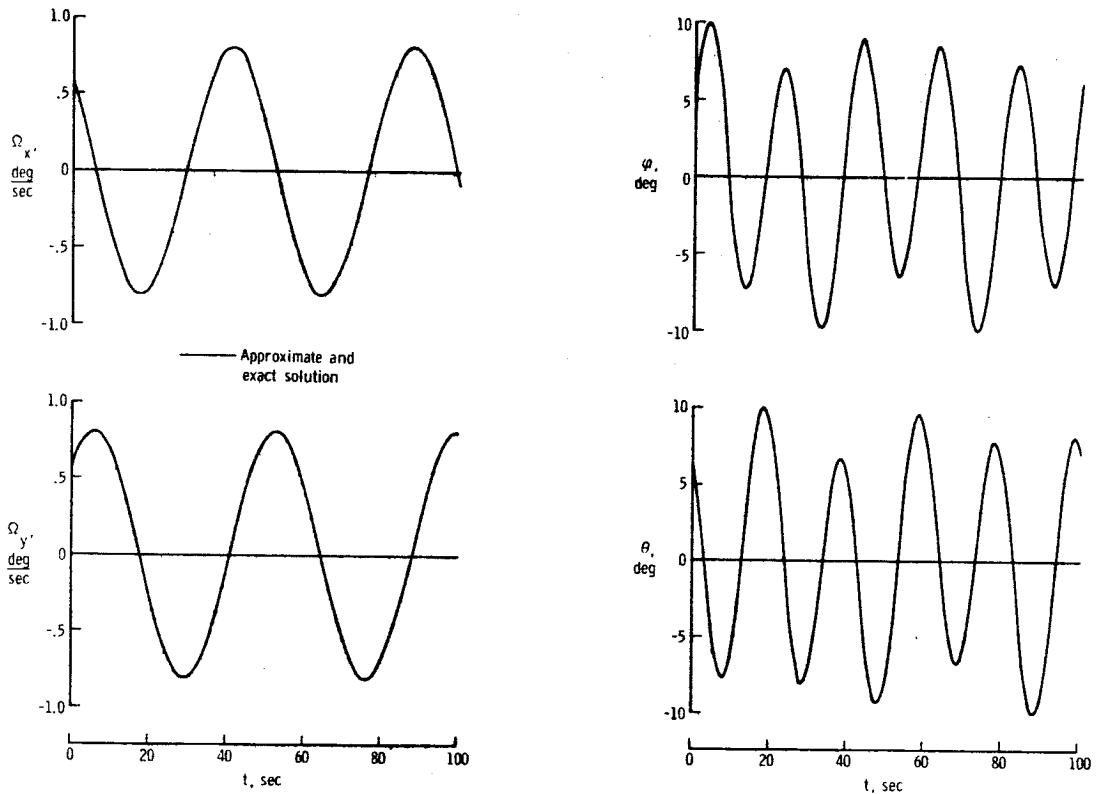


Figure 41.- Uncontrolled station error histories for residual errors.

The controlled station motion with the residual errors is shown in figure 42. Rate plus attitude control commands are now employed, and the spacecraft completes the required 10° reorientation about two axes in approximately 16 spin cycles. The analytical and exact solutions again were identical.

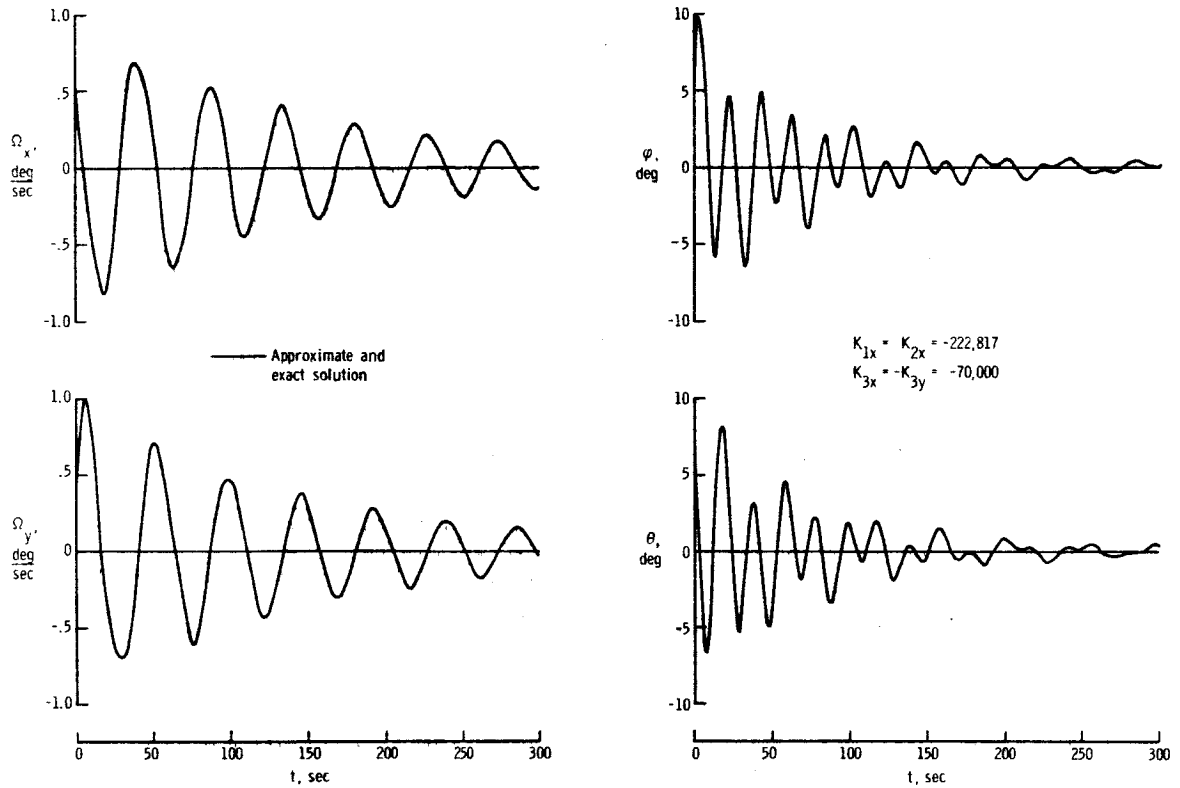


Figure 42.- Station error histories for residual errors and rate plus attitude control.

In summarizing the comparison, one may conclude that the analytical solution was in excellent agreement with the exact solution for all cases considered. Since the spacecraft used in the comparison are typical examples of future rotating manned spacecraft, the analytical solution should be valid for the determination of the dynamics and control of most such spacecraft. Analytical results for unmanned spacecraft, which may have larger torque disturbances and residual errors but have few or no inertia changes, should also be acceptable. The time history data

obtained for the step torques and residual errors were accurate to three places and an increase in these disturbances should not appreciably degrade the results in the linear range. The analytical solution thus offers a simpler, more economical, and more direct means of assessing the effects of various disturbances and spacecraft characteristics on the spacecraft motion than the computer runs. The insight into the mechanics of motion, that is gained from the error formulation developed in this analysis, should be of major value to future work on the dynamics of arbitrary rotating spacecraft.

IX. ANALYSIS OF SPINUP AND DESPIN MODE

A. Governing Equations

For the present application of the governing equations for the spinup and despin mode, the spacecraft disturbances are assumed to be restricted so that no internal mass movements occur and no moments are exerted about the spacecraft X and Y axes. This yields

$$\Omega_z = \frac{1}{I_z} \left[I_{z0} \Omega_{z0} + \int M_z dt \right] \quad (290)$$

and

$$\psi = I_{z0} \Omega_{z0} \int \frac{dt}{I_z} + \int \frac{1}{I_z} \left[\int M_z dt \right] dt \quad (291)$$

from (8) and (12).

Spinup and despin moments about the Z axis will be assumed to be provided by constant-thrust, pulse-modulated jets (refs. 1, 34, 36). Since the control of the spacecraft during this mode is quite straightforward, the main problem is the selection of a spinup and despin technique which minimizes the associated fuel consumption for rigid and extensible spacecraft.

B. Rigid Spacecraft

For the rigid spacecraft configurations, such as the large hexagonal space station, the jet moment arms remain constant. Spinup and despin fuel is thus given by

$$W_{SU} = \frac{M_z t_f}{l_{zf} I_{SP}} = \frac{I_{zf} \Omega_{zf}}{l_{zf} I_{SP}} \quad (292)$$

where the subscript f denotes conditions after completion of the spinup maneuver. The simplest spinup technique would apply continuous thrust or constant-width thrust pulses until the desired spin rate Ω_{zf} is reached.

C. Extensible Spacecraft

1. Mathematical Model

For extensible spacecraft configurations, such as the MORL, the fuel calculation becomes somewhat more difficult. As an example, consider the sketch below.

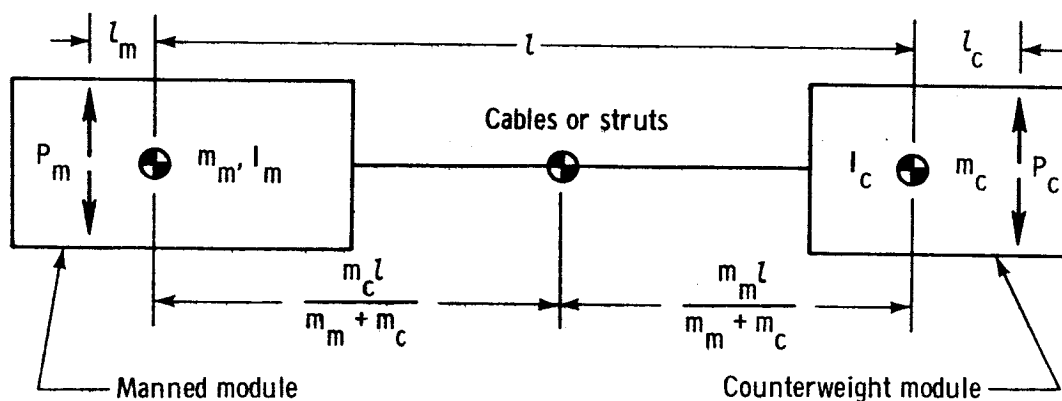


Figure 43.- Mathematical model for spinup fuel calculations.

Here the spacecraft consists of a manned module with mass m_m and a counterweight module with mass m_c . The two modules are connected by a flexible cable or strut arrangement, which is extended to produce a large rotational radius. The distance between the module mass centers is designated l ; the offset distance between the thrust P_m and the manned module mass center is l_m ; and the offset distance between the thrust P_c and the counterweight module mass center is l_c . These

offset distances yield a larger moment arm and may be required to maintain the spinup thrust line normal to the line connecting the mass centers. To minimize oscillations of the manned module about its Z axis, some type of rate damping should also be provided. Rate damping moments can be supplied by a small reaction wheel or passive dampers. The individual module oscillations about their respective mass centers will, however, be neglected for the spinup fuel calculations.

Spinup thrusts may be produced by jets on the manned module, by jets on the counterweight module, or by jets on both modules. The first method is preferable when the counterweight module mass exceeds the manned module mass, and the second method is preferable when the manned module mass exceeds the counterweight module mass. The third method may be used if jets are mounted on both the manned and counterweight module; a pure couple about the spacecraft mass center can now be produced by selecting

$$\left. \begin{aligned} P_c &= \left(\frac{m_c}{m_m} \right) P_m \\ \text{and} \\ l_c &= \left(\frac{m_m}{m_c} \right) l_m \end{aligned} \right\} \quad (293)$$

Spinup thrusts would be simultaneously applied to both modules for this method.

All three of the thrusting methods lead to effective moment and moment arm relations of the form

236
236
472

and

$$\left. \begin{aligned} l_z &= D_1 l + D_2 \\ M_z &= D_3 l_z \end{aligned} \right\} \quad (294)$$

where

$$\left. \begin{aligned} D_1 &= \frac{P_m m_c + P_c m_m}{(P_m + P_c)(m_m + m_c)} \\ D_2 &= \frac{P_m l_m + P_c l_c}{P_m + P_c} \\ D_3 &= P_m + P_c \end{aligned} \right\} \quad (295)$$

and

for the spacecraft model.

The spin inertia I_z can be written as

$$I_z = I_o + D_4 l_z + D_5 l_z^2$$

where

$$\left. \begin{aligned} I_o &= I_m + I_c + \left(\frac{m_c m_m}{m_m + m_c} \right) \left(\frac{D_2}{D_1} \right)^2 \\ D_4 &= \left(\frac{2m_c m_m}{m_m + m_c} \right) \left(\frac{D_2}{D_1^2} \right) \\ D_5 &= \left(\frac{m_c m_m}{m_m + m_c} \right) \left(\frac{1}{D_1^2} \right) \end{aligned} \right\} \quad (297)$$

and I_m , I_c denote the respective module inertias referred to the module mass centers.

The above equations now allow the simple formulation of the total fuel consumptions for different spinup techniques.

2. Spinup and Despin Techniques

Spinup will be assumed to occur in the following manner. While rigidly coupled, the two modules are brought to an angular rate Ω_{zi} . The modules are then separated by extending the flexible module connector under action of the centrifugal force. During this extension process the spacecraft momentum, spin-rate, or spinup thrust may be held constant. After the full cable extension is reached, the two modules are spun up to the final spacecraft spin speed. Despin will require this sequence in reverse order.

The fuel required for spinup or despin can be expressed as

$$\begin{aligned}
 W_{SU} &= \frac{1}{I_{SP}} \int_0^{t_f} \left(\frac{M_z}{l_z} \right) dt \\
 &= \frac{1}{I_{SP}} \left[\frac{I_{zi} \Omega_{zi}}{l_{zi}} + \int_{t_i}^{t_e} \left(\frac{I_z \dot{\Omega}_z + \dot{I}_z \Omega_z}{l_z} \right) dt + \frac{I_{zf} (\Omega_{zf} - \Omega_{ze})}{l_{zf}} \right] \\
 &= \frac{1}{I_{SP}} \left[\frac{I_{zf} \Omega_{zf}}{l_{zf}} + \int_{l_{zi}}^{l_{zf}} \left(\frac{I_z \Omega_z}{l_z^2} \right) dl_z \right] \quad (298)
 \end{aligned}$$

where the subscript i denotes conditions after the initial spinup to Ω_{zi} ; the subscript e denotes conditions after the extension; and the subscript f again denotes final conditions.

Three characteristic spinup techniques will be considered here. These involve extension with constant momentum $I_{zi} \Omega_{zi}$, constant spin rate Ω_{zi} , and continuous thrust.

a. Constant-Momentum Extension

Perhaps the simplest spinup technique is one where no spinup thrust is applied during the extension. The modules are allowed to separate as desired while the spin speed automatically decreases to maintain the angular momentum constant. After achievement of the desired extension the spinup jets are again actuated.

The fuel consumption now becomes

$$W_{SU} = \frac{I_{zf}\Omega_{zf}}{l_{zf}ISP} \left[1 + \left(\frac{I_{zi}\Omega_{zi}}{I_{zf}\Omega_{zf}} \right) \left(\frac{l_{zf}}{l_{zi}} - 1 \right) \right] \quad (299)$$

from (298). The rate of cable (or strut) extension does not effect this fuel consumption and may be varied arbitrarily to maintain the cables in tension during the extension. The fuel consumption is minimized by selecting the smallest value of Ω_{zi} which will yield sufficient cable tension at the completion of the extension.

b. Constant-Rate Extension

For this spinup technique, the spacecraft spin speed is maintained at its initial value Ω_{zi} throughout the extension. The modules are again allowed to separate until the final extension is reached, and the spacecraft is then brought to its final spin speed Ω_{zf} .

The fuel consumptions relation (298) reduces to

$$W_{SU} = \frac{I_{zf}\Omega_{zf}}{l_{zf}ISP} \left\{ 1 + \left(\frac{l_{zf}}{I_{zf}} \right) \left(\frac{\Omega_{zi}}{\Omega_{zf}} \right) \left[I_0 \left(\frac{l_{zf} - l_{zi}}{l_{zi}l_{zf}} \right) - D_4 \ln \left(\frac{l_{zf}}{l_{zi}} \right) + D_5 (l_{zf} - l_{zi}) \right] \right\} \quad (300)$$

for this case. Fuel consumption now is minimized by selecting the smallest value of Ω_{zi} which will yield sufficient cable tension at the beginning of the extension.

The spinup thrust for the constant-rate extension is established by the requirement that the rate of change of angular velocity due to operation of the thruster must be greater than that due to the rate of extension or retraction. When the extension rate is maintained at a constant value \dot{l}_z , this condition can be expressed as

$$D_3 \geq \Omega_{zi} \dot{l}_z \left[2D_5 - \frac{D_4}{l_{zi}} \right] \quad (301)$$

The minimum thrust is thus directly dependent on the product of the extension rate and the initial spin rate. Corresponding conditions for variable extension rates may be developed from (290), if the time variation of l_z is known.

c. Continuous-Thrust Extension

Another possible spinup technique would involve continuous thrusting during the spinup. This brute-force technique will require rapid extension of the cable modules to be efficient, but will be simpler to implement than the constant-rate extension.

The associated fuel consumption is given by

$$W_{SU} = \frac{D_3 t_f}{I_{SP}} = \frac{I_{zf} \Omega_{zf}}{l_{zf} I_{SP}} \left\{ 1 - \left(\frac{\Omega_{ze}}{\Omega_{zf}} \right) + \left(\frac{I_{zi}}{I_{zf}} \right) \left(\frac{l_{zf}}{l_{zi}} \right) \left(\frac{\Omega_{zi}}{\Omega_{zf}} \right) + \left(\frac{l_{zf} D_3}{I_{zf} \Omega_{zf}} \right) (t_e - t_1) \right\} \quad (302)$$

To evaluate (302), a time history for either Ω_z or l_z during the extension must be selected. Values of Ω_{ze} and t_e can then be developed from this time history and (290), if one recalls that $l_z = l_{zf}$ and $\Omega_z = \Omega_{ze}$ when $t = t_e$.

If the extension rate \dot{l}_z is constant, then

$$\left. \begin{aligned} \Omega_{ze} &= \frac{1}{I_{zf}} \left[I_{zi} \Omega_{zi} + D_3 l_{zi} (t_e - t_i) + \frac{D_3 \dot{l}_z}{2} (t_e - t_i)^2 \right] \\ \text{and} \\ t_e - t_i &= \frac{l_{zf} - l_{zi}}{\dot{l}_z} \end{aligned} \right\} \quad (303)$$

Substitution of (303) into (302) now yields

$$W_{SU} = \frac{I_{zf} \Omega_{zf}}{l_{zf} I_{SP}} \left\{ 1 + \left(\frac{l_{zf} - l_{zi}}{I_{zf} \Omega_{zf}} \right) \left[\frac{I_{zi} \Omega_{zi}}{l_{zi}} + \frac{D_3 (l_{zf} - l_{zi})}{2 \dot{l}_z} \right] \right\} \quad (304)$$

and fuel consumption is optimized by selecting the smallest value of Ω_{zi} and the largest value of \dot{l}_z which will avoid cable slacking during the extension.

d. Comparison of Extension Techniques

To compare the different extension techniques, note that the fuel consumption for each technique is expressed as the ideal fuel consumption at full extension plus an incremental fuel consumption for the extension process. From the ratio of these incremental fuel consumptions for (299) and (300), it follows that

$$\left[\frac{(\Omega_{zi})_{CM}}{(\Omega_{zi})_{CR,CT}} - 1 \right] \left(\frac{I_{zi}}{D_5 l_{zi}^2} \right) = \left(\frac{l_{zf}}{l_{zi}} - 1 \right) + 2 \left(\frac{D_2}{l_{zi}} \right) \left[1 + \frac{\ln \left(\frac{l_{zi}}{l_{zf}} \right)}{1 - \left(\frac{l_{zi}}{l_{zf}} \right)} \right] \quad (305)$$

is the condition corresponding to equality of the constant-rate and constant-momentum fuel consumption. Similarly the relation

$$\left[\frac{(\Omega_{zi})_{CM}}{(\Omega_{zi})_{CR,CT}} - 1 \right] \left(\frac{I_{zi}}{D_5 l_{zi}^2} \right) = \frac{1}{2} \left[\frac{D_3}{D_5 l_z (\Omega_{zi})_{CR,CT}} \right] \left(\frac{l_{zf}}{l_{zi}} - 1 \right) \quad (306)$$

must hold for equality of the constant-rate and constant-momentum fuel consumption.

The initial spin rates $(\Omega_{zi})_{CT}$ and $(\Omega_{zi})_{CR}$ for the constant-thrust and constant-rate extensions should produce equal centrifugal forces to start the extension and are both assumed to be equal to the value $(\Omega_{zi})_{CR,CT}$. The spin rate $(\Omega_{zi})_{CM}$ for the constant-momentum extension is greater than or equal to $(\Omega_{zi})_{CR,CT}$.

The equations (305) and (306) are represented graphically in figure 44. This figure allows the direct selection of the most economical spinup technique for a particular spacecraft as a function of an extension length ratio $\frac{l_{zi}}{l_{zf}}$, a moment arm ratio $\frac{D_2}{l_{zi}}$, a thrust ratio

$\left[\frac{D_3}{D_5 l_z (\Omega_{zi})_{CR,CT}} \right]$, and a momentum ratio $\left[\frac{(\Omega_{zi})_{CM}}{(\Omega_{zi})_{CR,CT}} - 1 \right] \left(\frac{I_{zi}}{D_5 l_{zi}^2} \right)$. To

make use of the figure, one first selects the extension parameters

D_2 , D_3 , l_z , $(\Omega_{zi})_{CR,CT}$, and $(\Omega_{zi})_{CM}$. The selected parameters and the initial spacecraft characteristics determine values for the moment arm ratio, the thrust ratio, and the momentum ratio.

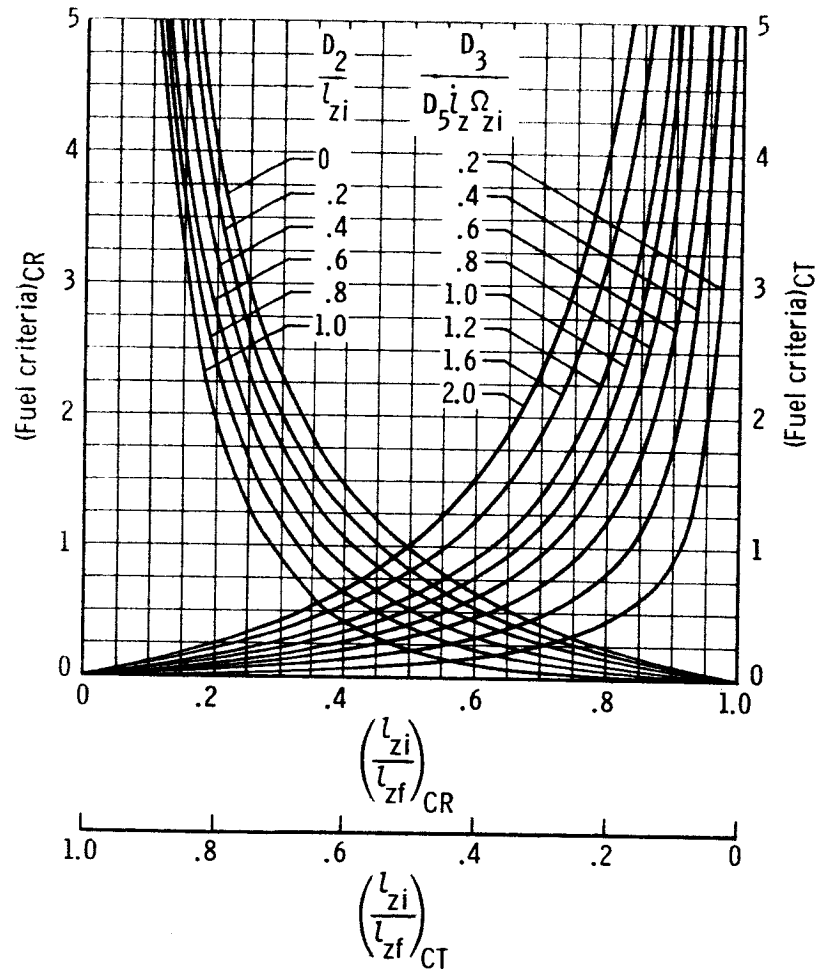


Figure 44.- Fuel criteria for extension technique selection.

For a particular value of the extension length ratio, the moment arm ratio locates a fuel criteria point corresponding to the constant-rate extension and the thrust ratio locates a fuel criteria point corresponding to the continuous-thrust extension. The momentum ratio gives a third fuel criteria point for the constant-momentum extension on the ordinate. The lowest of the three fuel criteria values indicates the technique which will yield the lowest fuel consumption.

The special case, where the minimum centrifugal force for all three techniques is equal, is of interest since the minimum cable tension will usually determine the extension parameters. For this case, one has

$$\frac{(\Omega_{zi})_{CM}}{(\Omega_{zi})_{CR,CT}} = \left(\frac{I_{zf}}{I_{zi}} \right) \sqrt{\frac{\frac{l_{zi}}{l_{zf}} - \frac{D_2}{l_{zf}}}{1 - \frac{D_2}{l_{zf}}}} \quad (307)$$

for the constant-momentum extension and

$$D_3 \geq \left[I_{zf} \sqrt{\frac{\frac{l_{zi}}{l_{zf}} - \frac{D_2}{l_{zf}}}{1 - \frac{D_2}{l_{zf}}}} - I_{zi} \right] \left[\frac{2\dot{l}_z(\Omega_{zi})_{CR,CT}}{l_{zf}^2 - l_{zi}^2} \right] \quad (308)$$

for the continuous-thrust extension.

From (307) and (308), one may write

$$\frac{\text{Constant-momentum fuel criteria}}{\text{Continuous-thrust fuel criteria}} = 1 + \frac{l_{zf}}{l_{zi}} \quad (309)$$

and the continuous-thrust extension is now always more economical than the constant-momentum extension. Only the constant-rate extension and the continuous-thrust extension need to be compared for this case.

As an example, consider the Manned Orbital Research Laboratory described in table 6. The assumed extension parameters for this spacecraft are

$$l_1 = 37.5 \text{ ft}$$

$$l_f = 137.5 \text{ ft}$$

$$(\Omega_{zi})_{CR,CT} = 0.1 \text{ rad/sec}$$

$$\Omega_{zf} = 0.4 \text{ rad/sec}$$

$$D_3 = P_m = 100 \text{ lb}$$

$$D_2 = l_m = 4 \text{ ft}$$

and a spinup technique which will yield the lowest fuel consumption is desired. The cable tension must be greater than or equal to its initial value during the extension and the spinup time is immaterial.

Since the minimum centrifugal force must be equal for all three techniques, the constant-momentum extension may be disregarded. From the given extension parameters and (301) and (308), one has

$$(i_z)_{CT} = 0.252 \text{ ft/sec}$$

and

$$(i_z)_{CR} = 0.172 \text{ ft/sec}$$

as the respective maximum extension rates for the continuous-thrust and constant-rate spinups.

The extension ratios now are

$$\frac{l_{zi}}{l_{zf}} = 0.334$$

$$\frac{D_2}{l_{zi}} = 0.254$$

and

$$\left[\frac{D_3}{D_5(i_z)_{CT}(\Omega_{zi})_{CR,CT}} \right] = 1.02$$

By referring to figure 44, one notes that

$$(\text{Fuel criteria})_{CT} = 1.0$$

$$(\text{Fuel criteria})_{CR} = 1.6$$

Since the fuel criterion for the continuous-thrust extension is considerably lower than that for the constant-rate extension, it follows that the continuous-thrust spinup technique will require the least spinup fuel for this example.

The actual fuel consumption values for the example, as computed from (299), (300), and (304) for a specific impulse of 290 lbf sec/lbm, are

$$W_{CT} = 245 \text{ lb}$$

$$W_{CR} = 256 \text{ lb}$$

$$W_{CM} = 276 \text{ lb}$$

The continuous-thrust spinup requires approximately 12 percent more fuel than the ideal spinup at full extension and the constant-momentum and constant-rate spinups require approximately 26 percent and 17 percent more fuel than the ideal value of 219 pounds. A saving of about 22 pounds of fuel can thus be realized for each spinup and despin cycle by selection of an optimum spinup technique for this example.

If desired, the response of the spacecraft to internal mass movements and external disturbance torques may be included in the analysis of the spinup and despin mode by using (8) and (12) as the governing equations of motion. Supplementary linearized equations of motions for the relative module oscillations can be incorporated in such an analysis.

X. CONCLUSIONS

An approximate solution of the equations of motion of arbitrary rotating spacecraft with variable disturbance functions has been developed on the basis of small changes in the spacecraft body rates, Euler angles, and inertia terms. Complex representations have been used to define spacecraft and rate errors induced by the disturbance functions, and the solutions for the time history components and total error vectors have been examined for both uncontrolled and controlled spacecraft.

The results of this analysis have led to the following conclusions:

A. A comparison of the present analytical solution and solutions obtained by numerical integration of the exact equations of motion for two typical manned spacecraft has shown that the analytical solution is in excellent agreement with the exact solution for the small angle and rate regime. The analytical solution provides a simpler, more economical, and more direct method of assessing the effects of various disturbances and spacecraft characteristics on the spacecraft motion and allows an insight into the mechanics of motion which cannot be derived from the numerical solution.

B. Analytical upper limits of the rate and attitude errors induced by various disturbances are in reasonable agreement with the maximum errors found by interpolation of the numerical data. These upper limits should suffice for first estimates of the effect of the disturbances on the spacecraft motion.

C. The spacecraft inertia distribution was found to have a significant effect on the spacecraft motion for equal disturbance

characteristics. Spacecraft, whose inertia distribution approached that of a flat disk, exhibit considerably more inherent stability than slender, near-cylindrical spacecraft spinning about a maximum or minimum axis of inertia. However, for most practical cases the disturbance characteristics are directly related to the inertia distribution, so that the error bounds for spacecraft with different inertia distributions will tend to be similar.

D. Periodic mass motions within the spacecraft may result in rate and attitude errors, which are several times greater than those predicted for worst-case step products of inertia. For equal disturbance characteristics, the largest errors resulted from circumferential mass motion in the direction of spin. Respectively, smaller errors were produced by radial mass oscillations in an offset spin plane and vertical mass oscillations parallel to the spin axis. Motions of the crew such as trampoline exercise, ladder climbing, or periodic translations along the spacecraft floor should be carefully examined to determine their impact on the spacecraft motion.

E. The spacecraft errors indicated instability trends, when the spin axis became an intermediate axis of inertia during a mass motion and when the periodic motions took place with the precession frequency λ . Mass motions falling in these two categories should be avoided.

F. An investigation of possible control techniques revealed that pure rate control and rate plus rate integral control would provide adequate damping of the spacecraft errors induced by internal disturbances. Initial attitude errors and attitude errors induced by external

disturbances cannot be eliminated by these control techniques and will require rate plus attitude control.

G. Single-axis control was found to be acceptable for all control techniques and allows major reductions in the control gains and control system weight for near-cylindrical configurations spinning about a maximum axis of inertia.

H. Optimization of the spinup and extension technique for cable- or strut-connected spacecraft modules can lead to appreciable fuel savings for the extension and retraction process. Comparison of continuous thrust, constant rate, and constant-momentum extensions for an example spacecraft indicated that 22 lbs or 5 percent of the ideal spinup and despin fuel could be saved by use of a continuous-thrust extension technique.

XI. ACKNOWLEDGMENTS

The author would like to express his gratitude to Dr. James B. Eades of the Virginia Polytechnic Institute for serving as his committee chairman and for his many valuable suggestions.

Thanks are also due to the National Aeronautics and Space Administration for permitting this work to be carried out, and to East Stenographic Section personnel for their valuable assistance in typing the rough and final dissertation drafts.

XII. BIBLIOGRAPHY

1. Kurzahls, P. R.: Stability and Control for the Manned Orbital Laboratory. Paper presented at the Thirteenth Meeting of the SAE A-18 Committee on Flight Controls, December 1963.
2. Space Technology Laboratories: Manned Mars Landing and Return Missions. Technical Report No. TR-2572-6911-RU000, 1964.
3. Kurzahls, P. R.; and Adams, J. J.: Dynamics and Stabilization of the Rotating Space Station. Astronautics, vol. 7, no. 9, Sept. 1962.
4. Kurzahls, P. R.; and Keckler, C. R.: Spin Dynamics of Manned Space Stations. NASA TR R-155, 1963.
5. Leon, H. T.: Spin Dynamics of Rockets and Space Vehicles in a Vacuum. STL TR-59-0000-00787, 1959.
6. Thomson, W. T.: Introduction to Space Dynamics. John Wiley and Sons, Inc., 1961.
7. Thomson, W. T.; and Fung, Y. C.: On the Stability of Spinning Space Stations Due to Crew Motion. STL Report EM-14-11, 2521-6003-RU000, 1964.
8. Hackler, C. T.: Some Considerations of the Stabilization and Control of a Rotating Space Station Based on a Linear Analysis. NASA Proposed TN, 1964.
9. Buglia, J. J.; Young, G. R.; Timmons, J. D.; and Brinkworth, H. S.: Analytical Method of Approximating the Motion of a Spinning Vehicle With Variable Mass and Inertia Properties Acted Upon by Several Disturbing Parameters. NASA TR R-110, 1961.
10. Loebel, M.: Progress Report, Manned Orbital Space Station Technical Summary. North American Aviation Report SID 63-36-1, 1963. (Confidential)
11. Routh, E. J.: Advanced Dynamics of Rigid Bodies. Dover Publications, Inc., 1955.
12. MacMillian, W. D.: Dynamics of Rigid Bodies. Dover Publications, Inc., 1960.
13. Whitbeck, R. F.: A Phase Plane Method for Finding the Exact Solutions for the Motion of a Freely Spinning Unsymmetrical Rigid Body With Arbitrary Initial Conditions. Paper presented at the Fourteenth Meeting of the SAE A-18 Committee on Flight Controls, July 1964.

14. Suddath, J. H.: A Theoretical Study of the Angular Motions of Spinning Bodies in Space. NASA TR R-83, 1961.
15. Charters, A. C.: The Linearized Equations of Motion Underlying the Dynamic Stability of Aircraft, Spinning Projectiles, and Symmetrical Missiles. NACA TN 3350, January 1955.
16. Kuebler, Manfred E.: Gyroscopic Motion of an Unsymmetrical Satellite Under No External Forces. NASA TN D-596, December 1960.
17. Grubin, Carl: Dynamics of a Vehicle Containing Moving Parts. The Journal of Applied Mechanics, September 1962.
18. Tai, C. L.; Andrew, L. V.; Loh, M. M. H.; and Kamrath, P. C.: Transient Dynamic Response of Orbiting Space Stations. AF Report No. FDL-TDR-64-25, February 1965.
19. Piland, William M.: An Analytical and Experimental Investigation of the Motion of a Rotating Space Station. NASA TN D-2981, September 1965.
20. Poli, Corrado R.: A Study of the Effects of Man's Motion on the Attitude and Orbital Motion of a Satellite. AF Report No. SEG-TR-65-41, 1965.
21. Stoker, J. J.: Nonlinear Vibrations. Interscience Publishers, Inc., 1950.
22. Minorsky, N.: Introduction to Non-Linear Mechanics. J. W. Edwards, 1947.
23. Kryloff, N.; and Bogoliuboff, N.: Introduction to Nonlinear Mechanics. Princeton University Press, 1943.
24. Andronow, A. A.; and Chaikin, C. E.: Theory of Oscillations. Princeton University Press, 1949.
25. Hurwitz, A.: On the Conditions Under Which an Equation Has Only Roots With Negative Real Parts. Mathematische Annalen, vol. 46, 1895, pp. 273-284.
26. Abzug, M. J.: On the Stability of a Class of Discontinuous Attitude Control Systems. AIAA Journal, vol. 1, no. 8, August 1963.
27. Gaylord, R. A.; and Keller, W. N.: Attitude Control System Using Logically Controlled Pulses, Guidance and Control. Edited by R. E. Roberson and J. S. Farrior, Academic Press, 1962.
28. Brown, B. M.: The Mathematical Theory of Linear Systems. John Wiley and Sons, Inc., 1961.

29. Bendix Eclipse-Pioneer Division: Reaction Wheels for Space Vehicles. Report AP 380, September 1963.
30. Minneapolis-Honeywell Regulator Company: Final Report for MORL Stabilization and Control, Phase I. Report No. R-ED 9317, September 1963.
31. The Boeing Company: Manned Orbital Research Laboratory System, Volume V, Subsystem Design. Report No. D2-22473-5, September 1963.
32. Garrett AiResearch Manufacturing Division: Control Moment Gyroscope Optimization Study. Report No. F-8036, January 1965.
33. Minneapolis-Honeywell Regulator Company: Reaction Control Propulsion for Space Vehicles. Report No. R-ED 17015, 1962.
34. Sperry Rand Systems Group: Space Station Stabilization and Control Study. Report No. AB-1210-0020, December 1963.
35. Bendix Eclipse-Pioneer Division: Control Moment Gyroscope, Design Report. November 1965.
36. Kurzahls, Peter R.: MORL Control System Integration. Paper presented at the Fourteenth Meeting of the SAE A-18 Committee on Flight Controls, July 1964.
37. Den Hartog, T. P.: Mechanical Vibrations. McGraw-Hill Book Company, Inc., 1940.
38. Churchill, R. V.: Operational Mathematics. McGraw-Hill Book Company, Inc., 1958.
39. Carslaw, H. S.; and Jaeger, J. C.: Operational Methods in Applied Mathematics. Oxford University Press, 1941.
40. Vanderpol, B.; and Bremmer, H.: Operational Calculus. Cambridge University Press, 1950.
41. Swerdtfeger, H.: Geometry of Complex Numbers. University of Toronto Press, 1962.
42. Zwicker, C.: The Advanced Geometry of Plane Curves and Their Applications. Dover Publications, Inc., 1963.
43. Hoffman, C. H.: How to Check Linear System Stability. Control Engineering, vol. 12, no. 2, February 1965.
44. Bellman, R.; and Kalaba, R.: Selected Papers on Mathematical Trends in Control Theory. Dover Publications, 1964.

45. Bohn, E. V.: The Transform Analysis of Linear Systems. Addison-Wesley Publishing Co., 1963.
46. Pungar, V.: Euler's Moment Equations for a Variable-Mass Unsymmetrical Top. IAS Journal, vol. 2, no. 5, May 1964.

XIII. VITA

The author was born in Berlin, Germany, on August 20, 1937. He graduated from Hampton High School in Hampton, Virginia, in 1955 and subsequently entered the Cooperative Engineering Program at the Virginia Polytechnic Institute. He received the degree of Bachelor of Science in Aeronautical Engineering in 1960 and was employed by the Langley Research Center of the National Aeronautics and Space Administration after graduation.

In 1961 he returned to the Virginia Polytechnic Institute under the NASA Graduate Study Program, and received the degree of Master of Science in Aerospace Engineering in 1962. Since 1962, he has continued his graduate work and has carried on research on the stability and control of manned spacecraft.

XIV. APPENDIX A

DEVELOPMENT OF THE LINEARIZED EQUATIONS OF MOTION

The rotating spacecraft will be considered as the system of particles shown in figure 1. A set of $X Y Z$ axes fixed to the spacecraft is used to describe the rotational motion of the spacecraft with respect to a set of $X_I Y_I Z_I$ axes which translate without rotation in inertial space and which remain parallel to a set of $X_F Y_F Z_F$ axes fixed in inertial space. The general moment equation (ref. 6) about the origin of the $X Y Z$ coordinate system is then

$$\vec{M} = \sum \vec{r}_j \times \frac{d}{dt} (m_j \vec{R}_j) \quad (A-1)$$

It will be assumed that the system mass does not change during the time periods of interest so that

$$\vec{M} = \sum \vec{r}_j \times m_j \vec{R}_j \quad (A-2)$$

The absolute vector acceleration \vec{R}_j is given by

$$\vec{R}_j = \vec{R}_0 + \vec{r}_j + \vec{\Omega} \times \vec{r}_j + 2\vec{\Omega} \times \vec{r}_j + \vec{\Omega} \times (\vec{\Omega} \times \vec{r}_j) \quad (A-3)$$

and substitution of (A-3) in (A-2) yields

$$\begin{aligned} \vec{M} = & \sum \vec{r}_j \times m_j \vec{R}_0 + \sum \vec{r}_j \times m_j (\vec{\Omega} \times \vec{r}_j) + \sum \vec{r}_j \times m_j (\vec{\Omega} \times \vec{r}_j) \\ & + \sum \vec{r}_j \times m_j \left[\vec{\Omega} \times (\vec{\Omega} \times \vec{r}_j) \right] + \sum \vec{r}_j \times m_j (\vec{\Omega} \times \vec{r}_j) + \sum \vec{r}_j \times m_j \vec{r}_j \end{aligned} \quad (A-4)$$

or

$$\begin{aligned}
 \vec{M} = m_s \vec{r}_s \times \ddot{\vec{R}}_0 + \sum \vec{r}_j \times m_j (\vec{\Omega} \times \vec{r}_j) + \sum \vec{r}_j \times m_j (\dot{\vec{\Omega}} \times \vec{r}_j) \\
 + \sum \vec{r}_j \times m_j (\vec{\Omega} \times \dot{\vec{r}}_j) + \sum \vec{\Omega} \times \left[\vec{r}_j \times m_j (\vec{\Omega} \times \vec{r}_j) \right] \\
 + \sum \vec{\Omega} \times m_j (\vec{r}_j \times \dot{\vec{r}}_j) + \sum \vec{r}_j \times m_j \ddot{\vec{r}}_j
 \end{aligned} \tag{A-5}$$

The acceleration of the origin $\ddot{\vec{R}}_0$ is found from the general force (ref. 6) equation

$$\vec{P} = m_s \left[\ddot{\vec{R}}_0 + \ddot{\vec{r}}_s + \vec{\Omega} \times \vec{r}_s + 2\vec{\Omega} \times \dot{\vec{r}}_s + \vec{\Omega} \times (\vec{\Omega} \times \vec{r}_s) \right] \tag{A-6}$$

and the first term of (A-5) may now be written as

$$\begin{aligned}
 m_s \vec{r}_s \times \ddot{\vec{R}}_0 &= \vec{r}_s \times \vec{P} - \vec{r}_s \times m_s (\vec{\Omega} \times \vec{r}_s) - \vec{r}_s \times m_s (\dot{\vec{\Omega}} \times \vec{r}_s) \\
 &\quad - \vec{r}_s \times m_s \left[\vec{\Omega} \times (\vec{\Omega} \times \vec{r}_s) \right] - \vec{r}_s \times m_s (\vec{\Omega}_s \times \dot{\vec{r}}_s) - \vec{r}_s \times m_s \ddot{\vec{r}}_s \\
 &= \vec{r}_s \times \vec{P} - \vec{r}_s \times m_s (\vec{\Omega} \times \vec{r}_s) - \vec{r}_s \times m_s (\dot{\vec{\Omega}} \times \vec{r}_s) \\
 &\quad - \vec{r}_s \times m_s (\vec{\Omega} \times \dot{\vec{r}}_s) - \vec{\Omega} \times \left[\vec{r}_s \times m_s (\vec{\Omega} \times \vec{r}_s) \right] - \vec{\Omega} \times m_s (\vec{r}_s \times \dot{\vec{r}}_s) \\
 &\quad - \vec{r}_s \times m_s \ddot{\vec{r}}_s
 \end{aligned} \tag{A-7}$$

The equation of motion becomes

$$\begin{aligned}
 \vec{M} = \vec{r}_s \times \vec{P} + & \left\{ \left[\sum \vec{r}_j \times m_j (\vec{\Omega} \times \vec{r}_j) - \vec{r}_s \times m_s (\vec{\Omega} \times \vec{r}_s) \right] \right. \\
 & + \left[\sum \vec{r}_j \times m_j (\vec{\dot{\Omega}} \times \vec{r}_j) - \vec{r}_s \times m_s (\vec{\dot{\Omega}} \times \vec{r}_s) \right] + \left[\sum \vec{r}_j \times m_j (\vec{\Omega} \times \vec{\dot{r}}_j) \right. \\
 & \left. \left. - \vec{r}_s \times m_s (\vec{\Omega} \times \vec{\dot{r}}_s) \right] + \vec{\Omega} \times \left[\sum \vec{r}_j \times m_j (\vec{\Omega} \times \vec{r}_j) - \vec{r}_s \times m_s (\vec{\Omega} \times \vec{r}_s) \right] \right\} \\
 & + \left\{ \Omega \times \left[\sum m_j \vec{r}_j \times \vec{\dot{r}}_j - m_s \vec{r}_s \times \vec{\dot{r}}_s \right] + \left[\sum \vec{r}_j \times m_j \vec{\ddot{r}}_j - \vec{r}_s \times m_s \vec{\ddot{r}}_s \right] \right\}
 \end{aligned} \tag{A-8}$$

where the vector from the center of mass to the origin is

$$\vec{r}_s = \sum \frac{m_j}{m_s} \vec{r}_j \tag{A-9}$$

To reduce (A-8) to a more useful form, the particle system will be represented as a large mass associated with the spacecraft and fixed with respect to the X Y Z axes and n smaller masses which move relative to the X Y Z axes. The rigid-body angular momentum vectors of the spacecraft, the n moving masses, and the spacecraft mass center will be designated as \vec{H}_0 , \vec{H}_n , and \vec{H}_s , respectively. The rigid-body angular momentum of the system \vec{H} referred to the system center of mass is then

$$\vec{H} = \vec{H}_0 + \vec{H}_n - \vec{H}_s \tag{A-10}$$

where

$$\left. \begin{aligned} \vec{H}_S &= \vec{r}_S \times m_S(\vec{\Omega}_S \times \vec{r}_S) \\ \vec{H}_n &= \sum_{j=1}^n \vec{r}_j \times m_j(\vec{\Omega}_j \times \vec{r}_j) \\ \vec{H}_O &= \sum_{j=n+1} \vec{r}_j \times m_j(\vec{\Omega}_j \times \vec{r}_j) \end{aligned} \right\} \quad (A-11)$$

and (A-8) can be rewritten as

$$\begin{aligned} \vec{M} = \vec{r}_S \times \vec{P} + \frac{d\vec{H}}{dt} + \left\{ \vec{\Omega} \times \left[\sum_{j=1}^n m_j \vec{r}_j \times \vec{r}_j - m_S \vec{r}_S \times \vec{r}_S \right] \right. \\ \left. + \left[\sum_{j=1}^n \vec{r}_j \times m_j \ddot{\vec{r}}_j - \vec{r}_S \times m_S \ddot{\vec{r}}_S \right] \right\} \end{aligned} \quad (A-12)$$

with

$$\vec{r}_S = \sum_{j=1}^n \frac{m_j}{m_S} \vec{r}_j \quad (A-13)$$

In component form, one obtains

$$\begin{aligned} M_x &= y_S P_z - z_S P_y + I_x \dot{\Omega}_x - I_{xy} \dot{\Omega}_y - I_{xz} \dot{\Omega}_z + \dot{I}_x \Omega_x - \dot{I}_{xy} \Omega_y - \dot{I}_{xz} \Omega_z \\ &\quad - \Omega_z (I_y \Omega_y - I_{yz} \Omega_z - I_{yx} \Omega_x) + \Omega_y (I_z \Omega_z - I_{zx} \Omega_x - I_{zy} \Omega_y) \\ &\quad + \left\{ \left[\sum_{j=1}^n m_j (x_j \dot{y}_j - y_j \dot{x}_j) \right] - \left[m_S (x_S \dot{y}_S - y_S \dot{x}_S) \right] \right\} \Omega_y \\ &\quad + \left\{ \left[\sum_{j=1}^n m_j (x_j \dot{z}_j - z_j \dot{x}_j) \right] - \left[m_S (x_S \dot{z}_S - z_S \dot{x}_S) \right] \right\} \Omega_z \\ &\quad + \left\{ \left[\sum_{j=1}^n m_j (y_j \dot{z}_j - z_j \dot{y}_j) \right] - \left[m_S (y_S \dot{z}_S - z_S \dot{y}_S) \right] \right\} \end{aligned} \quad (A-14)$$

$$\begin{aligned}
 M_y = & z_s P_x - x_s P_z + I_y \dot{\Omega}_y - I_{yz} \dot{\Omega}_z - I_{yx} \dot{\Omega}_x + \dot{I}_y \Omega_y - \dot{I}_{yz} \Omega_z - \dot{I}_{yx} \Omega_x \\
 & - \Omega_x (I_z \Omega_z - I_{zx} \Omega_z - I_{zy} \Omega_y) + \Omega_z (I_x \Omega_x - I_{xy} \Omega_y - I_{xz} \Omega_z) \\
 & + \left\{ \left[\sum_{j=1}^n m_j (y_j \dot{x}_j - x_j \dot{y}_j) \right] - \left[m_s (y_s \dot{x}_s - x_s \dot{y}_s) \right] \right\} \Omega_x \\
 & + \left\{ \left[\sum_{j=1}^n m_j (y_j \dot{z}_j - z_j \dot{y}_j) \right] - \left[m_s (y_s \dot{z}_s - z_s \dot{y}_s) \right] \right\} \Omega_z \\
 & + \left\{ \left[\sum_{j=1}^n m_j (z_j \ddot{x}_j - x_j \ddot{z}_j) \right] - \left[m_s (z_s \ddot{x}_s - x_s \ddot{z}_s) \right] \right\} \quad (A-15)
 \end{aligned}$$

and

$$\begin{aligned}
 M_z = & x_s P_y - y_s P_x + I_z \dot{\Omega}_z - I_{zx} \dot{\Omega}_x - I_{zy} \dot{\Omega}_y + \dot{I}_z \Omega_z - \dot{I}_{zx} \Omega_x - \dot{I}_{zy} \Omega_y \\
 & - \Omega_y (I_x \Omega_x - I_{xy} \Omega_y - I_{xz} \Omega_z) + \Omega_x (I_y \Omega_y - I_{yz} \Omega_z - I_{yx} \Omega_x) \\
 & + \left\{ \left[\sum_{j=1}^n m_j (z_j \dot{x}_j - x_j \dot{z}_j) \right] - \left[m_s (z_s \dot{x}_s - x_s \dot{z}_s) \right] \right\} \Omega_x \\
 & + \left\{ \left[\sum_{j=1}^n m_j (z_j \dot{y}_j - y_j \dot{z}_j) \right] - \left[m_s (z_s \dot{y}_s - y_s \dot{z}_s) \right] \right\} \Omega_y \\
 & + \left\{ \left[\sum_{j=1}^n m_j (x_j \ddot{y}_j - y_j \ddot{x}_j) \right] - \left[m_s (x_s \ddot{y}_s - y_s \ddot{x}_s) \right] \right\} \quad (A-16)
 \end{aligned}$$

where

$$\left. \begin{aligned}
 I_x &= I_{x0} + \left[\sum_{j=1}^n m_j (y_j^2 + z_j^2) - m_s (y_s^2 + z_s^2) \right] \\
 I_y &= I_{y0} + \left[\sum_{j=1}^n m_j (x_j^2 + z_j^2) - m_s (x_s^2 + z_s^2) \right] \\
 I_z &= I_{z0} + \left[\sum_{j=1}^n m_j (x_j^2 + y_j^2) - m_s (x_s^2 + y_s^2) \right] \\
 I_{xz} &= \left[\sum_{j=1}^n m_j (x_j z_j) - m_s (x_s z_s) \right] \\
 I_{yz} &= \left[\sum_{j=1}^n m_j (y_j z_j) - m_s (y_s z_s) \right] \\
 I_{xy} &= \left[\sum_{j=1}^n m_j (x_j y_j) - m_s (x_s y_s) \right]
 \end{aligned} \right\} (A-17)$$

and

$$\left. \begin{aligned}
 \dot{I}_x &= 2 \left[\sum_{j=1}^n m_j (y_j \dot{y}_j + z_j \dot{z}_j) - m_s (y_s \dot{y}_s + z_s \dot{z}_s) \right] \\
 \dot{I}_y &= 2 \left[\sum_{j=1}^n m_j (x_j \dot{x}_j + z_j \dot{z}_j) - m_s (x_s \dot{x}_s + z_s \dot{z}_s) \right] \\
 \dot{I}_z &= 2 \left[\sum_{j=1}^n m_j (x_j \dot{x}_j + y_j \dot{y}_j) - m_s (x_s \dot{x}_s + y_s \dot{y}_s) \right]
 \end{aligned} \right\} (A-18)$$

$$\left. \begin{aligned} \dot{i}_{xz} &= \left[\sum_{j=1}^n m_j (x_j \dot{z}_j + z_j \dot{x}_j) - m_s (x_s \dot{z}_s + z_s \dot{x}_s) \right] \\ \dot{i}_{yz} &= \left[\sum_{j=1}^n m_j (y_j \dot{z}_j + z_j \dot{y}_j) - m_s (y_s \dot{z}_s + z_s \dot{y}_s) \right] \\ \dot{i}_{xy} &= \left[\sum_{j=1}^n m_j (x_j \dot{y}_j + y_j \dot{x}_j) - m_s (x_s \dot{y}_s + y_s \dot{x}_s) \right] \end{aligned} \right\} \quad (A-18)$$

The coordinates of the jth moving mass are x_j , y_j , z_j , and the coordinates of the mass center are

$$\left. \begin{aligned} x_s &= \sum_{j=1}^n \frac{m_j}{m_s} x_j \\ y_s &= \sum_{j=1}^n \frac{m_j}{m_s} y_j \\ z_s &= \sum_{j=1}^n \frac{m_j}{m_s} z_j \end{aligned} \right\} \quad (A-19)$$

For the special case when only one mass m with coordinates x , y , z is moving with respect to the spacecraft, the equations of motion yield

$$\begin{aligned} M_x &= \frac{m}{m_s} (y \dot{p}_z - z \dot{p}_y) + I_x \dot{\Omega}_x - I_{xy} \dot{\Omega}_y - I_{xz} \dot{\Omega}_z + \dot{i}_x \Omega_x - \dot{i}_{xy} \Omega_y - \dot{i}_{xz} \Omega_z \\ &\quad - \Omega_z (I_y \Omega_y - I_{yz} \Omega_z - I_{yx} \Omega_x) + \Omega_y (I_z \Omega_z - I_{zx} \Omega_x - I_{zy} \Omega_y) \\ &\quad + Q \left[(x \dot{y} - y \dot{x}) \Omega_y + (x \dot{z} - z \dot{x}) \Omega_z + (y \dot{z} - z \dot{y}) \right] \end{aligned} \quad (A-20)$$

$$\begin{aligned}
 M_y = & \frac{m}{m_s} (zP_x - xP_z) + I_y \dot{\Omega}_y - I_{yz} \dot{\Omega}_z - I_{yx} \dot{\Omega}_x + \dot{I}_y \Omega_y - \dot{I}_{yz} \Omega_z - \dot{I}_{yx} \Omega_x \\
 & - \Omega_x (I_z \Omega_z - I_{zx} \Omega_x - I_{zy} \Omega_y) + \Omega_z (I_x \Omega_x - I_{xy} \Omega_y - I_{xz} \Omega_z) \\
 & + Q \left[(y\dot{x} - x\dot{y}) \Omega_x + (y\dot{z} - z\dot{y}) \Omega_z + (z\dot{x} - x\dot{z}) \right] \quad (A-21)
 \end{aligned}$$

and

$$\begin{aligned}
 M_z = & \frac{m}{m_s} (xP_y - yP_x) + I_z \dot{\Omega}_z - I_{zx} \dot{\Omega}_x - I_{zy} \dot{\Omega}_y + \dot{I}_z \Omega_z - \dot{I}_{zx} \Omega_x - \dot{I}_{zy} \Omega_y \\
 & - \Omega_y (I_x \Omega_x - I_{xy} \Omega_y - I_{xz} \Omega_z) + \Omega_x (I_y \Omega_y - I_{yz} \Omega_z - I_{yx} \Omega_x) \\
 & + Q \left[(z\dot{x} - x\dot{z}) \Omega_x + (z\dot{y} - y\dot{z}) \Omega_y + (x\dot{y} - y\dot{x}) \right] \quad (A-22)
 \end{aligned}$$

with

$$\left. \begin{aligned}
 I_x &= I_{x0} + Q(y^2 + z^2) \\
 I_y &= I_{y0} + Q(x^2 + z^2) \\
 I_z &= I_{z0} + Q(x^2 + y^2) \\
 I_{xz} &= Q(xz) \\
 I_{yz} &= Q(yz) \\
 I_{xy} &= Q(xy)
 \end{aligned} \right\} \quad (A-23)$$

and

$$\left. \begin{aligned}
 \dot{I}_x &= 2Q(y\dot{y} + z\dot{z}) \\
 \dot{I}_y &= 2Q(x\dot{x} + z\dot{z}) \\
 \dot{I}_z &= 2Q(x\dot{x} + y\dot{y})
 \end{aligned} \right\} \quad (A-24)$$

$$\left. \begin{aligned} \dot{I}_{xz} &= Q(x\dot{z} + z\dot{x}) \\ \dot{I}_{yz} &= Q(y\dot{z} + z\dot{y}) \\ \dot{I}_{xy} &= Q(x\dot{y} + y\dot{x}) \end{aligned} \right\} \quad (A-24)$$

where Q is given by

$$Q = \frac{m(m_S - m)}{m_S} \quad (A-25)$$

The spacecraft equations of motion (A-14) to (A-16) can be solved for the body rates Ω_x , Ω_y , and Ω_z . The motion of the rotating spacecraft is then defined in terms of the modified Euler angles ψ , θ , and ϕ . These angles, as shown in figure 2, relate the moving body axes $X Y Z$ to the intermediate reference axes $X_I Y_I Z_I$. From the figure one notes that the time derivatives of the Euler angles are

$$\left. \begin{aligned} \dot{\phi} &= \Omega_x + \Omega_y \tan \theta \sin \phi + \Omega_z \tan \theta \cos \phi \\ \dot{\theta} &= \Omega_y \cos \phi - \Omega_z \sin \phi \\ \dot{\psi} &= \Omega_z \cos \phi \sec \theta + \Omega_y \sin \phi \sec \theta \end{aligned} \right\} \quad (A-26)$$

The Euler angles found from (A-26) and the body rates found from (A-14) to (A-16) completely define the rotational motion of the spinning spacecraft.

For a large number of practical applications, one is concerned with motions involving small oscillations of the spacecraft spin axis from an equilibrium reference position. If it is assumed that the spacecraft

spins about its Z axis, that the Z axis is initially an axis of maximum or minimum inertia, and that the Z_I axis is selected as the inertial reference, then

$$\begin{aligned} \sin \varphi &\cong \tan \varphi \cong \varphi & \cos \varphi &\cong 1 \\ \sin \theta &\cong \tan \theta \cong \theta & \cos \theta &\cong 1 \end{aligned} \quad (A-27)$$

and

$$\begin{aligned} \Omega_x &\ll \Omega_z \\ \Omega_y &\ll \Omega_z \end{aligned} \quad (A-28)$$

for the small oscillation regime. Consistent with these assumptions, one can consider the variable inertia terms to be sufficiently small in comparison with the spacecraft moments of inertia so that they may be neglected when multiplied by the oscillatory body rates or any angular accelerations.

The reduction of the nonlinear governing equations to linear approximations can best be accomplished by first converting (A-14) through (A-16) to nondimensional form. As was done in reference 4, one may introduce a nondimensional time τ , an inertia term ϵ_{pq} , and a nondimensional mass μ_j by

$$\tau = \Omega_{z0} t \quad \epsilon_{pq} = \frac{I_{pq}}{I_{z0}} \quad \mu_j = \frac{m_j}{m_s} \quad (A-29)$$

where p and q range over x , y , and z . The remaining nondimensional terms are then

$$\left. \begin{aligned} \omega_p &= \frac{\Omega_p}{\Omega_{z0}} & \dot{\omega}_p &= \frac{\dot{\Omega}_p}{\Omega_{z0}^2} & \dot{\epsilon}_{pq} &= \frac{\dot{I}_{pq}}{I_{z0}\Omega_{z0}} \\ L_p &= \frac{M_p}{I_{z0}\Omega_{z0}^2} & \rho_p &= \frac{P_p}{\Omega_{z0}^2} \sqrt{\frac{1}{I_{z0}m_s}} \\ u_j &= x_j \sqrt{\frac{m_s}{I_{z0}}} & \dot{u}_j &= \frac{\dot{x}_j}{\Omega_{z0}} \sqrt{\frac{m_s}{I_{z0}}} & \ddot{u}_j &= \frac{\ddot{x}_j}{\Omega_{z0}^2} \sqrt{\frac{m_s}{I_{z0}}} \\ v_j &= y_j \sqrt{\frac{m_s}{I_{z0}}} & w_j &= z_j \sqrt{\frac{m_s}{I_{z0}}} \end{aligned} \right\} \quad (A-30)$$

and the nondimensional equations of motion become

$$\begin{aligned} L_x &= v_s \rho_z - w_s \rho_y + \epsilon_{xx} \dot{\omega}_x - \epsilon_{xy} \dot{\omega}_y - \epsilon_{xz} \dot{\omega}_z - \dot{\epsilon}_x \omega_x - \dot{\epsilon}_{xy} \omega_y - \dot{\epsilon}_{xz} \omega_z \\ &\quad - \omega_z (\epsilon_{yy} \omega_y - \epsilon_{yz} \omega_z - \epsilon_{yx} \omega_x) + \omega_y (\epsilon_{zz} \omega_z - \epsilon_{zx} \omega_x - \epsilon_{zy} \omega_y) \\ &\quad + \left\{ \left[\sum_{j=1}^n \mu_j (u_j \dot{v}_j - v_j \dot{u}_j) \right] - (u_s \dot{v}_s - v_s \dot{u}_s) \right\} \omega_y \\ &\quad + \left\{ \left[\sum_{j=1}^n \mu_j (u_j \dot{w}_j - w_j \dot{u}_j) \right] - (u_s \dot{w}_s - w_s \dot{u}_s) \right\} \omega_z \\ &\quad + \left\{ \left[\sum_{j=1}^n \mu_j (v_j \ddot{w}_j - w_j \ddot{v}_j) \right] - (v_s \ddot{w}_s - w_s \ddot{v}_s) \right\} \end{aligned} \quad (A-31)$$

$$\begin{aligned}
 L_y &= w_s \rho_x - u_s \rho_z + \epsilon_y \dot{\omega}_y - \epsilon_{yz} \dot{\omega}_z - \dot{\epsilon}_{yx} \omega_x + \dot{\epsilon}_y \omega_y - \dot{\epsilon}_{yz} \omega_z - \epsilon_{yx} \omega_x \\
 &\quad - \omega_x (\epsilon_z \omega_z - \epsilon_{zx} \omega_x - \epsilon_{zy} \omega_y) + \omega_z (\epsilon_x \omega_x - \epsilon_{xy} \omega_y - \epsilon_{xz} \omega_z) \\
 &\quad + \left\{ \left[\sum_{j=1}^n \mu_j (v_j \ddot{u}_j - u_j \ddot{v}_j) \right] - (v_s \ddot{u}_s - u_s \ddot{v}_s) \right\} \omega_x \\
 &\quad + \left\{ \left[\sum_{j=1}^n \mu_j (v_j \ddot{w}_j - w_j \ddot{v}_j) \right] - (v_s \ddot{w}_s - w_s \ddot{v}_s) \right\} \omega_z \\
 &\quad + \left\{ \left[\sum_{j=1}^n \mu_j (w_j \ddot{u}_j - u_j \ddot{w}_j) \right] - (w_s \ddot{u}_s - u_s \ddot{w}_s) \right\} \quad (A-32)
 \end{aligned}$$

and

$$\begin{aligned}
 L_z &= u_s \rho_y - v_s \rho_x + \epsilon_z \dot{\omega}_z - \epsilon_{zx} \dot{\omega}_x - \epsilon_{zy} \dot{\omega}_y + \dot{\epsilon}_z \omega_z - \dot{\epsilon}_{zx} \omega_x - \dot{\epsilon}_{zy} \omega_y \\
 &\quad - \omega_y (\epsilon_x \omega_x - \epsilon_{xy} \omega_y - \epsilon_{xz} \omega_z) + \omega_x (\epsilon_y \omega_y - \epsilon_{yz} \omega_z - \epsilon_{yx} \omega_x) \\
 &\quad + \left\{ \left[\sum_{j=1}^n \mu_j (w_j \ddot{u}_j - u_j \ddot{w}_j) \right] - (w_s \ddot{u}_s - u_s \ddot{w}_s) \right\} \omega_x \\
 &\quad + \left\{ \left[\sum_{j=1}^n \mu_j (w_j \ddot{v}_j - v_j \ddot{w}_j) \right] - (w_s \ddot{v}_s - v_s \ddot{w}_s) \right\} \omega_y \\
 &\quad + \left\{ \left[\sum_{j=1}^n \mu_j (u_j \ddot{v}_j - v_j \ddot{u}_j) \right] - (u_s \ddot{v}_s - v_s \ddot{u}_s) \right\} \quad (A-33)
 \end{aligned}$$

where

$$\left. \begin{aligned} \epsilon_x &= \epsilon_{x0} + \left[\sum_{j=1}^n \mu_j (v_j^2 + w_j^2) - (v_s^2 + w_s^2) \right] \\ \epsilon_y &= \epsilon_{y0} + \left[\sum_{j=1}^n \mu_j (u_j^2 + w_j^2) - (u_s^2 + w_s^2) \right] \\ \epsilon_z &= \epsilon_{z0} + \left[\sum_{j=1}^n \mu_j (u_j^2 + v_j^2) - (u_s^2 + v_s^2) \right] \\ \epsilon_{xz} &= \left[\sum_{j=1}^n \mu_j (u_j w_j) - (u_s w_s) \right] \\ \epsilon_{yz} &= \left[\sum_{j=1}^n \mu_j (v_j w_j) - (v_s w_s) \right] \\ \epsilon_{xy} &= \left[\sum_{j=1}^n \mu_j (u_j v_j) - (u_s v_s) \right] \end{aligned} \right\} \quad (A-34)$$

In accordance with the small oscillation assumptions, take ω_k , $\theta\varphi$, $\dot{\omega}_p$, θ^2 , φ^2 , L_p , ρ_p , and the variable inertia terms

$$\sum_{j=1}^n \mu_j u_j^2, \quad \sum_{j=1}^n \mu_j v_j^2, \quad \sum_{j=1}^n \mu_j w_j^2, \quad \sum_{j=1}^n \mu_j u_j v_j, \quad \sum_{j=1}^n \mu_j u_j w_j, \quad \sum_{j=1}^n \mu_j v_j w_j,$$

and their derivatives to be of order Δ . Here Δ is restricted to be sufficiently small so that terms of higher order than Δ may be neglected in the governing equations.

Thus, it follows that

$$\begin{aligned}
 \underbrace{I_x}_{O[\Delta]} &= \underbrace{u_s \rho_z - w_s \rho_y}_{O[\Delta^2]} + \underbrace{\epsilon_x \dot{\omega}_x}_{O[\Delta]} - \underbrace{\epsilon_{xy} \dot{\omega}_y}_{O[\Delta^2]} - \underbrace{\epsilon_{xz} \dot{\omega}_z}_{O[\Delta^2]} + \underbrace{\dot{\epsilon}_x \omega_x}_{O[\Delta^2]} - \underbrace{\dot{\epsilon}_{xy} \omega_y}_{O[\Delta^2]} - \underbrace{\dot{\epsilon}_{xz} \omega_z}_{O[\Delta]} \\
 &\quad - \omega_z \underbrace{(\epsilon_y \omega_y - \epsilon_{yz} \omega_z - \epsilon_{yx} \omega_x)}_{O[\Delta]} + \omega_y \underbrace{(\epsilon_z \omega_z - \epsilon_{zx} \omega_x - \epsilon_{zy} \omega_y)}_{O[\Delta^3]} \\
 &\quad + \underbrace{\left\{ \left[\sum_{j=1}^n \mu_j (u_j \dot{v}_j - v_j \dot{u}_j) \right] - (u_s \dot{v}_s - v_s \dot{u}_s) \right\}}_{O[\Delta^2]} \omega_y \\
 &\quad + \underbrace{\left\{ \left[\sum_{j=1}^n \mu_j (u_j \dot{w}_j - w_j \dot{u}_j) \right] - (u_s \dot{w}_s - w_s \dot{u}_s) \right\}}_{O[\Delta]} \omega_z \\
 &\quad + \underbrace{\left\{ \left[\sum_{j=1}^n \mu_j (v_j \ddot{w}_j - w_j \ddot{v}_j) \right] - (v_s \ddot{w}_s - w_s \ddot{v}_s) \right\}}_{O[\Delta]}
 \end{aligned} \tag{A-35}$$

$$\begin{aligned}
 \underbrace{L_y}_{O[\Delta]} &= \underbrace{w_s \rho_x - u_s \rho_z}_{O[\Delta^2]} + \underbrace{\epsilon_y \dot{\omega}_y}_{O[\Delta]} - \underbrace{\epsilon_{yz} \dot{\omega}_z}_{O[\Delta^2]} - \underbrace{\epsilon_{yx} \dot{\omega}_x}_{O[\Delta^2]} - \underbrace{\dot{\epsilon}_y \omega_y}_{O[\Delta^2]} - \underbrace{\dot{\epsilon}_{yz} \omega_z}_{O[\Delta]} - \underbrace{\dot{\epsilon}_{yx} \omega_x}_{O[\Delta^2]} \\
 &\quad - \underbrace{\omega_x (\epsilon_z \omega_z - \epsilon_{zx} \omega_x - \epsilon_{zy} \omega_y)}_{O[\Delta]} + \underbrace{\omega_z (\epsilon_x \omega_x - \epsilon_{xy} \omega_y - \epsilon_{xz} \omega_z)}_{O[\Delta]} \\
 &\quad + \underbrace{\left\{ \left[\sum_{j=1}^n \mu_j (v_j \dot{u}_j - u_j \dot{v}_j) \right] - (v_s \dot{u}_s - u_s \dot{v}_s) \right\}}_{O[\Delta^2]} \omega_x \\
 &\quad + \underbrace{\left\{ \left[\sum_{j=1}^n \mu_j (v_j \dot{w}_j - w_j \dot{v}_j) \right] - (v_s \dot{w}_s - w_s \dot{v}_s) \right\}}_{O[\Delta]} \omega_z \\
 &\quad + \underbrace{\left\{ \left[\sum_{j=1}^n \mu_j (w_j \ddot{u}_j - u_j \ddot{w}_j) \right] - (w_s \ddot{u}_s - u_s \ddot{w}_s) \right\}}_{O[\Delta]}
 \end{aligned}
 \tag{A-36}$$

and

$$\begin{aligned}
 \underbrace{L_z}_{O[\Delta]} &= \underbrace{u_s \rho_y - v_s \rho_x}_{O[\Delta^2]} + \underbrace{\epsilon_z \dot{\omega}_z}_{O[\Delta]} - \underbrace{\epsilon_{zx} \dot{\omega}_x}_{O[\Delta^2]} - \underbrace{\epsilon_{zy} \dot{\omega}_y}_{O[\Delta^2]} + \underbrace{\dot{\epsilon}_z \omega_z}_{O[\Delta]} - \underbrace{\dot{\epsilon}_{zx} \omega_x}_{O[\Delta^2]} - \underbrace{\dot{\epsilon}_{zy} \omega_y}_{O[\Delta^2]} \\
 &\quad - \underbrace{\omega_y (\epsilon_x \omega_x - \epsilon_{xy} \omega_y - \epsilon_{xz} \omega_z)}_{O[\Delta^2]} + \underbrace{\omega_x (\epsilon_y \omega_y - \epsilon_{yz} \omega_z - \epsilon_{yx} \omega_x)}_{O[\Delta^2]} \\
 &\quad + \underbrace{\left\{ \left[\sum_{j=1}^n \mu_j (w_j \dot{v}_j - v_j \dot{w}_j) \right] - (w_s \dot{v}_s - v_s \dot{w}_s) \right\}}_{O[\Delta^2]} \omega_y \\
 &\quad + \underbrace{\left\{ \left[\sum_{j=1}^n \mu_j (w_j \dot{u}_j - u_j \dot{w}_j) \right] - (w_s \dot{u}_s - u_s \dot{w}_s) \right\}}_{O[\Delta^2]} \omega_x \\
 &\quad + \underbrace{\left\{ \left[\sum_{j=1}^n \mu_j (u_j \ddot{v}_j - v_j \ddot{u}_j) \right] - (u_s \ddot{v}_s - v_s \ddot{u}_s) \right\}}_{O[\Delta]}
 \end{aligned} \tag{A-37}$$

or neglecting terms of higher order

$$\begin{aligned}
 L_x = & \epsilon_x \dot{\omega}_x + (\epsilon_z - \epsilon_y) \omega_y \omega_z - \omega_z (\dot{\epsilon}_{xz} - \epsilon_{yz} \omega_z) \\
 & + \left\{ \left[\sum_{j=1}^n \mu_j (u_j \dot{w}_j - w_j \dot{u}_j) \right] - (u_s \dot{w}_s - w_s \dot{u}_s) \right\} \omega_z \\
 & + \left\{ \left[\sum_{j=1}^n \mu_j (v_j \ddot{w}_j - w_j \ddot{v}_j) \right] - (v_s \ddot{w}_s - w_s \ddot{v}_s) \right\} \quad (A-38)
 \end{aligned}$$

$$\begin{aligned}
 L_y = & \epsilon_y \dot{\omega}_y - (\epsilon_z - \epsilon_x) \omega_x \omega_z - \omega_z (\dot{\epsilon}_{yz} + \epsilon_{xz} \omega_z) \\
 & + \left\{ \left[\sum_{j=1}^n \mu_j (v_j \dot{w}_j - w_j \dot{v}_j) \right] - (v_s \dot{w}_s - w_s \dot{v}_s) \right\} \omega_z \\
 & + \left\{ \left[\sum_{j=1}^n \mu_j (w_j \ddot{u}_j - u_j \ddot{w}_j) \right] - (w_s \ddot{u}_s - u_s \ddot{w}_s) \right\} \quad (A-39)
 \end{aligned}$$

$$L_z = \epsilon_z \dot{\omega}_z + \dot{\epsilon}_z \omega_z + \left\{ \left[\sum_{j=1}^n \mu_j (u_j \ddot{v}_j - v_j \ddot{u}_j) \right] - (u_s \ddot{v}_s - v_s \ddot{u}_s) \right\} \quad (A-40)$$

For the same range of disturbances, the Euler angles are given by

$$\left. \begin{aligned} \frac{d\varphi}{d\tau} &= \underbrace{\omega_x}_{O[\Delta]} + \underbrace{\omega_y \theta \varphi}_{O[\Delta^2]} + \underbrace{\omega_z \theta}_{O[\Delta^{1/2}]} \\ \frac{d\theta}{d\tau} &= \underbrace{\omega_y}_{O[\Delta]} - \underbrace{\omega_z \varphi}_{O[\Delta^{1/2}]} \\ \frac{d\psi}{d\tau} &= \underbrace{\omega_z}_{O[1]} + \underbrace{\omega_y \varphi}_{O[\Delta^{3/2}]} \end{aligned} \right\} \quad (A-41)$$

and again neglecting terms of order higher than Δ

$$\left. \begin{aligned} \frac{d\varphi}{d\tau} &= \omega_x + \omega_z \theta \\ \frac{d\theta}{d\tau} &= \omega_y - \omega_z \varphi \\ \frac{d\psi}{d\tau} &= \omega_z \end{aligned} \right\} \quad (A-42)$$

If the spacecraft dynamics are well conditioned, the above equations should give reasonable results in the small angle and rate regime, for which

$$-15^\circ \leq \varphi \leq 15^\circ$$

$$-15^\circ \leq \theta \leq 15^\circ$$

or

$$-0.0685 \leq \Delta \leq 0.0685$$

Solutions for higher values of Δ will lead to correspondingly less accurate solutions.

Since the form of the physical and nondimensional differential equations is identical, only the more convenient physical equations of motion will be used. These equations can then be written as

$$\begin{aligned} \dot{\Omega}_x + \left\{ \left(\frac{I_z - I_y}{I_x} \right) \Omega_z \right\} \Omega_y = \frac{1}{I_x} \left\{ M_x + \Omega_z (\dot{I}_{xz} - I_{yz} \Omega_z) + \left[\sum_{j=1}^n m_j (z_j \dot{x}_j - x_j \dot{z}_j) \right. \right. \\ \left. \left. - m_s (z_s \dot{x}_s - x_s \dot{z}_s) \right] \Omega_z + \left[\sum_{j=1}^n m_j (z_j \ddot{y}_j - y_j \ddot{z}_j) \right] \right. \\ \left. - m_s (z_s \ddot{y}_s - y_s \ddot{z}_s) \right\} \quad (A-43) \end{aligned}$$

$$\begin{aligned} \dot{\Omega}_y - \left\{ \left(\frac{I_z - I_x}{I_y} \right) \Omega_z \right\} \Omega_x = \frac{1}{I_y} \left\{ M_y + \Omega_z (\dot{I}_{yz} + I_{xz} \Omega_z) + \left[\sum_{j=1}^n m_j (z_j \dot{y}_j - y_j \dot{z}_j) \right. \right. \\ \left. \left. - m_s (z_s \dot{y}_s - y_s \dot{z}_s) \right] \Omega_z + \left[\sum_{j=1}^n m_j (x_j \ddot{z}_j - z_j \ddot{x}_j) \right] \right. \\ \left. - m_s (x_s \ddot{z}_s - z_s \ddot{x}_s) \right\} \quad (A-44) \end{aligned}$$

and

$$\dot{\Omega}_z + \frac{\dot{I}_z}{I_z} \Omega_z = \frac{1}{I_z} \left\{ M_z + \left[\sum_{j=1}^n m_j (y_j \ddot{x}_j - x_j \ddot{y}_j) \right] - m_s (y_s \ddot{x}_s - x_s \ddot{y}_s) \right\} \quad (A-45)$$

where the moments of inertia I_x and I_y , in general, may be approximated by their initial values in (A-43) and (A-44), so that

$$\left. \begin{aligned} I_x &\approx I_{x0} + \left[\sum_{j=1}^n m_j (y_{j0}^2 + z_{j0}^2) \right] - m_s (y_{s0}^2 + z_{s0}^2) \\ I_y &\approx I_{y0} + \left[\sum_{j=1}^n m_j (x_{j0}^2 + z_{j0}^2) \right] - m_s (x_{s0}^2 + z_{s0}^2) \\ I_z &= I_{z0} + \left[\sum_{j=1}^n m_j (x_j^2 + y_j^2) \right] - m_s (x_s^2 + y_s^2) \end{aligned} \right\} \quad (A-46)$$

since the retention of variable inertia coefficients does not appear to add appreciably to the accuracy of the solutions. The other pertinent inertia terms are

$$\left. \begin{aligned} I_{xz} &= \left[\sum_{j=1}^n m_j (x_j z_j) \right] - m_s (x_s z_s) \\ I_{yz} &= \left[\sum_{j=1}^n m_j (y_j z_j) \right] - m_s (y_s z_s) \end{aligned} \right\} \quad (A-47)$$

and the required time derivatives of the inertia terms become

$$\left. \begin{aligned} \dot{I}_{xz} &= \left[\sum_{j=1}^n m_j (x_j \dot{z}_j + z_j \dot{x}_j) \right] - m_s (x_s \dot{z}_s + z_s \dot{x}_s) \\ \dot{I}_{yz} &= \left[\sum_{j=1}^n m_j (y_j \dot{z}_j + z_j \dot{y}_j) \right] - m_s (y_s \dot{z}_s + z_s \dot{y}_s) \\ \dot{I}_z &= 2 \left[\sum_{j=1}^n m_j (x_j \dot{x}_j + y_j \dot{y}_j) \right] - m_s (x_s \dot{x}_s + y_s \dot{y}_s) \end{aligned} \right\} \quad (A-48)$$

The Euler angle relations are given by

$$\left. \begin{aligned} \dot{\phi} - \Omega_z \theta &= \Omega_x \\ \dot{\theta} + \Omega_z \phi &= \Omega_y \\ \dot{\psi} &= \Omega_z \end{aligned} \right\} \quad (\text{A-49})$$

If results should be required in nondimensional form, one need only apply the transformations (A-29) and (A-30) to the solutions.

XV. APPENDIX B

PARTICULAR SOLUTION FUNCTIONS FOR THE
UNCONTROLLED SPACECRAFT

The forcing function for the differential equation with the constant moments of inertia approximation can be written as

$$F = \sum_{j=1}^f A_j F_j(t) \quad (B-1)$$

and thus the particular solutions are

$$\left. \begin{aligned} \bar{F} &= \sum_{j=1}^f A_j \bar{F}_j(t) \\ \bar{\bar{F}} &= \sum_{j=1}^f A_j \bar{\bar{F}}_j(t) \\ \dot{\bar{\bar{F}}} &= \sum_{j=1}^f A_j \dot{\bar{\bar{F}}}_j(t) \end{aligned} \right\} \quad (B-2)$$

where the functions $\bar{F}_j(t)$, $\bar{\bar{F}}_j(t)$, and $\dot{\bar{\bar{F}}}_j(t)$ are given by the inverse Laplace transforms

$$\left. \begin{aligned} \bar{F}_j(t) &= \mathcal{L}^{-1} \left\{ \frac{F_j(s)}{s^2 + \lambda^2} \right\} \\ \bar{\bar{F}}_j(t) &= \left(\frac{1}{\sigma^2 - \lambda^2} \right) \mathcal{L}^{-1} \left\{ \frac{F_j(s)}{s^2 + \lambda^2} - \frac{F_j(s)}{s^2 + \sigma^2} \right\} \\ \dot{\bar{\bar{F}}}_j(t) &= \left(\frac{1}{\sigma^2 - \lambda^2} \right) \mathcal{L}^{-1} \left\{ \frac{sF_j(s)}{s^2 + \lambda^2} - \frac{sF_j(s)}{s^2 + \sigma^2} \right\} \end{aligned} \right\} \quad (B-3)$$

A number of particular solution functions have been evaluated and are presented in tables 1 - 3. Other functions may be determined from (B-3) if needed.

The unit step function and the unit impulse function, that occur in these tables, are defined as

$$U(t) = \begin{cases} 0 & \text{for } t < 0 \\ 1 & \text{for } t > 0 \end{cases} \quad (\text{B-4})$$

and

$$\delta(t) = \begin{cases} 0 & \text{for } t \neq 0 \\ \text{with} \\ \int_{-\infty}^{\infty} \delta(t) dt = 1 \end{cases} \quad (\text{B-5})$$

where $t = 0$ is the initial time of application of the step or impulse disturbance.

TABLE 1.- SOLUTION TERMS FOR UNIT STEP AND UNIT IMPULSE FUNCTIONS

$F_j(t)$	$\bar{F}_j(t)$	$\bar{\bar{F}}_j(t)$
$U(t)$	$\frac{U(t)}{\lambda^2} [1 - \cos \lambda t]$	$\frac{U(t)}{\sigma^2 - \lambda^2} \left[\frac{1}{\lambda^2} (1 - \cos \lambda t) - \frac{1}{\sigma^2} (1 - \cos \sigma t) \right]$
$\dot{U}(t) = \delta(t)$	$\frac{U(t)}{\lambda} \sin \lambda t$	$\frac{U(t)}{\sigma^2 - \lambda^2} \left[\frac{1}{\lambda} \sin \lambda t - \frac{1}{\sigma} \sin \sigma t \right]$
$\ddot{U}(t) = \dot{\delta}(t)$	$U(t) \cos \lambda t$	$\frac{U(t)}{\sigma^2 - \lambda^2} [\cos \lambda t - \cos \sigma t]$
$\ddot{\ddot{U}}(t) = \ddot{\delta}(t)$	$\delta(t) - \lambda U(t) \sin \lambda t$	$\frac{U(t)}{\sigma^2 - \lambda^2} [\sigma^2 \cos \sigma t - \lambda^2 \cos \lambda t]$

TABLE 2.- SOLUTION FUNCTIONS FOR POWERS OF t

$F_j(t)$	$\bar{F}_j(t)$	$\bar{\bar{F}}_j(t)$
t	$\frac{1}{\lambda^2} \left[t - \frac{1}{\lambda} \sin \lambda t \right]$	$\frac{1}{\sigma^2 - \lambda^2} [\cos \lambda t - \cos \sigma t]$
t^2	$\frac{1}{\lambda^2} \left[t^2 - \frac{2}{\lambda^2} (1 - \cos \lambda t) \right]$	$\frac{2}{\sigma^2 - \lambda^2} \left\{ \frac{1}{\lambda^2} \left[t^2 - \frac{2}{\lambda} \sin \lambda t \right] - \frac{1}{\sigma^2} \left[t^2 - \frac{2}{\sigma} \sin \sigma t \right] \right\}$
t^n	$n! \left[\frac{1}{2\lambda^2} \left\{ \frac{1}{\lambda^2} \left[(-1)^n + 1 \right] \cos \lambda t + \frac{(-1)^n - 1}{\lambda} \sin \lambda t \right\} - \left\{ \sum_{N=0}^{n/2} \frac{(-1)^{N+1}}{2\lambda^2} \left[\frac{t}{(n-2N)!} \right] \frac{1}{\lambda} \sin \lambda t \right\} \right]$	$\frac{n!}{\sigma^2 - \lambda^2} \left\{ \left(\frac{-1}{\sigma^2} \right)^{N+1} - \left(\frac{-1}{\lambda^2} \right)^{N+1} \right\} \left\{ \frac{t}{(n-2N-1)!} \right\} + \frac{1}{2\lambda^2} \left\{ \sum_{N=0}^{N_{\max}+1} \frac{(-1)^N}{\lambda^2} \left[(-1)^n + 1 \right] \cos \lambda t + \left[\frac{(-1)^n - 1}{\lambda} \right] \sin \lambda t \right\} - \frac{1}{2\sigma^2} \left\{ \sum_{N=0}^{N_{\max}+1} \frac{(-1)^N}{\lambda^2} \left[(-1)^n + 1 \right] \cos \sigma t + \left[\frac{(-1)^n - 1}{\sigma} \right] \sin \sigma t \right\} \right\}$

The constant N_{\max} denotes the largest value of N within the summation limits.

TABLE 3.- SOLUTION TERMS FOR THE TRIGONOMETRIC FUNCTIONS $U(t) \sin pt$ AND $U(t) \cos pt$

$F_j(t)$	$\bar{F}_j(t)$	$\bar{\bar{F}}_j(t)$
$U(t) \sin pt$ $ \lambda \neq \rho \neq \sigma $	$\frac{U(t)}{\lambda^2 - \rho^2} \left[\sin pt - \frac{\rho}{\lambda} \sin \lambda t \right]$	$U(t) \left\{ \left[\frac{\sin pt}{(\lambda^2 - \rho^2)(\sigma^2 - \rho^2)} \right] + \frac{\rho}{\sigma} \left[\frac{\sin \sigma t}{(\sigma^2 - \rho^2)(\sigma^2 - \lambda^2)} \right] \right.$ $\left. + \frac{\rho}{\lambda} \left[\frac{\sin \lambda t}{(\lambda^2 - \rho^2)(\lambda^2 - \sigma^2)} \right] \right\}$
$U(t) \sin pt$ $ \rho = \lambda $	$\frac{U(t)}{2\lambda} \left[\frac{1}{\lambda} \sin \lambda t - t \cos \lambda t \right]$	$\frac{U(t)}{\sigma^2 - \lambda^2} \left\{ \left[\frac{\lambda \sin \sigma t}{\sigma(\sigma^2 - \lambda^2)} \right] + \left[\frac{\sigma^2 - \lambda^2}{2\lambda^2} \right] \left[\frac{\sin \lambda t}{\sigma^2 - \lambda^2} \right] \right.$ $\left. - \left[\frac{t \cos \lambda t}{2\lambda} \right] \right\}$
$U(t) \sin pt$ $ \rho = \sigma $	$\frac{U(t)}{\lambda^2 - \sigma^2} \left[\sin \sigma t - \frac{\sigma}{\lambda} \sin \lambda t \right]$	$\frac{U(t)}{\lambda^2 - \sigma^2} \left\{ \left[\frac{\sigma \sin \lambda t}{\lambda(\lambda^2 - \sigma^2)} \right] + \left[\frac{\lambda^2 - \sigma^2}{2\sigma^2} \right] \left[\frac{\sin \sigma t}{\lambda^2 - \sigma^2} \right] \right.$ $\left. - \left[\frac{t \cos \sigma t}{2\sigma} \right] \right\}$
$U(t) \cos pt$ $ \lambda \neq \rho \neq \sigma $	$\frac{U(t)}{\lambda^2 - \rho^2} [\cos pt - \cos \lambda t]$	$-U(t) \left\{ \left[\frac{\sin pt}{(\lambda^2 - \rho^2)(\sigma^2 - \rho^2)} \right] + \frac{\rho}{\sigma} \left[\frac{\sin \sigma t}{(\sigma^2 - \lambda^2)(\sigma^2 - \rho^2)} \right] \right.$ $\left. + \frac{\rho}{\lambda} \left[\frac{\sin \lambda t}{(\lambda^2 - \rho^2)(\lambda^2 - \sigma^2)} \right] \right\}$
$U(t) \cos pt$ $ \rho = \lambda $	$\frac{U(t)}{2\lambda} [t \sin \lambda t]$	$-\frac{U(t)}{\sigma^2 - \lambda^2} \left\{ \left[\frac{\sin \sigma t}{\sigma(\sigma^2 - \lambda^2)} \right] - \left[\frac{\sigma^2 + \lambda^2}{2\lambda} \right] \left[\frac{\sin \lambda t}{\sigma^2 - \lambda^2} \right] - t \cos \lambda t \right\}$
$U(t) \cos pt$ $ \rho = \sigma $	$\frac{U(t)}{\lambda^2 - \sigma^2} [\cos \sigma t - \cos \lambda t]$	$-\frac{U(t)}{\lambda^2 - \sigma^2} \left\{ \left[\frac{\sin \lambda t}{\lambda(\lambda^2 - \sigma^2)} \right] - \left[\frac{\lambda^2 + \sigma^2}{2\sigma} \right] \left[\frac{\sin \sigma t}{\lambda^2 - \sigma^2} \right] - t \cos \sigma t \right\}$

TABLE 4.- FORCING FUNCTION COEFFICIENTS FOR CHARACTERISTIC PERIODIC MOTIONS

Type of motion	Motion coordinates	Forcing function coefficients			
		E_0	E_1	E_2	E_3
Circumferential motion in plane perpendicular to Z axis	$x = r_0 \cos pt$ $y = r_0 \sin pt$ $z = z_0 u(t)$	$-1 \left[\frac{(p + \lambda_y)(\sigma + p)^2 I_{rz}}{I_x} \right]$	$-1 \left[\frac{(p + \lambda_x)(\sigma + p)^2 I_{rz}}{I_y} \right]$	$1 \left[\frac{(\sigma + p)^2 I_{rz}}{I_y} \right]$	$-1 \left[\frac{(p + \lambda_y) I_{rz}}{I_x} \right]$
Oscillation parallel to X axis in XZ plane	$x = r_0 \sin pt$ $y = 0$ $z = z_0 u(t)$	$1 \left\{ \frac{[(\sigma^2 + p^2)p + (2\sigma p)\lambda_x] I_{rz}}{I_y} \right\}$	$-1 \left\{ \frac{[(\sigma^2 + p^2)\lambda_y + (2\sigma p)p] I_{rz}}{I_x} \right\}$	$1 \left[\frac{(2\sigma p) I_{rz}}{I_x} \right]$	$1 \left[\frac{p I_{rz}}{I_y} \right]$
Oscillation parallel to Z axis in XZ plane	$x = r_0$ $y = 0$ $z = z_0 \sin pt$	$1 \left[\frac{(\sigma^2 - p^2) p I_{rz}}{I_y} \right]$	$-1 \left[\frac{(\sigma^2 - p^2) \lambda_y I_{rz}}{I_x} \right]$	0	0
Oscillation parallel to Y axis in YZ plane	$x = 0$ $y = r_0 \sin pt$ $z = z_0 u(t)$	$-1 \left\{ \frac{[(\sigma^2 + p^2)p + (2\sigma p)\lambda_y] I_{rz}}{I_x} \right\}$	$-1 \left\{ \frac{[(\sigma^2 + p^2)\lambda_x + (2\sigma p)p] I_{rz}}{I_y} \right\}$	$1 \left[\frac{(2\sigma p) I_{rz}}{I_y} \right]$	$-1 \left[\frac{p I_{rz}}{I_x} \right]$
Oscillation parallel to Z axis in YZ plane	$x = 0$ $y = r_0$ $z = z_0 \sin pt$	$-1 \left[\frac{(\sigma^2 - p^2) p I_{rz}}{I_x} \right]$	$-1 \left[\frac{(\sigma^2 - p^2) \lambda_x I_{rz}}{I_y} \right]$	0	0
The term I_{rz} denotes the constant inertia product $Q_{r_0 z_0}$.					

TABLE 2. - SOLUTION FUNCTION COEFFICIENTS FOR CHARACTERISTIC PERIODIC MOTIONS

Type of motion	Solution function coefficients			
	E_1	E_2	E_3	E_4
Circumferential motion in plane perpendicular to Z axis	$\left[\frac{I_{xz}}{2\lambda I_x I_y} \left\{ \frac{[(\sigma + p)^2 - (\lambda^2 - p^2)](p + \lambda_y)(\lambda_x I_y + \lambda_y I_x)}{\lambda^2 - p^2} + p \lambda_x I_x \right\} - p \lambda_y I_y \right]$	$\left[\frac{I_{xz}}{2\lambda I_x I_y} \left\{ \frac{[(\sigma + p)^2 - (\lambda^2 - p^2)](p + \lambda_y)(\lambda_x I_y + \lambda_y I_x)}{\lambda^2 - p^2} - p \lambda_x I_x \right\} + p \lambda_y I_y \right]$	$\left[\frac{I_{xz}(\sigma + p)^2}{2(\lambda^2 - p^2)I_x I_y} \right] \left[(p + \lambda_y)I_x + (p + \lambda_x)I_y \right]$	$\left[\frac{I_{xz}(\sigma + p)^2}{2(\lambda^2 - p^2)I_x I_y} \right] \left[(p + \lambda_x)I_x - (p + \lambda_y)I_y \right]$
Oscillation parallel to X axis in XZ plane	$-1 \left\{ \left[(\sigma^2 + p^2)p + (2\sigma p)\lambda_y \right] (\lambda_x I_x + \lambda_y I_y) - (\lambda^2 - p^2)p \lambda_x \right\} \left[\frac{I_{xz}}{2\lambda(\lambda^2 - p^2)I_x I_y} \right]$	$-1 \left\{ \left[(\sigma^2 + p^2)p + (2\sigma p)\lambda_y \right] (\lambda_x I_x - \lambda_y I_y) - (\lambda^2 - p^2)p \lambda_x \right\} \left[\frac{I_{xz}}{2\lambda(\lambda^2 - p^2)I_x I_y} \right]$	$1 \left[\frac{I_{xz}}{2(\lambda^2 - p^2)I_x I_y} \right] \left[(\sigma^2 + p^2)(p I_x + \lambda_y I_y) + (2\sigma p)(p I_y + \lambda_x I_x) \right]$	$1 \left[\frac{I_{xz}}{2(\lambda^2 - p^2)I_x I_y} \right] \left[(\sigma^2 + p^2)(p I_x - \lambda_y I_y) - (2\sigma p)(p I_y - \lambda_x I_x) \right]$
Oscillation parallel to Z axis in XZ plane	$-1 \left[\frac{I_{xz}p(\sigma^2 - p^2)(\lambda_x I_x + \lambda_y I_y)}{2\lambda(\lambda^2 - p^2)I_x I_y} \right]$	$-1 \left[\frac{I_{xz}p(\sigma^2 - p^2)(\lambda_x I_x - \lambda_y I_y)}{2\lambda(\lambda^2 - p^2)I_x I_y} \right]$	$1 \left[\frac{I_{xz}(\sigma^2 - p^2)(p I_x + \lambda_y I_y)}{2(\lambda^2 - p^2)I_x I_y} \right]$	$1 \left[\frac{I_{xz}(\sigma^2 - p^2)(p I_x - \lambda_y I_y)}{2(\lambda^2 - p^2)I_x I_y} \right]$
Oscillation parallel to Y axis in YZ plane	$\left\{ \left[(\sigma^2 + p^2)p + (2\sigma p)\lambda_y \right] (\lambda_x I_y + \lambda_y I_x) - (\lambda^2 - p^2)p \lambda_y \right\} \left[\frac{I_{xz}}{2\lambda(\lambda^2 - p^2)I_x I_y} \right]$	$\left\{ \left[(\sigma^2 + p^2)p + (2\sigma p)\lambda_y \right] (\lambda_x I_y - \lambda_y I_x) - (\lambda^2 - p^2)p \lambda_y \right\} \left[\frac{I_{xz}}{2\lambda(\lambda^2 - p^2)I_x I_y} \right]$	$-1 \left[\frac{I_{xz}}{2(\lambda^2 - p^2)I_x I_y} \right] \left[(\sigma^2 + p^2)(p I_y + \lambda_x I_x) + (2\sigma p)(p I_x + \lambda_y I_y) \right]$	$-1 \left[\frac{I_{xz}}{2(\lambda^2 - p^2)I_x I_y} \right] \left[(\sigma^2 + p^2)(p I_y - \lambda_x I_x) - (2\sigma p)(p I_x - \lambda_y I_y) \right]$
Oscillation parallel to Z axis in YZ plane	$\left[\frac{I_{xz}p(\sigma^2 - \lambda^2)(\lambda_x I_y + \lambda_y I_x)}{2\lambda(\lambda^2 - p^2)I_x I_y} \right]$	$\left[\frac{I_{xz}p(\sigma^2 - \lambda^2)(\lambda_x I_y - \lambda_y I_x)}{2\lambda(\lambda^2 - p^2)I_x I_y} \right]$	$-1 \left[\frac{I_{xz}(\sigma^2 - p^2)(p I_y + \lambda_x I_x)}{2(\lambda^2 - p^2)I_x I_y} \right]$	$-1 \left[\frac{I_{xz}(\sigma^2 - p^2)(p I_y - \lambda_x I_x)}{2(\lambda^2 - p^2)I_x I_y} \right]$
The term I_{xz} denotes the constant inertia product $\sum x_i y_i$.				

TABLE 6.- ASSUMED CHARACTERISTICS FOR MANNED ORBITAL
RESEARCH LABORATORY

Parameter	Module values		Total values
	Manned	Counterweight	
I_{x0} , slug-ft ²	103,000	30,000	133,000
I_{y0} , slug-ft ²	90,500	73,000	7,393,412
I_{z0} , slug-ft ²	173,000	73,000	7,475,912
m_s , slugs	1,220	557	1,777
Q , slugs	36	---	36
σ , rad/sec			0.4

TABLE 7.- DISTURBANCE EFFECTS ON MANNED ORBITAL RESEARCH LABORATORY

Type of disturbance	Disturbance characteristics	Error limits			
		Rate, rad/sec		Attitude, rad	
		Exact	Approximate	Exact	Approximate
Residual errors	$\phi_0 = \theta_0 = 0.1 \text{ rad}$ $\Omega_{x0} = \Omega_{y0} = 0.01 \text{ rad/sec}$	0.0161	0.0161	0.181	0.182
Step torques	$T_x = 384 \text{ ft-lb}$ $T_y = 3,300 \text{ ft-lb}$	0.0234	0.0234	0.0608	0.0609
Step inertia products	$x_0 = 50 \text{ ft}$ $y_0 = 4 \text{ ft}$ $z_0 = 4 \text{ ft}$	0.00387	0.00485	0.0963	0.0121
X axis radial mass oscillation	$x = 45 + 5 \sin \frac{2\pi t}{5} \text{ ft}$ $y_0 = 0$ $z_0 = 4 \text{ ft}$	0.00591	0.00686	0.0102	0.0107
Y axis transverse mass oscillation	$x_0 = 50 \text{ ft}$ $y = 4 \sin \frac{\pi t}{2} \text{ ft}$ $z_0 = 4$	0.0196	0.0224	0.0720	0.0857
Vertical mass oscillation	$x_0 = 50$ $y_0 = 4$ $z = 4 \sin \frac{\pi t}{2} \text{ ft}$	0.0134	0.0154	0.0291	0.0329

TABLE 8.- ASSUMED CHARACTERISTICS FOR 150-FOOT SPACE STATION

Parameter	Total value
I_{x0} , slug-ft ²	10,500,000
I_{y0} , slug-ft ²	10,500,000
I_{z0} , slug-ft ²	15,000,000
m_s , slugs	2,270
Q , slugs	36
σ , rad/sec	0.314

TABLE 9.-- DISTURBANCE EFFECTS ON 150-FOOT SPACE STATION

Type of disturbance	Disturbance characteristics	Error limits			
		Rate, rad/sec		Attitude, rad	
		Exact	Approximate	Exact	Approximate
Residual errors	$\varphi_0 = \theta_0 = 0.1 \text{ rad}$ $\Omega_{x_0} = \Omega_{y_0} = 0.01 \text{ rad/sec}$	0.0141	0.0141	0.176	0.176
Step torques	$T_x = T_y = 7500 \text{ ft-lb}$	0.0150	0.0150	0.0477	0.0478
Step inertia products	$x_0 = 49.5 \text{ ft}$ $y_0 = 49.5 \text{ ft}$ $z_0 = -20 \text{ ft}$	0.00616	0.00628	0.0169	0.0173
Circumferential mass motion	$x = 70 \cos \frac{4t}{70} \text{ ft}$ $y = 70 \sin \frac{4t}{70} \text{ ft}$ $z_0 = -20 \text{ ft}$	0.0153	0.0162	0.0380	0.0518
Radial mass oscillation	$x = 46 + 3.5 \sin \frac{7\pi t}{16} \text{ ft}$ $y = 46 + 3.5 \sin \frac{7\pi t}{16} \text{ ft}$ $z_0 = -20 \text{ ft}$	0.00650	0.00734	0.0196	0.0222
Vertical mass oscillation	$x_0 = 49.5 \text{ ft}$ $y_0 = 49.5 \text{ ft}$ $z = -15 - 5 \sin \frac{2\pi t}{5} \text{ ft}$	0.00590	0.00724	0.0175	0.0199